

INFORMATION TO USERS

This manuscript has been reproduced from the microfilm master. UMI films the text directly from the original or copy submitted. Thus, some thesis and dissertation copies are in typewriter face, while others may be from any type of computer printer.

The quality of this reproduction is dependent upon the quality of the copy submitted. Broken or indistinct print, colored or poor quality illustrations and photographs, print bleedthrough, substandard margins, and improper alignment can adversely affect reproduction.

In the unlikely event that the author did not send UMI a complete manuscript and there are missing pages, these will be noted. Also, if unauthorized copyright material had to be removed, a note will indicate the deletion.

Oversize materials (e.g., maps, drawings, charts) are reproduced by sectioning the original, beginning at the upper left-hand corner and continuing from left to right in equal sections with small overlaps.

ProQuest Information and Learning
300 North Zeeb Road, Ann Arbor, MI 48106-1346 USA
800-521-0600

UMI[®]

NOTE TO USERS

This reproduction is the best copy available.

UMI

Extravascular Density Imaging for Regional Partial Volume Correction of ^{18}F FDG Cardiac PET Images

by

Richard Wassenaar, B.Sc.

A thesis submitted to
the Faculty of Graduate Studies and Research
in partial fulfillment of
the requirements for the degree of
Doctor of Philosophy

Ottawa-Carleton Institute for Physics
Department of Physics, Carleton University
Ottawa, Ontario, Canada
Submitted June 2005

©copyright
2005, Richard Wassenaar



Library and
Archives Canada

Bibliothèque et
Archives Canada

0-494-08353-0

Published Heritage
Branch

Direction du
Patrimoine de l'édition

395 Wellington Street
Ottawa ON K1A 0N4
Canada

395, rue Wellington
Ottawa ON K1A 0N4
Canada

Your file *Votre référence*

ISBN:

Our file *Notre référence*

ISBN:

NOTICE:

The author has granted a non-exclusive license allowing Library and Archives Canada to reproduce, publish, archive, preserve, conserve, communicate to the public by telecommunication or on the Internet, loan, distribute and sell theses worldwide, for commercial or non-commercial purposes, in microform, paper, electronic and/or any other formats.

The author retains copyright ownership and moral rights in this thesis. Neither the thesis nor substantial extracts from it may be printed or otherwise reproduced without the author's permission.

AVIS:

L'auteur a accordé une licence non exclusive permettant à la Bibliothèque et Archives Canada de reproduire, publier, archiver, sauvegarder, conserver, transmettre au public par télécommunication ou par l'Internet, prêter, distribuer et vendre des thèses partout dans le monde, à des fins commerciales ou autres, sur support microforme, papier, électronique et/ou autres formats.

L'auteur conserve la propriété du droit d'auteur et des droits moraux qui protègent cette thèse. Ni la thèse ni des extraits substantiels de celle-ci ne doivent être imprimés ou autrement reproduits sans son autorisation.

In compliance with the Canadian Privacy Act some supporting forms may have been removed from this thesis.

Conformément à la loi canadienne sur la protection de la vie privée, quelques formulaires secondaires ont été enlevés de cette thèse.

While these forms may be included in the document page count, their removal does not represent any loss of content from the thesis.

Bien que ces formulaires aient inclus dans la pagination, il n'y aura aucun contenu manquant.


Canada

Abstract

Positron emission tomography (PET) is a modality capable of assessing heart muscle (myocardial) viability using the glucose analog, ^{18}F -fluorodeoxyglucose (FDG). Areas of reduced activity (reduced FDG uptake) may indicate regions of disease. However, image blurring can also result in apparent activity reductions, referred to as partial volume (PV) losses. This may complicate accurate interpretation of PET images.

An extravascular (EV) density image may be used to estimate the PV losses within the myocardium. The EV image is created by subtracting a blood pool (BP) image (acquired using ^{11}C -carbon monoxide) from a transmission (TX) image (total tissue density). The EV density image represents the amount of myocardial tissue present for tracer uptake. In this work, EV density imaging was investigated as a means of regional PV correction for PET viability imaging. As well, a novel method of BP imaging, using the early frames of the FDG data, was investigated.

Simulations showed that EV density imaging could correct for both motion- and resolution-based PV losses, but that increased activity and TX values in the organs adjacent to the heart lead to biased EV values. These results were confirmed in in-vitro experiments using two different phantoms. The EV image was able to correct for PV losses to within 5% for various myocardial wall thicknesses.

In-vivo dog model studies revealed that the EV image provided more accurate estimates of the myocardial activity, but with an increase in noise. TX spillover in the EV images resulted in an underestimation of the true activity, as predicted by the simulations. Use of an FDG-BP image was found to provide decreased EV density values, as compared with CO-BP imaging, resulting in an overestimation of the true activity. Similar results were obtained with studies involving normal subjects.

The EV density image was able to provide more accurate estimates of myocardial activity, but with increased image noise. As such, the method may have limitations as a pixel-by-pixel correction, but could be used with larger regions of interest.

Acknowledgments

I would like to thank my supervisor, Dr. Rob deKemp, for all of his support and guidance. He has taught me a lot during my tenure here, and it has been a wonderful experience working under his direction.

I would also like to thank my wife, Kerry, for her patience and support, particularly in regards to my long days of writing.

Lastly, I am indebted to all the staff at the Ottawa Heart Institute Cardiac PET Centre, who have helped me in this research and have made my time here an enjoyable one.

Contents

List of Tables	viii
List of Figures	ix
Glossary of Acronyms	xi
Overview	1
1 Introduction	4
1.1 Positron Emission Tomography	4
1.2 The Physics of PET	6
1.3 2D/3D PET	10
1.4 Detector Efficiency Correction	13
1.5 Randoms Correction	13
1.6 Scatter Correction	14
1.7 Attenuation Correction	15
1.8 Image Reconstruction	20
1.9 ECAT ART Scanner	21
2 Partial Volume Averaging	23
2.1 Extravascular Density Imaging	26
2.2 Literature Review	30
2.3 Alternative Methods of PV Correction	32
2.3.1 Constant Factors	32
2.3.2 Anatomical Information	32
2.3.3 Modeling	33
2.3.4 Tracer Kinetic Modeling	33
2.3.5 Geometrical Modeling	35

3	Simulations	36
3.1	Methods	37
3.1.1	PSF Measurements	37
3.1.2	Left Ventricular Model	37
3.1.3	LV Motion Model	39
3.1.4	Anatomical Heart Model	39
3.2	Results	40
3.2.1	PSF	40
3.2.2	LV Model	43
3.2.3	LV Motion Model	46
3.2.4	Anatomical Heart Model	47
3.3	Discussion	50
3.3.1	PSF	50
3.3.2	LV Model	51
3.3.3	LV Motion Model	52
3.3.4	Anatomical Heart Model	53
4	Left Ventricular Cardiac Phantom	55
4.1	Methodology	55
4.2	Results	58
4.3	Discussion	60
5	Variable Wall Cardiac Phantom	63
5.1	Methodology	63
5.2	Results	66
5.3	Discussion	68
6	Dog Model	72
6.1	Methodology	72
6.1.1	Echo	72
6.1.2	PET Imaging	73
6.2	Results	77
6.2.1	Echo	77
6.2.2	EV Correction	78
6.2.3	FDG-BP	84
6.3	Discussion	89
6.3.1	EV Correction	89
6.3.2	FDG-BP	92

<i>CONTENTS</i>	vii
7 Human Studies	95
7.1 Methods	95
7.2 Results	97
7.3 Discussion	103
8 Discussion	107
9 Future Directions	110
Conclusion	112
A Polar Maps	114
B EV Density Values and RC	118
B.1 MYO Model	118
B.2 EV Density Values	119
B.3 Hutchins Model	121
B.4 Modified EV Values	122
C Variable FDG Uptake and EV Density	124
D ¹¹C-Carbon Monoxide Production	127
References	131

List of Tables

1.1	PET isotopes	5
1.2	Scintillators	10
2.1	Published EV values	31
6.1	Pericardial FDG uptake	78
6.2	Pericardial CO uptake	79
8.1	Published EV values and present research	109
D.1	CO production	130

List of Figures

1.1	PET Images	5
1.2	Detection of Decay Process	8
1.3	Coincidence Types	9
1.4	2D/3D PET	11
1.5	Variable Axial Rebinning	12
1.6	Scatter Correction	15
1.7	Attenuation Correction	16
2.1	PV Effects	24
2.2	Uniform PV Effects	25
2.3	PV and Clinical Imaging	25
2.4	EV Density Imaging	29
2.5	Kinetic Modeling Estimates of PV Losses	34
3.1	PSF fwhm Measurements	41
3.2	Gaussian Fit of the PSF	42
3.3	Simulated LV Profiles	44
3.4	Residual BP Activity Effects	44
3.5	Simulated Phantom Profiles	45
3.6	EM/TX Resolution Effects	45
3.7	Cardiac Motion Profiles	46
3.8	Cardiac Heart Model	48
3.9	Variable RV/LV Values	48
3.10	Lung Density Effects	49
3.11	Inferior/Anterior Wall Simulation	49
4.1	Transaxial Slices of the LV Phantom	56
4.2	BP Image Dilation	57
4.3	TX Images Erosion	57
4.4	ROI Effect on the EV Values	59
4.5	Emission Smoothing Effects on EV Values	60

5.1	Variable Wall Phantom Diagram	64
5.2	Variable Wall Results	66
5.3	TX Ring Artifacts	67
5.4	Variable Wall Results using the Chest Phantom	68
6.1	SA, VLA, and HLA Slices for Study 2	75
6.2	Echo, 4 chamber view	77
6.3	Echo, SA view	78
6.4	MYO, EV, and Corrected MYO Polar Maps	79
6.5	Segmental Polar Map Values	81
6.6	Average Polar Maps	82
6.7	Segmental Values, 5 mm endocardial ROI shift	83
6.8	Intra-segment Variance	84
6.9	Average Polar Maps, FDG-based	85
6.10	Segmental Values, FDG-BP	86
6.11	CO-BP vs FDG-BP Scatter Plot	87
6.12	CO-EV vs FDG-EV Scatter Plot	88
6.13	Intra-segment Variance	88
6.14	FDG-EV Polar Map, study 5	89
7.1	SA, VLA, and HLA Slices for Study 1	96
7.2	MYO, EV, and Corrected MYO Polar Maps	97
7.3	Average Polar Maps	98
7.4	Segmental Polar Map Values	100
7.5	Intra-segment Variance	101
7.6	Subject Motion	102
7.7	MYO, EV, and Corrected MYO Polar Maps, 5 mm endocardial shift	103
A.1	PET Image Slices	115
A.2	Image Reslicing	116
A.3	SA, HLA, and VLA Slices	116
A.4	Polar Map Sampling and Segmentation	117
D.1	CO Standards Plot	130

Glossary of Acronyms

AF	attenuation factor
ASNC	American Society of Nuclear Medicine
BP	blood pool
CT	computerized tomography
EM	emission
EV	extravascular density
FBV	fractional blood volume
FDG	¹⁸ F-fluorodeoxyglucose
FORE	fourier rebinning
FOV	field of view
fwhm	full width at half max
fwtm	full width at tenth max
GC	gas chromatograph
HLA	horizontal long axis
IEEE	Institute of Electrical and Electronics Engineers
IV	intravenous
LA	left atrium
LOR	line of response
LV	left ventricle
MR	magnetic resonance
MSRB	multi-slice rebinning
MYO	myocardium

OSEM	ordered subset expectation maximization
PET	positron emission tomography
PSF	point spread function
PTF	perfusable tissue fraction
PTI	perfusable tissue index
PV	partial volume
RA	right atrium
RC	recovery coefficient
RC_H	recovery coefficient from Hutchins' model
RC_{EV}	recovery coefficient based on EV model
ROI	region of interest
RV	right ventricle
SA	short axis
SNR	signal to noise ratio
SSRB	single slice rebinning
TX	transmission
VARB	variable axial rebinning
VLA	vertical long axis

Overview

Positron emission tomography (PET) is a modality capable of non-invasively imaging biological function with the use of radioactively labelled pharmaceuticals (tracers). Areas of reduced tracer uptake appear as areas of reduced activity in the PET images, which may indicate disease. However, image blurring due to motion and limited spatial resolution can also result in a systematic over- or underestimation of tracer activity, referred to as partial volume (PV) averaging. In cardiac PET imaging, PV averaging can complicate diagnosis of cardiovascular disease.

Initially developed for the assessment of lung disease [1], the use of an extravascular (EV) density image has been proposed as a means of correcting for PV artifacts in the heart muscle (myocardium). The EV (or non-blood) image is obtained through the subtraction of a blood pool image (related to blood density) from a transmission image (total tissue density). ^{11}C -carbon monoxide is used as the gold standard for blood pool imaging, while transmission imaging is acquired in PET for attenuation correction of the PET data. Within the myocardium, the resulting EV density values represent the amount of tissue in a voxel that is capable of tracer uptake.

Previous studies have investigated EV density imaging in-vivo using ^{15}O -water and 2D PET. The EV density image was used to obtain a PV-free parameter referred to as the perfusable tissue index (PTI) [2, 3, 4, 5, 6, 7, 8], which was related to the amount of tissue capable of exchanging water.

One in-vitro study, also using 2D PET, has investigated EV density imaging for PV correction of FDG images [9]. A full in-vivo characterization of EV density imaging for regional PV correction of cardiac PET imaging has not been published.

In this research work, EV density imaging is characterized for use as a direct and regional PV correction of ^{18}F -fluorodeoxyglucose (FDG) cardiac 3D PET images. In particular, the effect of 3D PET, where resolution differences between the blood pool and transmission images may bias the EV density values, is investigated. This is important since many modern PET scanners currently operating are 3D-only. As well, the method is adapted for use with an algorithm that automates sampling of the activity of the entire myocardial wall (polar maps). This is in contrast to the previous studies which used 3 or 4 large, manually drawn regions of interest (ROI). The use of large regions may mask areas of disease. Lastly, the effects of regional anatomical structures (i.e. chest wall, liver, lungs, etc) on the EV image are investigated. These effects have been eluded to in previous papers, but never fully characterized.

A review of PET is presented in Chapter 1, followed by an overview of EV density imaging in Chapter 2. A synopsis of the current literature related to EV imaging is also given in Chapter 2. In Chapter 3, computer simulations of PET images provides proof of concept for EV density imaging. The method is then characterized using a phantom with a constant myocardial thickness and a phantom with a variable wall thickness in Chapters 4 and 5 respectively. Initial simulation and phantom work was presented at the 2001 Canadian Cardiology Society Annual Meeting [10], and at the 2002 SPIE Regional Meeting [11]. The results from Chapter 4 were presented at the 2002 IEEE Medical Imaging Conference [12] and later published in IEEE Transactions on Nuclear Science [13]. The results from Chapter 5 were presented at the 2004 IEEE Medical Imaging Conference [14], and were submitted for publication to IEEE Transactions on Nuclear Science in November 2004.

In-vivo results using a dog model are presented in Chapter 6, including a novel

method of obtaining the blood pool image. These results were presented as an abstract at the 2005 Society of Nuclear Medicine Annual Meeting [15]. In Chapter 7, the methodology is adapted to a set of normal human subjects. The main results of the thesis are then reviewed in Chapter 8, along with the implications for clinical cardiac PET imaging. This is followed by Chapter 9, in which future directions for this work are discussed. Finally, the main conclusions of this thesis research are summarized.

Chapter 1

Introduction

1.1 Positron Emission Tomography

Developed in the early 1970's [16], positron emission tomography (PET) has quickly become a major tool in the diagnosis and research of cardiovascular, neurological, and oncological disease. In contrast to computerized tomography (CT) and magnetic resonance (MR) anatomical images, PET non-invasively provides images of biological function through the introduction of a positron-emitting pharmaceutical (tracer) into the subject. Detection of the radiation produced during decay provides information used to determine tracer location.

Table 1.1 lists some commonly used isotopes in PET, as well as their positron energy and range in water [17]. PET tracers can be tailored for a variety of applications by chemically bonding these isotopes to an appropriate pharmaceutical. In Fig 1.1, three cardiac PET images acquired with three different tracers are presented. The first image measures blood flow to the heart muscle (myocardium) with ^{82}Rb , a potassium analog that is absorbed across intact cell membranes. In the second image, tissue viability is studied with ^{18}F -fluorodeoxyglucose (FDG), a glucose analog used as fuel by myocardial cells. Lastly, an image of the ventricles is obtained with the tracer ^{11}C -carbon monoxide, which has a high affinity for hemoglobin.

Table 1.1: Characteristics of several commonly used positron-emitting isotopes [17].

Isotope	Half Life (min)	Max Energy (MeV)	Mean Energy (MeV)	Max Range (mm)	Mean Range (mm)
^{18}F	109.8	0.64	0.25	2.3	0.35
^{11}C	20.4	0.96	0.39	4.1	0.56
^{15}O	2.07	1.72	0.74	8.1	1.1
^{13}N	9.96	1.19	0.49	5.2	0.72
^{82}Rb	1.3	3.35	1.52	16.7	2.4

Figure 1.1: Cardiac PET images of (A) blood perfusion to the heart using ^{82}Rb , a potassium analog, (B) tissue viability using the glucose tracer FDG, and (C) vascular image using ^{11}C -carbon monoxide.

One of the advantages of PET is that many of the elements listed in Table 1.1 are native to the body. This allows for the creation of tracers with well defined kinetics (uptake in organs, diffusion across membranes, cell metabolism, etc.) such as ^{15}O -water, ^{13}N -ammonia, and ^{11}C -acetate. In theory, any protein, sugar, or receptor ligand can be labelled with one of the isotopes listed in Table 1.1. This is in contrast to single-photon imaging (SPECT) which must make use of more exotic compounds labelled with ^{99m}Tc or ^{201}Tl .

Although the majority of clinical PET is performed for oncological studies (tumor characterization and location) with FDG, the focus of this thesis research is in the area of cardiac PET imaging, which has been previously reviewed by the author [18]. As

discussed above, PET provides a mean of assessing biological function using various tracers. Two of the most important cardiac applications are perfusion (measurement of blood flow to the heart muscle) and myocardial viability. Interpretation of these images by an expert provides a qualitative assessment of myocardial function [19], which is used to determine the best course of patient management (i.e. bypass surgery, drugs, etc.). Quantitative analysis of myocardial blood flow, metabolism, tissue viability, and neurohormonal receptor binding can also be performed by fitting of the kinetic PET data to a mathematical model of tracer uptake [20, 21].

In contrast, CT, MRI, and echocardiography (ultrasound) mainly provide images used to determine anatomical forms of cardiac disease. Echocardiography is primarily used to assess valvular abnormalities. It can also be used to assess wall thickening and motion abnormalities that can be indicative of infarcted (scar) tissue. Cardiac CT can be used to visualize calcification, aneurysms, regional hypertrophy and thrombus formation. MRI can also be used to assess similar anatomical pathologies as CT. As well, MRI has the potential to obtain contrast-free angiographic images, which are typically acquired using a contrast agent and planar x-ray angiography. Lastly, gadolinium-based agents can be administered for use in MRI to assess myocardial necrosis, in a manner complementary to FDG PET. A good review of cardiac imaging applications is given by Yachimske and Challender [22].

1.2 The Physics of PET

Most PET isotopes are produced by bombarding a suitable target nucleus with a beam of high energy (~ 10 MeV) protons. The resulting nuclear reaction transforms the initial target nucleus into a proton rich isotope. For example, ^{18}F is produced by the nuclear reaction between cyclotron accelerated protons and an enriched oxygen gas target, as given by Eq. 1.1. The ^{18}F atom may decay into a more stable form through either electron capture (3%) or positron emission (97%) processes. Isotopes may only decay via positron emission if the energy of the system is reduced by more than 1.022

MeV ($2m_0c^2$).



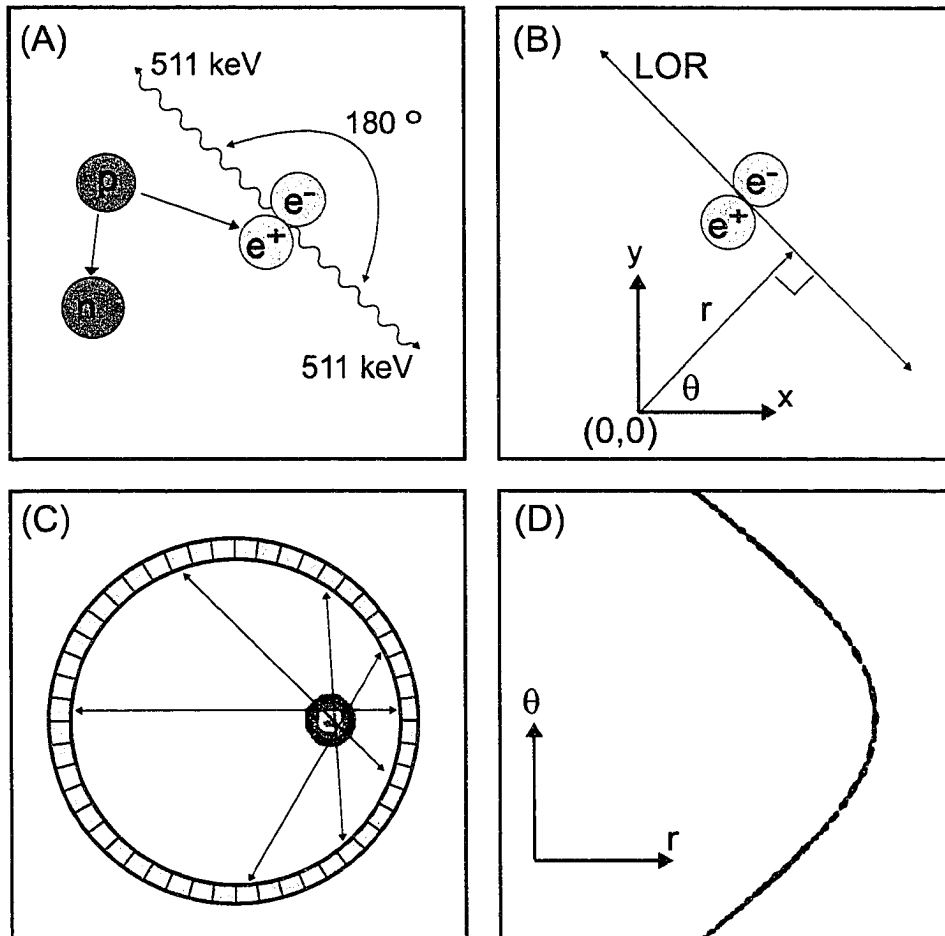
The process of decay via positron emission is given by Eq. 1.2. A nucleus proton decays into a neutron, ejecting a positron and an electron neutrino (Fig. 1.2). This decay results in a reduction of the total energy of the nucleus, which is carried away as kinetic energy by both the positron and neutrino. Mean and maximum positron energies are given in Table 1.1. The positron traverses the medium until its energy is reduced to thermal levels (~ 10 eV), at which point it annihilates with a nearby electron. Positron ranges in water are also tabulated in Table 1.1. The resulting annihilation event produces two gamma rays, each with an energy of 511 keV. If the initial momentum of both the positron and electron are zero, then, by conservation of momentum, the gamma rays are co-linear (180°). However, the positron typically has some finite momentum prior to annihilation which results in a deviation from co-linearity of approximately 0.5° [23].



Pairs of gamma rays are typically recorded by a ring of detectors surrounding the subject. Based on the crystal scintillation decay time and electronics timing, a coincidence window (on the order of 10 ns) is defined. Any two photons recorded by two separate detectors within this coincidence window are labelled as a coincidence event. This coincidence event is used to define a line of response (LOR) along which the decay occurred (Fig. 1.2).

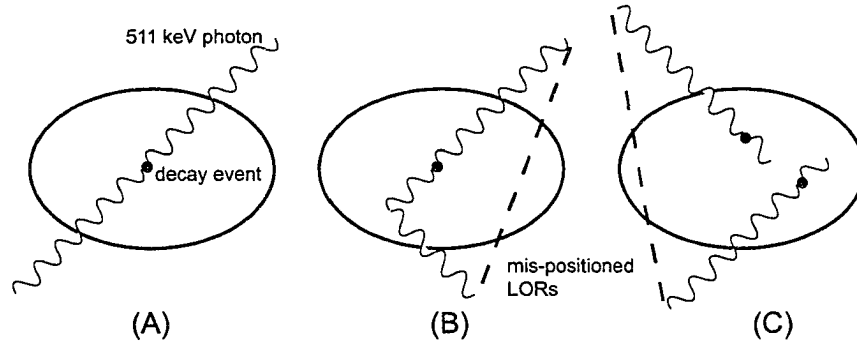
LORs are typically defined in polar coordinates and the events are stored as a histogram with each bin representing a unique (r, θ) coordinate. Such a histogram is referred to as a sinogram since a point source of activity will map out a half-sine wave.

Figure 1.2: (A) Positron decay of a nucleus proton results in the creation of a neutron and an ejected positron. The positron annihilates with a nearby electron, resulting in two co-linear 511 keV photons. (B) These photons describe a line of response (LOR), defined by (r, θ) , relative to the centre of the field of view (FOV). (C) A ring of detectors records the coincidence events, which are then stored in a sinogram. (D) Sinogram for a point source located off-centre in the FOV. Each bin in the sinogram corresponds to a unique (r, θ)



Events can also be stored in list-mode format. In list-mode, each LOR coordinate is stored as a separate line in a text file, along with other information, such as timing. From this file, a sinogram can be created post-acquisition. List-mode has the advantage

Figure 1.3: The three main types of coincidence events are: (A) trues, resulting from a single decay event, (B) scattered, where one or both of the photons have been scattered, and (C) randoms, where the coincidence event arises from two separate decay events.



of smaller files sizes for sparsely populated sinograms.

PET data is classified as either emission or transmission data. Emission data refers to the data collected when a tracer has been injected into the subject. This is the data that is reconstructed into the activity distribution image. With transmission data, an external activity source is used to acquire data in a manner similar to the x-ray tube on a CT scanner. The transmission data can be reconstructed into a map of the linear attenuation coefficients. The transmission file is used for emission data correction, as will be discussed shortly.

There are three main types of coincidence events, as illustrated in Fig. 1.3. Those originating from a single decay event, without scatter of either photon by the medium, are termed trues. However, if either photon is scattered by the medium, the coincidence event is mispositioned and a scattered event is recorded. A random event occurs when two photons originating from separate decay events are recorded as a coincidence event. Scatter and random events contribute to the background noise of the image and, as will be described later, must be corrected prior to image reconstruction.

Current PET detectors consist of a scintillating material coupled to a photo-

multiplier tube assembly. Table 1.2 lists some commonly used scintillators as well as their imaging properties [24]. Attributes of a good scintillator are: 1) high density for good photon absorption, 2) short decay time for increased photon counting rates, and 3) high light output to the PMT for improved energy resolution. The detectors are typically configured into a ring encompassing the subject. This ring defines a transaxial slice through the subject.

Table 1.2: Properties of several crystal scintillators used in PET.

Crystal	Density (g/cm ³)	Decay Time (ns)	Relative Light output*
NaI	3.67	250	1.00
BGO	7.13	300	0.15
LSO	7.40	40	0.75
GSO	6.71	65	0.35

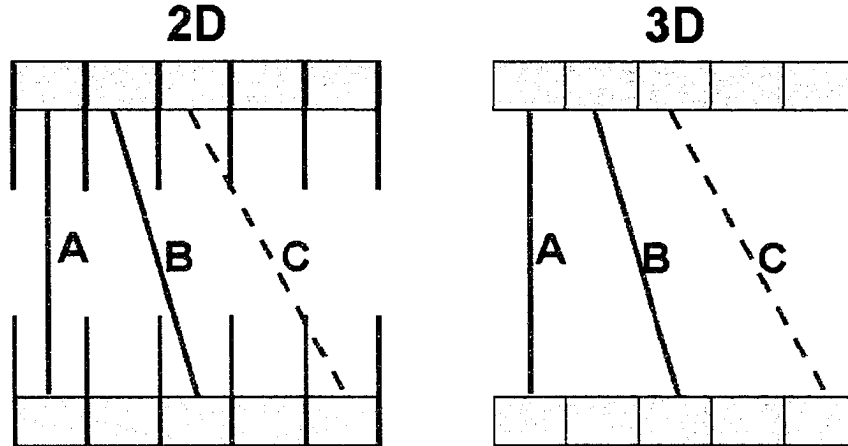
*relative to NaI

1.3 2D/3D PET

Traditional PET scanners were created by stacking a number of detector rings in the axial (z) direction. Each ring was separated by lead or tungsten septa extending into the field of view (FOV), as illustrated in Fig. 1.4. In traditional 2D scanners, detector rings with $\Delta r=0, 1$ were allowed to operate in coincidence, where Δr refers to the ring difference ($\Delta r = \text{ring1} - \text{ring2}$) between the coincidence photons. The $\Delta r=1$ LORs are assigned to a virtual plane defined between the two detector rings. LORs with $\Delta r > 1$ are attenuated by the septa.

The main advantage of this configuration was a reduction in the amount of scattered and random coincidences contributing to noise. However, the trade-off was a decrease in sensitivity (the number of counts recorded by the scanner for a given activity within the FOV) since many of the photons were absorbed by the septa.

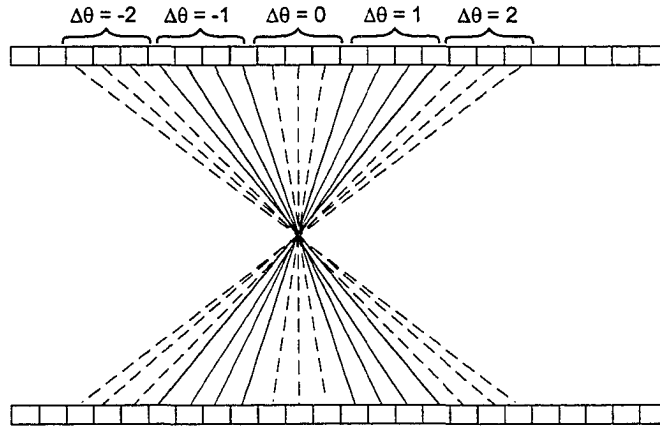
Figure 1.4: Septa between detector rings in a 2D system allow LORs such as A ($\Delta r=0$) and B ($\Delta r=1$), but attenuate more oblique LORs such as C ($\Delta r=2$). In 3D (no septa), coincidences between all detector rings are allowed.



In 3D acquisition, removal of the inter-plane septa allows for the acceptance of coincidences with $\Delta r > 1$ (Fig. 1.4). This results in an increase in scanner sensitivity by a factor of 4 to 7 [25, 26, 27] that can provide a statistical advantage in cardiac imaging [28, 29, 30]. However, noise in the form of scattered and randoms coincidence events is increased. As well, 3D acquisitions require up to N^2 sinograms to store the additional oblique LORs, where N is the number of detector rings. Along with memory management challenges, reconstructing the now correlated volume data is also more computationally intensive compared with reconstructing a set of independent 2D planes [31, 32, 33]. Rebinning of the 3D sinograms can be used to reduce the memory and reconstruction time requirements.

In 3D imaging, variable axial rebinning (VARB) is commonly used [34] during data acquisition. Two parameters, Δr and span, can be adjusted to restrict the number of oblique sinograms. The parameter, Δr , refers to the allowable ring difference. Span refers to the number of oblique sinograms that are averaged together. For example, a 3D scanner with 24 detector rings has $\Delta r_{max}=23$ and 576 possible sinograms. However with $\Delta r=17$ and span=7, 93% of the full 3D data is acquired with only 4 extra oblique

Figure 1.5: Example of variable axial rebinning (VARB) in a 24 ring system with $\Delta r=17$ and span of 7. Adjacent LORs in the θ direction are averaged to reduce the number of 3D sinograms. In this example, 4 oblique sinograms are present ($\Delta\theta=\pm 1,\pm 2$) with the 2D ($\theta=0$) sinogram



sinograms (175 sinograms in total), as illustrated in Fig. 1.5

Further rebinning of the 3D sinograms (which may have been previously rebinned using VARB) into independent 2D sinograms can offer a more substantial decrease in reconstruction time.

In single slice rebinning (SSRB) [35], the oblique LORs are assigned to the mid-plane, defined as $(r_1+r_2)/2$, where r is the ring number. However, off-axis activity is mispositioned, decreasing the axial resolution. This fast method offers accurate results when the activity is near the central axis of the scanner [36], as is the case in most cardiac studies. A variant of the SSRB algorithm is multi-slice rebinning (MSRB), which increments each transaxial plane traversed by the oblique LOR, thus reducing the axial blurring of off-axis activity. The accuracy of the MSRB algorithm is comparable to that of the dedicated 3D reconstruction algorithms, although the image signal to noise ratio (SNR) is generally lower [36]. The rebinning method most commonly employed today is Fourier rebinning (FORE) which assigns oblique LORs to a 2D transaxial sinogram based on an approximate frequency-distance relationship [37].

1.4 Detector Efficiency Correction

The process of correcting non-uniformities in detector pair efficiency is referred to as normalization. On traditional 2D scanners, blank scans were acquired using either rotating line sources [38] or plane sources [25]. The acquired data were then “inverted” to provide the normalization factors. However, these methods only measured the detector efficiencies in 2D mode and could not take into account geometric effects (i.e. varying ring difference) which are considerably different with 3D data [39].

Normalization of 3D data is performed using component based methods [39, 40, 41], which model the various effects that cause the non-uniformities. A 3D scan using rotating rods is performed to determine the geometrical effects. Individual detector efficiencies are estimated from a 3D scan of a uniform activity source such as a 20 cm diameter phantom. The individual terms are then combined mathematically to determine the overall efficiency for any particular 3D acquisition configuration [42].

1.5 Randoms Correction

A random coincidence is recorded when two gamma rays originating from separate decay events are detected within the coincidence timing window. The randoms rate is proportional to both the width of the coincidence window and the product of the singles rate of each detector, as given by:

$$R = \tau \cdot S_1 \cdot S_2 \tag{1.3}$$

where τ is the width of the coincidence window and S_1 and S_2 are the singles rates of

the two detectors.

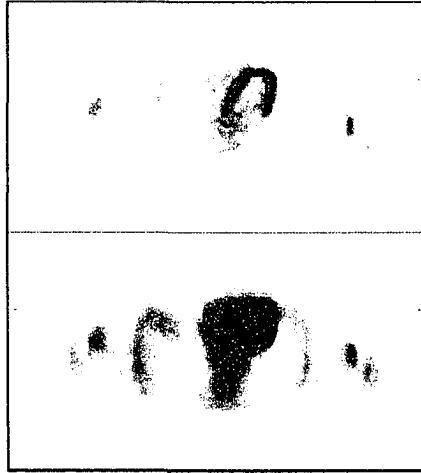
The number of random events can be estimated using a delayed window technique. A coincidence window offset in time from the initial window is created (e.g. 100 ns apart). Any coincidence event recorded by this second window must constitute a random coincidence event since the time delay precludes them from originating from the same decay. A random (or delayed) sinogram is acquired in this manner and subtracted directly from the raw sinogram. Alternately, the number of random events can also be estimated using Eq. 1.3, if the detector singles rates are known.

1.6 Scatter Correction

Scatter events are those which originate from a single decay, but where one or both of the photons has been scattered by the surrounding medium. Scatter events degrade image contrast and increase image noise by increasing the background counts. Fig 1.6 illustrates the effect of scattered photons on a FDG myocardial uptake image. In the uncorrected image, myocardial-to-background contrast is non-uniformly reduced due to the increased background noise from the inclusion of scattered events into the reconstruction algorithm.

Several methods have been proposed to remove the scatter coincidences. Multiple energy window methods estimate the scatter in the acquisition energy window from the data obtained at a higher energy, in which there should be no scattered events (i.e. $E > 511$ keV) [43, 44]. Such methods appear to work well for brain studies, but not when a non-uniform attenuating medium, such as the thorax, exists. Another method of scatter correction involves the acquisition of a short 2D scan along with the 3D data set. The 2D data sets can be assumed to contain almost no scatter, and thus comparison of the 2D data to the corresponding LORs in the 3D data can yield an estimate of the scatter component to be subtracted [45]. This method is not practical for 3D-only scanners.

Figure 1.6: FDG myocardial viability after (top) and before (bottom) model-based scatter correction. The estimated scatter fraction was approximately 54% and the increase in background noise due to the scattered events is clearly visible.

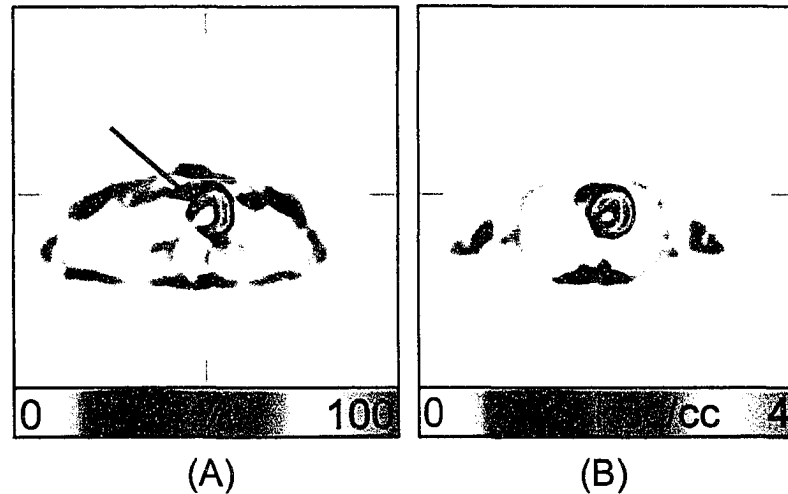


The most common method used in modern scanners is a direct calculation of the scattered distribution. This method is based on the fact that Compton scatter interactions are well modeled by the Klein-Nishina equation [46]. The shape of the single-scatter distribution can be estimated from the intensity of the emitted photons and knowledge of the attenuating medium. This information is contained in the emission and transmission images respectively. The scatter distribution should be calculated iteratively since the initial emission image still contains scatter [46, 47, 48]. This method has been shown to provide images as accurate as those obtained in 2D [46].

1.7 Attenuation Correction

Correction for the attenuation of the photons by the medium is required for accurate quantification of cardiac PET studies. As well, qualitative assessment of myocardial tracer uptake can also be biased due to non-uniform attenuation of the photons, which is a result of the variety of attenuating media present in the thorax (e.g. lung versus soft

Figure 1.7: (A) Cardiac image from a normal subject. No attenuation correction has been applied. This results in a perceived underestimation of the septal wall activity (arrow) relative to the opposing lateral wall. (B) Application of attenuation correction results in a more uniform activity distribution around the myocardial wall.



tissue). This attenuation of the photons can result in a non-uniform underestimation of myocardial activity, as shown in Fig. 1.7.

The probability of measuring a coincidence event is the product of the probabilities of detecting each photon, as given by Eq. 1.4, where the length of the medium is $x_2 - x_1$, μ is the linear attenuation coefficient, and X is the location of positron decay. This reduces to the equation for the attenuation of a single photon traversing the entire length of the medium. The attenuation of the coincidence events is independent of the depth at which the photons originated. This is in contrast to single-photon tomography in which the attenuation of the photons varies with the depth at which the photons originate.

$$\begin{aligned}
 P &= P_1 \cdot P_2 \\
 &= e^{-\int_{x_1}^X \mu(x) dx} \cdot e^{-\int_X^{x_2} \mu(x) dx} \\
 &= e^{-\int_{x_1}^{x_2} \mu(x) dx}
 \end{aligned} \tag{1.4}$$

Attenuation correction is achieved through transmission imaging, similar to CT imaging. Typically, external $^{68}\text{Ge}/^{68}\text{Ga}$ line sources are rotated around the FOV to acquire the transmission data. As well, a reference sinogram (or blank scan since no medium is present in the FOV) is acquired each morning. The patient transmission scan records the number of photons, N , while the reference scan records N_o . The values N and N_o are related by Eq. 1.5, where the integral is taken over the entire length transversed by the photons.

$$\frac{N}{N_o} = e^{-\int_{x_2}^{x_1} \mu(x) dx} \quad (1.5)$$

Division of the transmission data by the reference data yields a sinogram containing the probabilities of detecting a coincidence event along a given LOR (comparison of Eq. 1.4 with Eq. 1.5), also referred to as the attenuation factors. Correction for photon attenuation is obtained by dividing the raw image sinogram by the attenuation factor sinogram.

Singles Transmission Imaging

On 2D scanners, $^{68}\text{Ge}/^{68}\text{Ga}$ rod sources are used to acquire coincidence data for transmission imaging. With 3D scanners, the removal of the septa results in large deadtime losses in the detectors closest to the rod sources, unless the activity of the sources is lowered at the expense of image quality or scan time. As well, removal of the septa results in an increase in scatter to the transmission data.

On 3D scanners with retractable septa, a transmission image in 2D mode (with septa) can be acquired and forward-projected to obtain the 3D transmission data [49]. In newer 3D-only scanners which do not contain septa, transmission data can be acquired using singles transmission sources. Instead of a ^{68}Ge rotating line source, a translating and rotating point source of ^{137}Cs (a single 662 keV photon emitter) is used

[50, 51]. Since only the detectors opposite the source are counting in singles transmission imaging, deadtime losses are reduced. This allows for the use of higher activity sources (400-800 MBq) to improve transmission image quality or shorten scan times.

Attenuation factors measured with ^{137}Cs methods must be scaled to the equivalent 511 keV values [52] and the increased scatter must also be accounted for. With uncollimated sources, as in the ECAT EXACT3D (Siemens), ADAC CPET (Philips), and ALLEGRO (Philips) scanners, segmentation methods can be used to compensate for both energy scaling and scatter. The transmission image is segmented (i.e. air, soft tissue, and bone) and the peaks of the histogrammed values from these regions are then reassigned to the narrow-beam attenuation values at 511 keV [53]. A potential problem with segmentation is the effect of cardiac and respiratory motion which blurs together lung and soft tissue, making segmentation along the inferior-lateral wall of the left ventricular (LV) myocardium difficult. With collimated transmission sources as in the ECAT ART, the 2D ACFs can be calculated directly by dividing a reference (blank) scan by the transmission scan [54, 55]. However, these ACFs can still display a small bias related to patient size. Ideally, scatter should be rejected completely from the 3D transmission scan using point source coincidence measurements and dedicated fast transmission detectors near the sources [56]

CT Based Transmission Imaging

A rapidly emerging trend today is the use of combined PET/CT scanners. This modality is being driven by oncology studies where fusion of the PET and CT images provides advantages in interpretation and treatment planning [57, 58]. Cardiac PET/CT offers several potential advantages over conventional PET systems, such as respiratory- and ECG- gated attenuation correction and accurate measurement of myocardial wall-thickness. Myocardial wall-thickness information can potentially be used for partial volume correction or as prior anatomic information in image reconstruction.

In PET/CT systems, the high quality CT image can also be used to calculate the attenuation factors. The CT values obtained from the polyenergetic X-ray beam must be scaled to the appropriate 511 keV values [59, 60]. This is often performed by segmentation methods, similar to those used in singles transmission imaging. The segmented CT image is then forward projected to obtain the transmission data.

However, differences in respiratory and cardiac motion between the emission and transmission scans can introduce attenuation correction artifacts in cardiac imaging. A recent study in our lab showed that the FDG myocardial uptake values were underestimated by approximately 7% when a CT based attenuation correction was used [61]. Respiratory gating of the CT images may prove useful in removing this bias.

Post-Injection Imaging

Transmission data using coincidence or singles methods can be acquired in either a pre- or post- injection mode. A pre-injection transmission scan is acquired prior to injection of the PET isotope.

A post-injection transmission scan is acquired after injection of the PET isotope, where counts from the injected activity contaminate the transmission data. To compensate for this on the ECAT ART, the transmission sources are shielded for half of the scan duration. During this time, the injected activity is counted, and later subtracted from the data acquired with both the transmission source and injected activity.

A pre-injection acquisition provides a higher quality transmission image. However, the post-injection transmission data are typically acquired closer to the time of emission acquisition, reducing the effects of misalignment due to subject movement [62].

1.8 Image Reconstruction

Reconstruction of the PET sinograms can be performed using either filtered back-projection or iterative techniques. With 2D PET, each plane is reconstructed independently of the others. With 3D PET, the inclusion of the oblique sinograms requires 3D-specific reconstruction algorithms.

The analytic 3D reconstruction algorithm set forth by Colsher in 1980 is based on backprojection with a filter applied to the image in frequency space [63]. This algorithm has become the basis for most of the 3D backprojection algorithms currently in use. One requirement of the method is complete projections in all directions. However, due to the limited axial extent of the detectors, oblique sinograms are truncated. The 3D reprojection (3DRP) algorithm developed by Kinahan and Rogers [31] solved this limitation by first reconstructing an initial image from the non-truncated sinograms and then reprojecting through this initial image to estimate the missing data. The completed set of sinograms was then used for full 3D reconstruction. Due to the large number of sinograms in a full 3D dataset and the need to forward project the missing data with 3DRP, reconstruction times of several hours were common [31, 32, 33]. Other variations which did not require completion of the missing projections were also suggested to shorten reconstruction times, such as the fast volume reconstruction algorithm (FAVOR) [64].

Decreased 3D reconstruction times can be achieved through use of the standard 2D algorithms on rebinned (either FORE or SSRB) data. Initially, FORE was combined with 2D backprojection techniques to provide images comparable to those obtained with 3DRP, but in an order of magnitude less time [37, 65, 66]. More common now is the application of 2D iterative techniques, such as ordered subsets expectation maximization (OSEM) or row action maximum likelihood algorithm (RAMLA), to FORE data. Since FORE is fast, reconstruction time is similar to conventional 2D iterative methods, allowing this approach to be clinically practical [67, 68].

1.9 ECAT ART Scanner

One of the major contributors to the price of a PET scanner is the scintillator/PMT/electronics assembly. In an attempt to reduce the cost of PET scanners, several novel configurations comprised of rotating partial detector rings have been proposed [69, 70]. The scanner used for acquisition of all data for this thesis investigation, the ECAT ART (Siemens/CTI), is an example of such a system.

The ECAT ART is a partial ring PET scanner consisting of 2 banks of detectors covering 31% of a full ring. The banks are mounted on a gantry via slip rings and rotated at 30 rpm to acquire full-ring equivalent data.

The detectors are comprised of a $6 \times 6 \text{ cm}^2$ block of BGO coupled to 4 PMTs. The surface of the block is etched into 8×8 detector elements. The relative light output from the four PMTs is used in positioning the incident gamma ray. Each bank on the ECAT ART consists of 3 detector blocks in the axial direction and 11 detector blocks transaxially, for a total of 2112 detectors per bank.

The ECAT ART is a 3D-only scanner since it contains no interplane septa. Variable axial rebinning combined with Fourier rebinning is used to produce 2D sinograms from the 3D data. The resolution of the ECAT ART is approximately 6.4 mm in the center of the FOV. [69].

Transmission imaging is performed using 2 collimated ^{137}Cs sources and can be acquired in either post- or pre- injection mode. To reduce scatter bias in the transmission data, the reference (blank) scan is acquired with a large attenuating slab of plastic ($\mu = 0.096 \text{ cm}^{-1}$) in the FOV [55]. Scatter from the emission images is corrected using a direct calculation method scaled with a constant factor [71]. Normalization is per-

formed using a component based method [41]. Random events are subtracted using a delayed coincidence window technique.

Chapter 2

Partial Volume Averaging

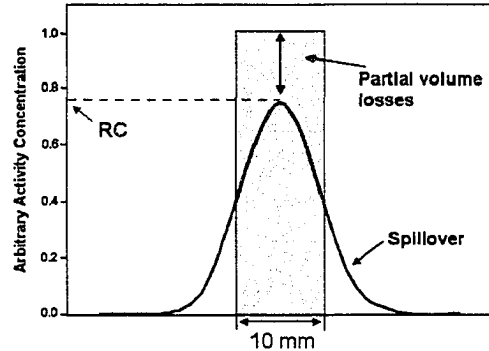
The limited spatial resolution of the scanner and organ motion (i.e. cardiac, respiratory, etc.) lead to a blurring of the PET images. This blurring results in a mixing of the activity signal from adjacent voxels, and is commonly referred to as partial volume (PV) averaging [72]. PV averaging can be further categorized into spillover and PV losses.

Spillover is defined as the blurring of activity from adjacent voxels into the target voxel. This leads to an overestimation of the true target activity. Blurring of activity from the target voxel into adjacent voxels is referred to as PV losses. PV losses result in an underestimation of the true activity. PV losses are quantified by the recovery coefficient (RC), which is defined as the ratio of the measured activity to the true activity.

Figure 2.1 illustrates the effect of PV averaging on a 10 mm thick region of activity, due to 10 mm scanner resolution. In this example, PV averaging results in a RC of 0.76, or a 24% underestimation of the activity. The RC approaches a value of 1.0 for regions greater than twice the full-width half-maximum (fwhm) of the scanner's resolution.

In myocardial images with uniform uptake, PV averaging can reduce the measured activity concentrations. Fig. 2.2 is an image of the left ventricular (LV) heart phan-

Figure 2.1: A 10 mm region of activity (normalized to 1.0) convolved with a 10 mm fwhm kernel leads to PV losses. The maximum measured activity (line) underestimates the true activity by $\sim 24\%$ (RC=0.76).



tom (Data Spectrum) filled with 59 kBq/cm^3 of activity. The myocardial wall of the phantom is a constant 10 mm thick, resulting in the uniform activity distribution seen. However, the measured PET signal from this image is 41.5 kBq/cm^3 . This corresponds to a RC of 0.70, or a 30% reduction in the measured activity.

In cardiac PET, PV losses are affected by myocardial wall thickness and cardiac motion, both of which may vary about the myocardium. This non-uniform PV averaging can complicate accurate diagnosis of cardiovascular disease, as illustrated in Fig 2.3. In this example, a vertical long axis (VLA) slice (see Appendix A) of a FDG uptake image from a normal volunteer is compared to an image from a patient with a mild defect. Uniform uptake is expected around the LV myocardial wall in the normal subject. However, the apex region is typically thinner and undergoes increased motion relative to the septal and lateral walls. As a result, PV losses are increased in this area leading to an underestimation of the activity. This apparent reduction in FDG may appear similar to the reduced FDG uptake resulting from the mild defect. Distinction between reduced FDG uptake resulting from disease and apparent reduction resulting from PV averaging can be difficult. As such, a means of removing PV losses is necessary for accurate diagnosis.

PV averaging can result in a localized apparent reduction in tracer uptake. This may lead to false positive tests or hide true areas of disease. Correction of PV averaging may improve the use of PET for more accurate diagnosis of cardiovascular disease.

Figure 2.2: (left) Uniform activity is seen in the LV heart phantom due to uniform PV averaging (the wall has a constant thickness of 10 mm). (right) However, a line profile through the cavity indicates that the absolute activity is underestimated by 30%, due to PV effects.

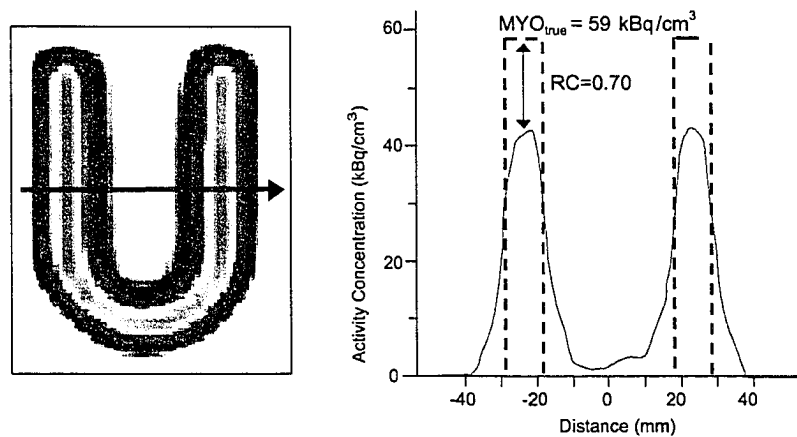
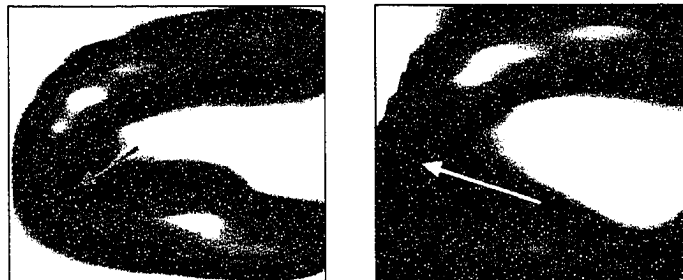


Figure 2.3: VLA FDG images of a normal heart (left) and from a patient heart with a defect (right). Uniform uptake should be seen around the entire LV myocardial wall in the normal heart. However, increased PV losses in the apex result in an apparent reduction (red arrow) of activity. This appears similar to the reduction in activity resulting from the defect (yellow arrow).



2.1 Extravascular Density Imaging

Initially developed for quantitative measurements of extravascular (EV) lung density [1], EV density imaging has been proposed as a means of correcting for PV losses in cardiac PET studies [2]. The EV density image depicts the non-vascular component of tissue within each voxel (units of g/cm^3). In the myocardial wall, *the EV density image represents the density of myocardial tissue capable of tracer uptake.*

The EV density image is derived from the subtraction of a blood pool (BP) image from a transmission (TX) image using Eq 2.1. The BP image represents the total vascular component within each voxel and is typically obtained using a tracer with a high affinity for red blood cells, such as ^{11}C -carbon monoxide. The 511 keV linear attenuation coefficients of the TX image are proportional to the total density of the material within the voxel. The TX and BP images are normalized to a region of pure blood, located in the LV cavity, prior to subtraction. The values are then scaled to the density of whole blood, $1.06 \text{ g}/\text{cm}^3$. The methodology is illustrated in Fig. 2.4.

$$EV = \left[\frac{TX}{TX_{LV}} - \frac{BP}{BP_{LV}} \right] * 1.06 \text{ g}/\text{cm}^3 \quad (2.1)$$

Eq. 2.1 contains four terms that have the following properties in a myocardial voxel.

- 1) For a given mass of tissue, TX/TX_{LV} represents the fractional volume of blood with the same mass as the tissue present in the voxel. In myocardial regions with no

PV losses, this term goes to 0.98 since:

$$\begin{aligned}
 \frac{TX}{TX_{lv}} &= \frac{\mu_{muscle}}{\mu_{blood}} \\
 &\approx \frac{\rho_{muscle}}{\rho_{blood}} \\
 &= \frac{1.04 \text{ g/cm}^3}{1.06 \text{ g/cm}^3} \\
 &= 0.98
 \end{aligned} \tag{2.2}$$

Eq. 2.2 assumes that the ratio of the linear attenuation coefficients is equal to the ratio of the densities. This is a valid assumption at 511 keV, since the mass attenuation coefficient is similar for most materials (e.g. lead versus air) due to the dominance of the Compton process [73]. In areas with PV losses, this volume is reduced ($TX < TX_{LV}$) due to PV losses across the epicardium (outer myocardial wall), and so this term contains PV information near the epicardium. It is assumed that only blood and myocardium contribute to the TX signal. In areas such as the anterior or inferior walls, chest wall or liver TX spillover may confound the signal, and the fractional volume may be overestimated. In the lateral wall, a more accurate estimate of the fractional volume may be obtained due to the lower value of lung density.

2) The second term, BP/BP_{LV} , represents the fractional volume of blood in the voxel. This includes both the fractional blood volume (FBV, i.e. blood vessel space; approximately 10% within the myocardial wall [2]) and spillover from the ventricular cavities into the myocardial (MYO) region. This term contains PV information near the endocardium (inner myocardial edge) and is often referred to as the total blood volume (TBV) in kinetic modeling [74].

3) The subtraction of the above two terms yields the fractional volume containing myocardium tissue.

4) The last term is used in scaling to true myocardial density values. Terms 1 and 2 are scaled by the value of whole blood (1.06 g/mL) since a region in the LV cavity

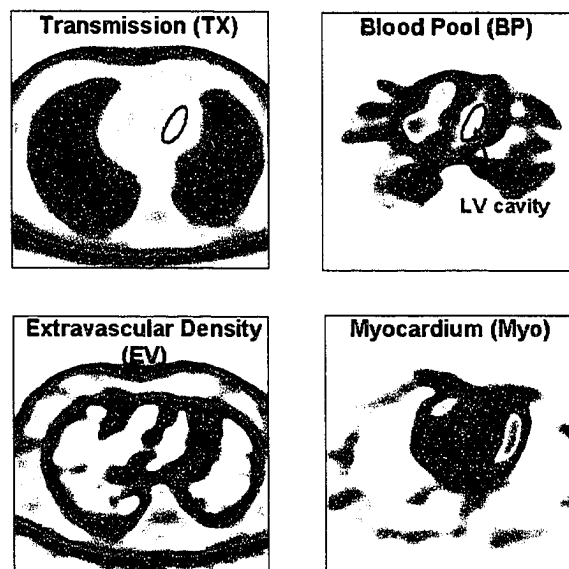
was used for normalization. Scaling by the density of whole blood accounts for the TX contrast difference between MYO and LV transmission values (Eq. 2.2).

Within the MYO region, the EV density values are reported to approximate the underestimation of activity resulting from PV losses. Dividing the measured myocardial activity (Bq/cm^3) by the corresponding EV density value (g/cm^3), as given in Eq. 2.3, should provide PV-free estimates of activity (Bq/g). The EV density correction assumes that PV averaging of the myocardial wall is identical to the TX spillover along the epicardium and the complement of the BP spillover along the endocardium.

Application of the EV density values to the measured myocardial activity (MYO) results in a units transformation (from Bq/cm^3 to Bq/g). Due to this units transformation, a normalized activity of $1.0 \text{ Bq}/\text{cm}^3$ is not expected. Rather, the true, normalized activity is $0.962 \text{ Bq}/\text{g}$. Appendix B reviews two cases to clarify the use of EV density imaging for PV correction, and also develops the relationship between EV and RC.

$$MYO_{true} = \frac{MYO_{measured}}{EV} \quad (2.3)$$

Figure 2.4: Subtraction of the BP (top right) image from the TX image (top left), after normalization of each to a region of pure blood (LV cavity), yields the EV image (bottom left). The measured myocardial image (MYO), obtained using FDG, is shown in the bottom right. Within the myocardial wall, the EV density values can be used to estimate the RC. The pattern between the EV and MYO should be similar in the absence of disease. In this example, the reduced septal activity in the MYO corresponds to reduced EV values in the same region, indicating this reduction is due to PV losses.



2.2 Literature Review

Iida et. al. [2] first introduced the concept of EV density imaging for ^{15}O -water studies. The EV density values were compared with the perfusable tissue fraction (PTF), a parameter obtained from kinetic modeling of the dynamic data. The PTF was defined as the fractional volume of the voxel which was freely diffusable to water. In the kinetic model, the PTF accounted for PV losses and was used as an estimate of the RC. The ratio of the PTF to EV was defined as the perfusable tissue index (PTI), or the amount of water perfusable tissue per gram of myocardium in the voxel. It was hypothesized that the ratio of PTF to EV should be unity for normal tissue and less than unity for diseased myocardium [8].

Subsequent papers further characterized the concept of EV density imaging for PTI measurement [3, 4, 5, 6, 7]. Each of these studies investigated the methodology on ^{15}O -water/ ^{15}O -carbon monoxide studies and, with the exception of [7], 2D PET. EV density values from the published papers are tabulated in Table 2.1. Knaapen et. al. [75] provides a good overview of the significant contributions of each of these papers.

Gerber et. al. [4] also compared CO blood pool (BP) imaging with FDG blood pool imaging. The first 45 s of a dynamic FDG study was summed to create the FDG-BP image. A comparison of EV values obtained using both the CO-BP and FDG-BP was made and no significant difference between the two was found.

In all of the PTI papers, the EV density image was used solely for the purposes of PTI measurement and not as a means of regional PV correction of the ^{15}O -water data. As well, relatively large regions, typical for ^{15}O -water studies, were used.

Spinks et. al. [9] have published an in-vitro characterization of EV density imaging for regional PV correction. A custom-built left ventricular cardiac phantom with a myocardial wall thickness varying between 3 mm and 27 mm was imaged using ^{18}F and

Table 2.1: Published EV density values (1σ) for normal myocardium

		LAT	ANT	SEP	INF
Human	Iida 1991	0.62 (0.05)	0.64 (0.04)	0.62 (0.05)	N/A
	Yamamoto 1992	0.66 (0.03)	0.68 (0.04)	0.63 (0.04)	0.67 (0.05)
	Gerber 1998	0.64 (0.02)	0.63 (0.02)	0.56 (0.02)	N/A
	Gerber* 1998	0.62 (0.02)	0.63 (0.02)	0.56 (0.02)	N/A
Dog	Iida 2000	0.48 (0.09)	0.48 (0.05)	0.42 (0.05)	N/A

* BP image created from the FDG dynamic data

2D PET. The EV density values were able to correct for PV averaging for thicknesses between 10 mm and 27 mm. However, below 10 mm, the corrected values were still underestimated. This underestimation was believed to result from biasing due to both the construction of the phantom and TX spillover from the lung.

Hutton et. al. [76] have published simulation results of the methodology adapted to SPECT imaging. In this paper, the effects of transmission and emission resolution differences were considered with respect to attenuation correction. However, the effect of resolution mismatch on the EV density values was not investigated. In 3D PET, it may be difficult to match transmission and emission resolutions. This resolution mismatch may be expected to bias EV density values.

Various aspects of EV density imaging have been investigated. However, to date there has not been a complete characterization of the methodology for regional PV correction of PET images. The effect of ROI size on accuracy and noise has not been investigated. As well, the possible bias due to resolution mismatch must be quantified if EV density imaging is to be used clinically with newer 3D-only scanners. The purpose of this research thesis was to fully characterize EV density imaging as a direct and regional (i.e. polar map basis) PV correction for FDG viability studies using au-

tomated ROI placement. This study included an investigation into the effects of ROI size, resolution mismatch, and contaminating signal from adjacent organs on the EV image.

2.3 Alternative Methods of PV Correction

2.3.1 Constant Factors

The simplest method of PV correction is to divide the measured MYO values by a constant RC [77]. This is useful in quantitative analysis where PV averaged data may bias the final results. The disadvantage of this type of correction is the assumption that PV losses are uniform about the myocardial wall. Application of a constant factor does not change the relative distribution of the tracer within the myocardium. This limits the clinical usefulness of the methodology, since it is the relative non-uniformity of tracer distribution that is typically used to assess cardiovascular disease from PET images.

2.3.2 Anatomical Information

A more recent method of PV correction involves the use of high-resolution anatomical images, typically obtained from either CT or MRI. From these high-resolution images, information regarding wall thickness is used to estimate PV losses. There are two approaches to this type of PV correction.

The first approach involves segmentation of the myocardium. This area is assigned unity activity and convolved with the point spread function (PSF) of the PET scanner to determine PV losses on a pixel-by-pixel basis. For example, the myocardial wall from a CT image is segmented with each pixel being set to 1.0 to represent the true activity distribution. All other pixels are set to 0.0. This segmented image is then convolved

with the PSF of the scanner. After convolution, each pixel within the myocardium corresponds to the RC for that pixel [78]. These values can then be applied on a regional basis, in a manner similar to EV density values, to correct for PV losses.

This approach has been investigated for neurological studies [79, 80, 81, 82]. However, there have been limited studies applying the method to cardiology [78].

In the second approach, CT or MRI data is used as a-priori knowledge in iterative reconstruction. The CT or MRI data is again segmented, but this time it is used to weight the PET data during image reconstruction. [83, 84, 85].

One of the disadvantages of these types of corrections is the need for an anatomical image and the subsequent registration of the PET and MR/CT images. Even on combined PET/CT systems, we have shown that respiratory motion differences between the CT and PET data may introduce artifacts [61]. For these reasons, this method of PV correction has seen limited development in cardiology.

2.3.3 Modeling

2.3.4 Tracer Kinetic Modeling

Kinetic modeling of the tracer distribution as a function of time can yield parameters related to biological function, such as blood flow. In creating the kinetic models, a parameter accounting for PV averaging can be introduced, as shown in Eq. 2.4 [74].

$$C_{pet}(t) = TBV \cdot C_a(t) + (1 - TBV) \cdot C_m(t) \quad (2.4)$$

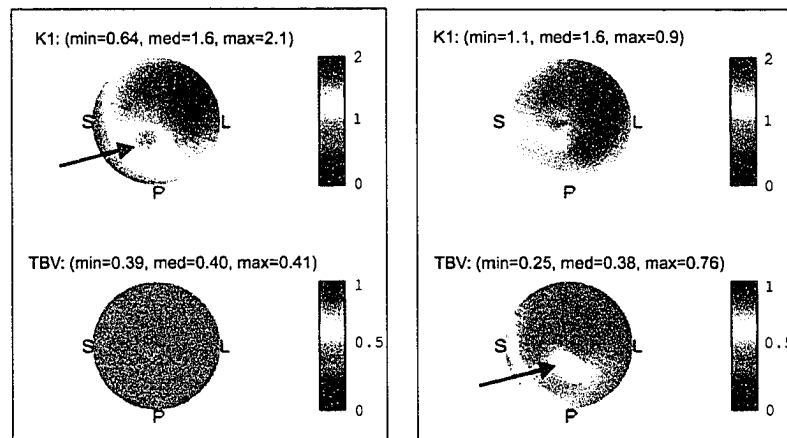
where

- $C_{pet}(t)$ is the measured MYO signal (Bq/cm³),
- $C_m(t)$ is the true myocardial PET signal

- $C_a(t)$ is the arterial blood signal, and
- TBV represents the fractional volume of the voxel occupied by the blood pool activity (0.0 to 1.0). This is comprised of both spillover from the ventricular cavity, and vascular space (i.e. blood vessels, capillaries, etc.) within the myocardial tissue.

In this model, $1-TBV$ is an estimate of the recovery coefficient, including vascular space (RC_H), as described in Appendix B. $C_m(t)$ is related to $C_a(t)$ by parameters of the kinetic model, such as blood flow and tracer uptake into the cell. These parameters, along with TBV, can be solved by fitting the model to the measured data. Fig. 2.5 illustrates the effects of setting TBV (and hence RC_H) to a constant in the model versus allowing TBV to vary. A disadvantage of this methodology is that the derived model parameter values can be correlated with the partial volume parameter [74, 86].

Figure 2.5: Kinetic modeling of blood flow (K1) for ^{82}Rb . The images on the left were obtained by setting RC_H to a constant value of 0.6 (TBV=1-RC=0.4). This reduced flow values in the inferior-apex wall (arrow). However, when RC_H was allowed to vary, (images on the right) increased TBV (reduced RC) values were seen in the same region, leading to more uniform flow and indicating that the initial flow estimates may have been biased due to PV loss from reduced wall thickness and increased motion.



2.3.5 Geometrical Modeling

In geometrical modeling, an estimate of the target size and the activity concentration is used along with the scanner's geometry and PSF to compute a set of sinograms [87, 88, 89]. These estimated sinograms are compared with the measured sinograms. Changes to the initial parameters (size, activity) are iteratively performed until the estimated and measured sinograms match. This method has been found to produce accurate results for simple spheres greater than 3.2 mm in diameter [87]. However, the method requires accurate modeling of the activity and scanner geometry, and has not been developed for the more complex geometry of cardiac imaging.

Chapter 3

Simulations

Computer simulations of the PET images were performed as an initial validation of EV density imaging for PV correction. The advantage of computer simulations was the ability to exactly define activity distributions of interest. This allowed for characterization of PV averaging and the EV correction under various clinically relevant conditions.

PET images can be simulated by approximating the scanner as a linear and shift invariant system. The PET image, $I(x,y,z)$, is the convolution of the true activity distribution, $A(x,y,z)$, with the point spread function, $PSF(x,y,z)$, of the scanner, as given by Eq. 3.1. The PSF is a measure of the amount of blurring introduced by the system and is defined as the response of the system to a delta function of unit area.

$$I(x,y,z) = A(x,y,z) \otimes PSF(x,y,z) \quad (3.1)$$

Several papers have derived analytical models describing the PSF function [87, 88]. However, the PSF can also be estimated using a point source of activity. Typically, a long thin needle of activity is used to approximate a point source in the transaxial plane, $PSF(x,y)$. With this 2D PSF, 2D images can be simulated for any arbitrary

activity distribution.

3.1 Methods

3.1.1 PSF Measurements

A stainless steel needle (inner and outer diameters of 1.3 mm and 1.8 mm respectively) filled with ^{18}F and placed axially in the FOV was used to emulate a point source in the transaxial plane. Data was acquired in 3D mode with a $\Delta r/\text{span}$ of 17/7, and 2x angular compression (mashing). Images were reconstructed onto a 128 x 128 image grid using filtered backprojection with a ramp filter and a zoom of 3. These acquisition and reconstruction parameters are consistent with clinical imaging.

The radial (y) and tangential (x) full-width-at-half-max (fwhm) and full-width-at-tenth max (fwtm) values of the PSF were determined for each of 30 planes individually and then averaged. PSF measurements were obtained at various positions along the y-axis between +2.0 and -12.5 cm from the centre of the FOV (field of view). The mean value from several studies (n=3) is reported with $\pm 1\sigma$ quoted as the error.

Several of the PSF profiles were fitted to a Gaussian distribution to test the hypothesis that the PSF could be modeled as a Gaussian. Curve fitting was performed using non-linear least squares fitting. Goodness-of-fit was assessed visually.

3.1.2 Left Ventricular Model

The left ventricular (LV) myocardial wall was modeled as a spherically symmetric LV cavity surrounded by a MYO wall of uniform thickness. The right ventricular (RV) cavity was neglected for simplicity. The LV cavity was set to 34 mm in diameter with a MYO thickness of 10 mm. This is consistent with the dimensions of a normal heart. As

well, the parameters corresponded to the dimensions of the LV cardiac phantom (Data Spectrum, Hillsborough NC) later used for in-vitro investigations.

The LV cardiac phantom also contained a 1.7 mm thick plastic wall separating the LV cavity from the MYO wall and an outer plastic wall of the same thickness. The effect of this plastic wall, which may bias the EV density values, was investigated.

Due to the spherical symmetry employed, one-dimensional profiles were generated and analyzed (similar to Fig. 2.2). One-dimensional activity distributions (or profiles) for the MYO and blood pool (BP) images were defined with an arbitrary activity concentration of 1.0. The transmission (TX) profile was also created with a normalized value of 1.0. Simulated PET images were obtained by convolving these profiles with the one-dimensional scanner PSF. Direct subtraction of the BP from the TX profile yielded the EV profile. Since these simulations were performed to best characterize the methodology under ideal conditions, no noise was added.

The effect of residual BP activity in the MYO was studied. This residual BP activity is typical in many clinical studies due to incomplete tracer uptake and labeled metabolites. MYO profiles with 0%, 10%, 20% and 30% residual BP activity (as a percent of the true MYO value) were simulated.

In 3D PET imaging, emission (EM) and TX images are often acquired with different acquisition parameters. This may result in resolution differences between EM and TX images that may bias the EV values. The effect of TX and EM resolution differences was investigated by varying the fwhm of the PSF of the EM images between 6 mm and 14 mm. The TX PSF was held constant at 10 mm, consistent with clinical practice.

3.1.3 LV Motion Model

Cardiac motion was introduced into the simple LV model to study motion-based PV averaging. The heart was modeled as an ellipsoid with the major axis equal to twice the minor axis. The LV volume was set to 50 mL and 150 mL for the end-systolic and end-diastolic phases, respectively, of the cardiac cycle [90]. An end-diastolic MYO thickness of 10 mm was assumed. The MYO volume remained constant (constant MYO density) while the LV volume varied sinusoidally with a frequency of 60 beats/min ($T=1$ s). All values are consistent with those from a normal heart.

Simulation of motion was achieved by defining MYO, BP, and TX profiles for 16 gates (positions within the cardiac cycle). The 16 gates were summed together and the result convolved with the PSF of the scanner to produce simulated images containing both motion- and resolution-based PV averaging.

3.1.4 Anatomical Heart Model

A more complex model of the heart with surrounding anatomy was developed to further characterize EV density imaging. The simple model described in Section 3.1.2 was extended to approximate the three situations present in a human heart; the lateral, septal, and anterior/inferior walls.

Simulation of the septum was accomplished by adding an RV cavity to the left of the LV cavity. In BP imaging, it is possible for the RV cavity value to exceed that of the LV, particularly if the BP image is formed from the early frames of a dynamic FDG acquisition. The effect of this on the EV density values was investigated by allowing the RV value to vary between 1.0 and 1.2, relative to the LV value.

The lateral wall was simulated by designating the area to the right of the LV MYO wall as lung tissue. The density of lung tissue has been reported to vary between 0.21

g/cm^3 and 0.37 g/cm^3 [1]. TX spillover from the lung may bias the EV values. As well, lung activity, due to lung tracer uptake, may also bias the measured MYO values (see Appendix C). A review of clinical FDG PET images revealed that this lung uptake may vary between 1% and 20%. Both of these effects were studied by simulating lung uptake activities of 0.01, 0.04, 0.10 and 0.20, relative to the MYO activity, for various lung tissue densities.

Finally, the inferior and anterior walls were simulated by setting the density of tissue adjacent to the heart (previously defined as lung) to be equal to the density of MYO tissue. In the anterior wall, this soft tissue is a result of the chest wall while the inferior wall is adjacent to organs such as the diaphragm and liver. The effect of this soft tissue on the EV density values was characterized.

As before, true EM and TX values were set to a value of 1.0. The PSF was approximated as a Gaussian with a fwhm of 14 mm, consistent with clinical imaging. The residual BP activity in the MYO image was set to zero, however, a FBV of 0.1 was assumed. Motion was not included in the anatomical model.

3.2 Results

3.2.1 PSF

The fwhm and fwtm values for both the radial and tangential directions are shown in Fig. 3.1. Tangential and radial fwhm values were found to be 8.4 ± 0.2 mm and 9.1 ± 0.5 mm respectively at the centre of the FOV. At a radial position of 10 cm, the fwhm values were 11.0 ± 0.2 mm and 8.9 ± 1.0 mm in the tangential and radial directions respectively. In subsequent simulations, the intrinsic resolution of the PET scanner was set to 10 mm.

The fwhm values at ± 2.0 cm were approximately equal. This was expected due to the rotational symmetry of the ECAT ART scanner.

A sample of several PSF profiles fitted to a Gaussian distribution are illustrated in Fig. 3.2. Visual assessment of the fits indicated that the measured PSF could be approximated as a Gaussian.

Figure 3.1: Fwhm and fwtm measurements of the PSF for both the tangential (top) and radial (bottom) directions.

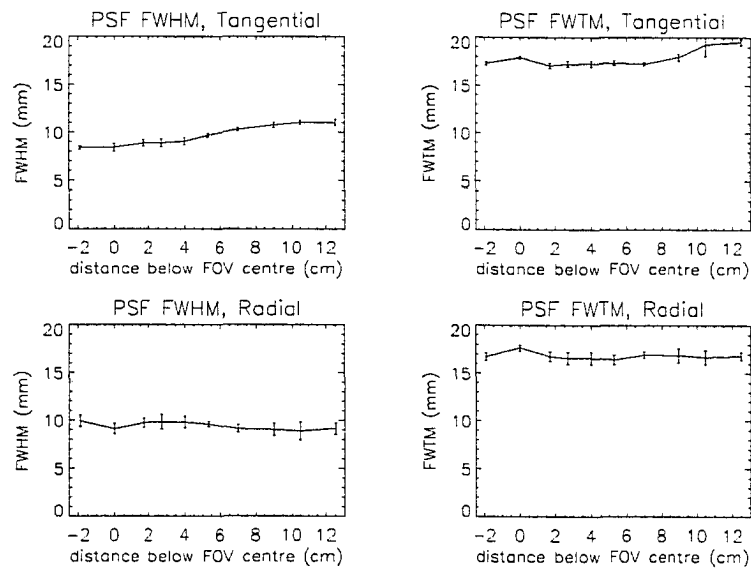
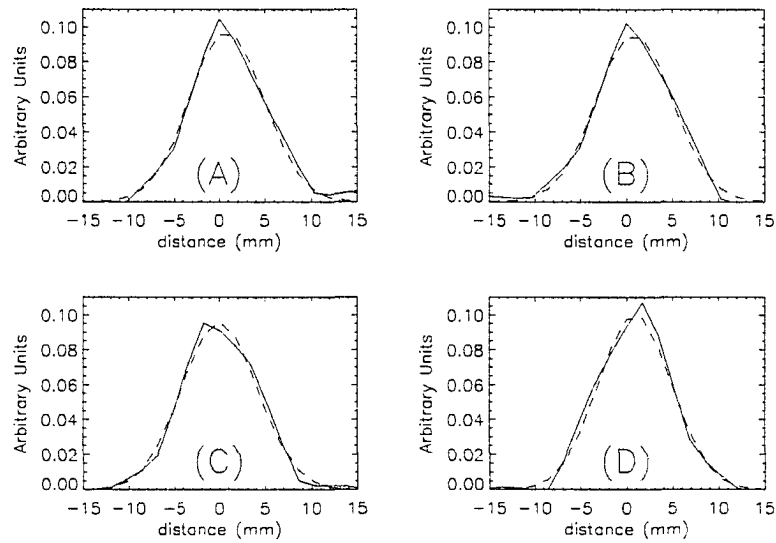


Figure 3.2: Measured PSF profiles (solid line) and fitted Gaussian distributions (dashed line) for: A) radial profile at 0 cm, B) tangential profile at 0 cm, C) radial profile at 7 cm, and D) tangential profile at 7 cm below the centre of the FOV.



3.2.2 LV Model

The simulated profiles for the simple LV model are plotted in Fig. 3.3. The maximum MYO value was 0.78. The corresponding EV value was also 0.78. Division of the measured MYO values by the EV values yielded 1.0, the true activity concentration.

Fig. 3.4 plots the results of added residual BP activity. This residual activity had no effect on the EV image, but biased the measured MYO values. Application of the EV density values to these biased MYO values resulted in an overestimation of the true MYO activity. With a residual BP activity of 30%, the true activity was overestimated by 7%.

The simulated profiles of the LV cardiac phantom are plotted in Fig. 3.5. As before, the maximum MYO value was 0.78. However, the corresponding EV value was found to be 0.93. This resulted in a corrected MYO value of only 0.83. Also plotted are the TX and BP profiles obtained if no plastic wall exists. Comparison of these profiles to those obtained with the plastic wall indicated an inward shift of the edge of the BP profile, and an outward shift of the edge of the TX image. This caused an overestimation of the EV values.

The effect of TX and EM resolution mismatch is shown in Fig. 3.6. A smaller EM resolution kernel resulted in an overestimated true MYO value, while a larger resolution kernel underestimated the true MYO value. EM resolutions of 6 and 14 mm resulted in corrected MYO values of 1.09 and 0.88 respectively.

Figure 3.3: Simulated profiles of the LV model. The dashed line represents the true MYO activity distribution. Subtraction of the BP from the TX yields the EV profile. The EV and MYO profiles are identical indicating that peak MYO/EV would yield the true MYO activity.

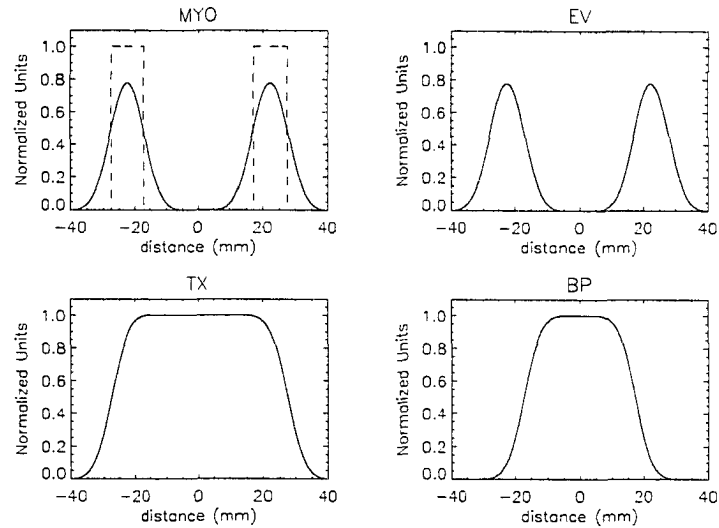


Figure 3.4: (left) MYO profiles with 0% and 30% residual BP activity. (right) Effect of the residual BP activity on PV correction. The EV density values remain constant but the peak MYO values are biased, resulting in overestimated corrected MYO values.

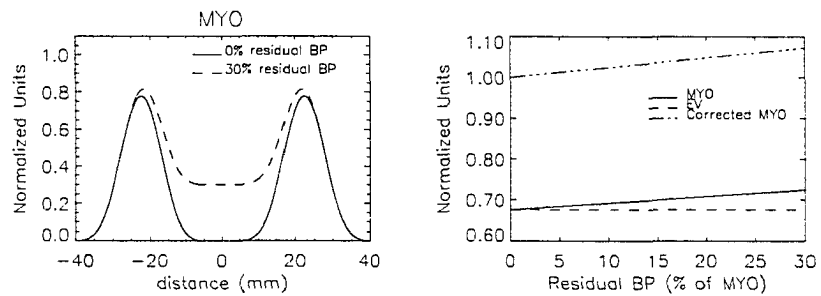


Figure 3.5: Simulated profiles of the LV phantom model with 1.7 mm plastic walls. The TX and BP profiles obtained without inclusion of the plastic walls are also shown (dashed line). The plastic walls cause the EV profile to be overestimated by mispositioning the edges of the BP and TX images.

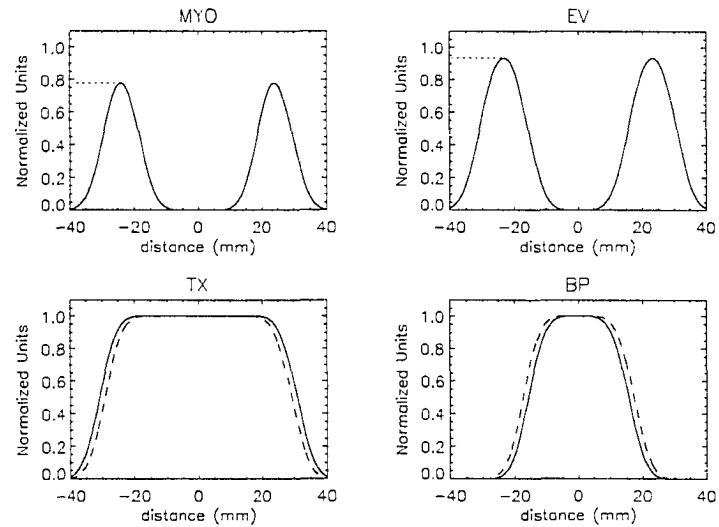
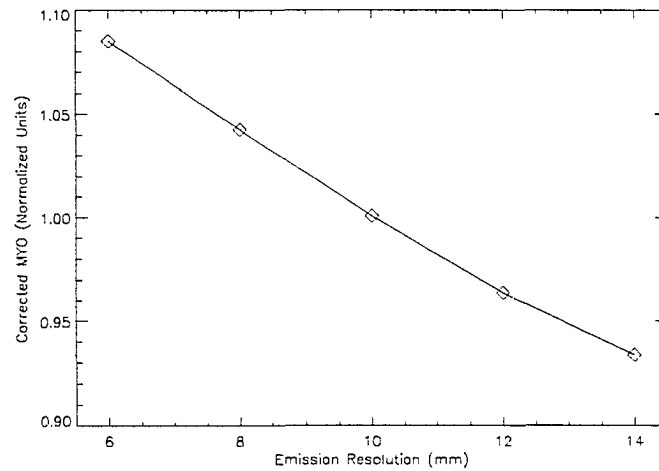


Figure 3.6: Effect of EM resolution on the peak corrected MYO value. The TX resolution was kept constant at 10 mm fwhm.



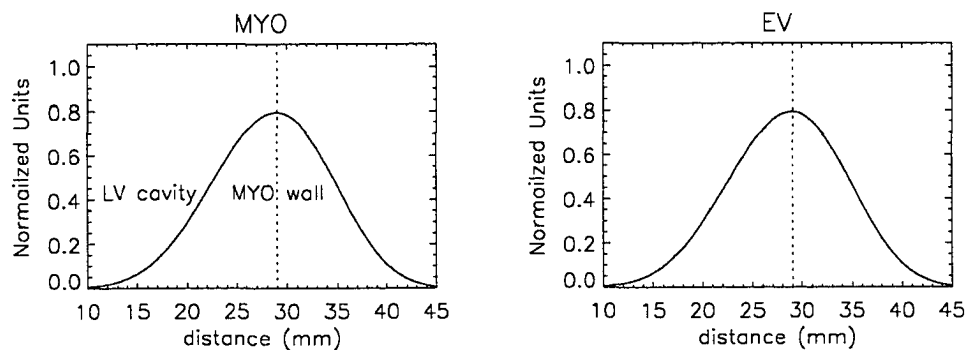
3.2.3 LV Motion Model

The MYO and EV profiles for the cardiac motion model are shown in Fig. 3.7. The average MYO thickness was 11.9 mm, with an end-diastolic to end-systolic thickening of 45.9%. The mean distance from the centre of the BP cavity to the middle of the MYO wall was 28.9 mm, similar to that of a normal heart.

The peak MYO value was measured to be 0.79. The corresponding EV value was identical, allowing for accurate recovery of the true MYO activity of 1.0.

Inclusion of cardiac motion resulted in a slight asymmetry of the myocardial profile, biased towards the outer edge of the myocardium (epicardium). This is a result of the constant MYO density. As the heart contracts, the muscle thickens and the peak MYO tissue position is biased towards the outside of the MYO wall.

Figure 3.7: Simulated profiles of the sinusoidal cardiac motion model. (Only one of the MYO walls is shown) The EV profile is identical to the MYO profile, indicating full recovery of PV effects is possible within the MYO wall. The dashed line represents the position of the maximum MYO value.



3.2.4 Anatomical Heart Model

Fig. 3.8 is a plot of the profiles obtained using no EM or TX spillover from pericardial structures and equal RV and LV cavity values in the BP image. The true MYO activity within the MYO wall was seen to be 0.9, due to the introduction of a 10% vascular space (see Appendix C). Under these conditions, the EV density was able to exactly characterize PV averaging in both the septum and lateral walls.

Increased RV cavity values, relative to the LV value, resulted in an increase of the BP values within the septum, and an underestimation of the corresponding EV density values. Fig. 3.9 illustrates the effect of variable RV values on the corrected septum values. A RV/LV ratio of 1.20 resulted in an overestimation of the true septum activity by 9%.

Fig. 3.10 plots the results of variable lung density and lung activity on the corrected MYO values. Tracer uptake in the lung resulted in biased measured MYO values, overestimating the corrected values. However, increased lung density lead to TX spillover into the lateral wall that biased the EV values and underestimated the true MYO activity.

Fig. 3.11 illustrates the results for the inferior and anterior walls segments. TX spillover from adjacent soft tissue (organs or chest wall) caused an overestimation of the EV density values. From the simulation, the MYO activity was measured to be 0.57 with a corresponding EV value of 0.76. Application of the EV density value yielded a corrected MYO value of 0.75, a 25% underestimation of the true activity.

However, Fig. 3.11 indicated that this overestimation is most severe in the epicardial region. Sampling the MYO wall 2 mm closer to the LV cavity (relative to the centre of the MYO wall) resulted in measured MYO and EV values of 0.48 and 0.52 respectively, yielding a corrected value of 0.92 for the true activity.

Figure 3.8: Profiles obtained using an anatomical heart model. True MYO values (solid line) are reduced to 0.9 due to the 10% vascular component. Within the septal (SEP) and lateral (LAT) walls, the EV profile is identical to the simulated MYO profile, indicating exact correction of PV averaging in both MYO walls.

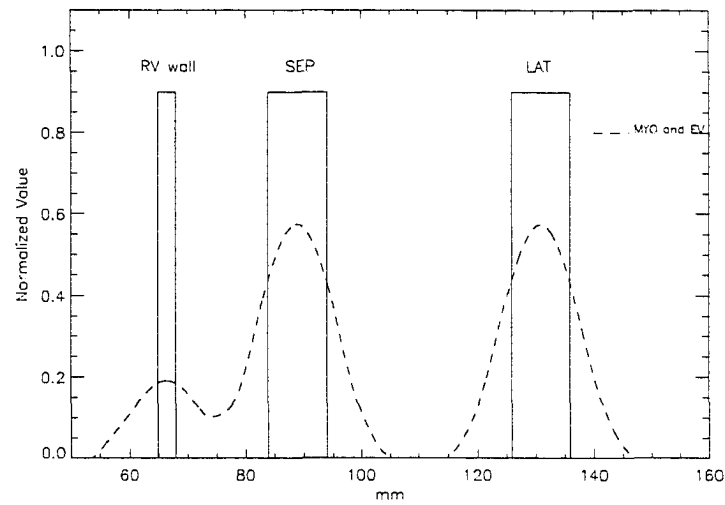


Figure 3.9: Plot of the effect of variable RV values in the BP image. EV values are biased, resulting in an overestimation of the true peak activity within the septal wall.

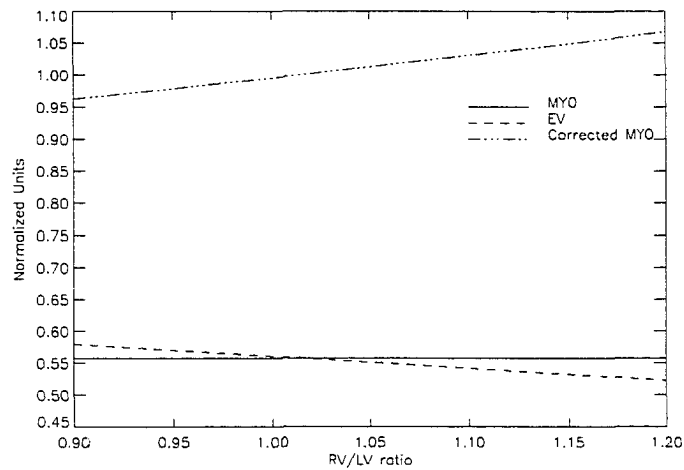


Figure 3.10: Effect of lung density and lung activity on the peak corrected MYO values. Increased activity biases the measured MYO values resulting in an overestimation of the corrected MYO. Increases in lung density bias the EV values, resulting in an underestimation of the true activity.

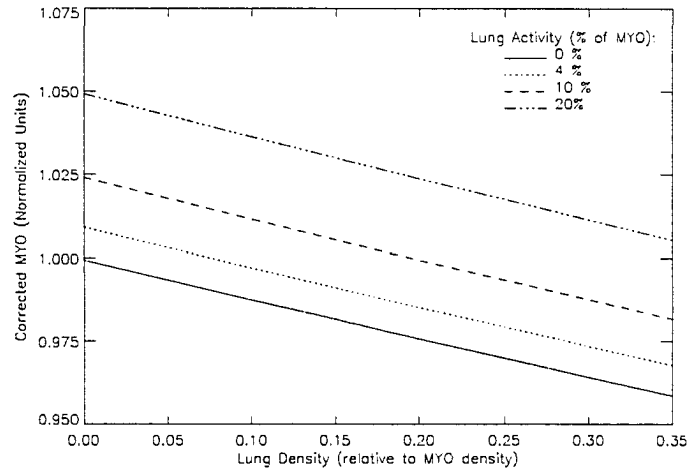
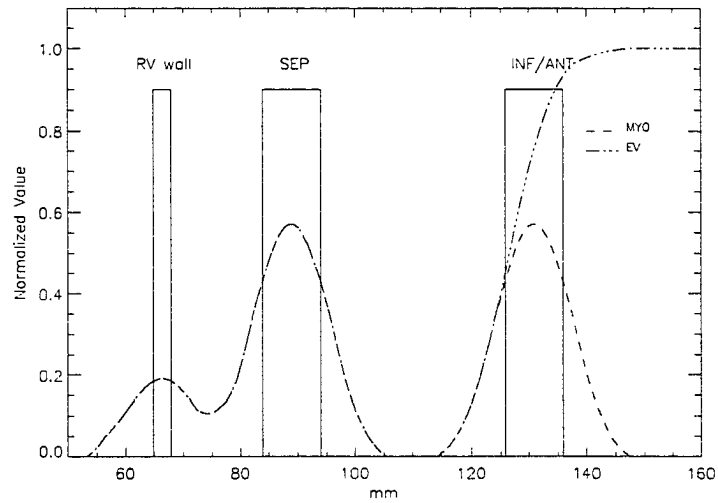


Figure 3.11: Profiles of the inferior/anterior wall. TX spillover from either the chest wall or adjacent organs resulted in an increase in the measured EV values in the inferior/anterior wall. This would undercorrect for PV averaging in these walls.



3.3 Discussion

A methodology has been developed to simulate PV effects. The simulated PET profiles were used to characterize PV averaging and the use of EV density imaging for PV correction.

One of the limitations of this methodology is the use of one dimensional activity profiles instead of three dimensional images. However, if the MYO activity is constant in the other two dimensions, then PV losses are a one dimensional effect. This is a reasonable approximation of the myocardium, where PV losses occur along the radial dimension from the centre of the LV cavity. The work presented was not an attempt to fully characterize the ECAT ART, but rather to study the use of EV density imaging under common clinical conditions.

3.3.1 PSF

The transaxial PSF, measured using a line source, was found to be well characterized by a Gaussian distribution with a fwhm of 10 mm. This is referred to as the intrinsic resolution of the scanner and does not include smoothing applied during image reconstruction.

The fwhm of the radial PSF was found to be relatively constant over the FOV, while the tangential PSF degraded further from the center of the scanner. These results are consistent with those reported for our scanner by Bailey et. al. [69]. However, in PET imaging, the PSF is typically expected to degrade in the radial direction. This was the result reported by Wienhard et. al. [91] for the ECAT EXACT, which is the full-ring version of the ECAT ART. It is believed that our results may be due to the rotational nature of the scanner.

One of the limitations of the PSF measurement is that, even in the transaxial plane,

the needle only approximates a point source due to its finite width of 1.3 mm. Further simulations, not presented in this thesis, of this geometry showed that this finite width would result in a $\sim 3.5\%$ increase in the measured fwhm. This would alter the absolute measured values of the MYO, BP, TX, and EV profiles. However, the relative values, i.e. MYO/EV, would remain unchanged as long as the PSF for the images was identical.

Another limitation is that the PET scanner was assumed to be a shift invariant system. This assumption was violated since the PSF was found to vary by approximately 2.5 mm over 10 cm in the FOV. However, Eq. 3.1 can still be used as an approximation if the simulation is performed within a small area of the FOV such that the PSF remains unchanged. Furthermore, the relative MYO/EV value would remain unchanged as above, as long as EM and TX resolution vary together.

3.3.2 LV Model

Simulations of a simple LV geometry indicated PV averaging resulted in a 32% underestimation of the true MYO activity, consistent with published phantom study results [9, 13]. In these ideal conditions, the EV density image was able to exactly correct for this PV averaging.

The effect of residual BP activity is important as most clinical studies may have anywhere between 5% and 35% BP activity in the MYO image due to incomplete tracer uptake or labeled metabolites. The EV density image is not able to correct for this overestimation as it is not due to PV effects, as discussed in Appendix C. Subtraction of a high quality, normalized BP image may be able to remove this bias. Such a correction was utilized in the in-vivo studies described in Chapter 6.

Simulation of the LV cardiac phantom showed that the plastic walls separating the chambers caused the edges of the BP and TX profiles to shift away from the MYO re-

gion. The outer plastic wall caused a broadening of the TX image, relative to the MYO, while the inner plastic wall diminished the BP region size. The result was increased EV values which underestimated PV averaging within the MYO wall. This effect will be problematic for all phantom studies, the magnitude of which will depend on the thickness of the plastic. This problem is potentially correctable using morphological operators such as dilation and erosion, as discussed in Chapter 4 and Chapter 5.

The simulations were also able to characterize the effect of mismatched EM and TX resolutions. The EV density correction assumes that PV averaging of the MYO wall is identical to TX spillover and the complement of BP spillover. This is only true if the resolutions of the images are matched. In 3D imaging, the TX image is typically acquired with acquisition parameters different from that used for EM imaging, resulting in a potential resolution mismatch of the TX and EM images.

3.3.3 LV Motion Model

Inclusion of cardiac motion resulted in an asymmetric myocardial profile. However, simulations showed that the EV density method was still able to exactly correct for PV averaging resulting from non-linear cardiac motion.

In the model, the LV chamber volume was assumed to vary sinusoidally. However, previous studies have shown the cardiac cycle to be more complex in nature [90, 92]. Applying a more physiologically correct motion model (such as one that may also include compression of the MYO wall during contraction) would change the absolute MYO and EV values, but not the ratio of the two. The MYO and EV profiles would still be identical and thus the EV image could be used to correct for PV losses, regardless of the actual form of the motion. The choice of sinusoidal motion was based on ease of implementation.

3.3.4 Anatomical Heart Model

Simulation of the more anatomically accurate heart model indicated that either pericardial activity or tissue density can bias the MYO and/or EV values. Tracer uptake in structures such as the lung or liver results in increased measured MYO values which cannot be corrected for using the EV density image. Residual BP activity, assumed to have been removed in these simulations, would also cause bias. It may be possible to remove the residual BP effects through direct subtraction of the BP image from the MYO image, as described for ^{15}O -water studies [2] and in Chapter 6. The same method could be used to remove pericardial activity effects, if a PET image of only the pericardial structure could be obtained. Factor analysis, which aims to extract a pure physiological image from a dynamic data set [93, 94], may prove useful in this regard.

In the septum, TX spillover from the RV cavity was compensated for exactly by RV activity spillover in the BP image. However, increased RV values in the BP image, relative to the LV, would result in decreased EV values and an overestimation of the PV effect. This is potentially a problem if the BP image is formed using the early frames from a dynamic study. However, one of the first frames in a dynamic study is typically an RV-only image. This image has the potential to correct for increased RV/LV ratios.

A larger challenge may be the effect of pericardial organs on the EV image. Soft tissue, adjacent to the heart, was found to effectively remove or reduce the edge of the TX image from the MYO wall. This resulted in an overestimation of the EV density values and an underestimation of the true activity.

As seen in Fig. 3.10, the effect of pericardial TX spillover can be offset by an increase in activity spillover from the same organ. However, the amount of TX and activity spillover cannot be accurately predicted and so it is best to remove both of these confounding effects.

Currently, no simple method of removing pericardial structures from the TX images exists. Methods involving segmentation of a high-resolution anatomical image (such as a CT or MRI) may potentially be used, but involve challenges with image registration and resolution matching. In Section 3.2.4, shifting the MYO sampling point towards the LV cavity (as opposed to sampling the centre, or maximum value, of the MYO wall) was found to minimize the effect of spillover due to the pericardial structures, and produced a more accurate PV correction.

Chapter 4

Left Ventricular Cardiac Phantom

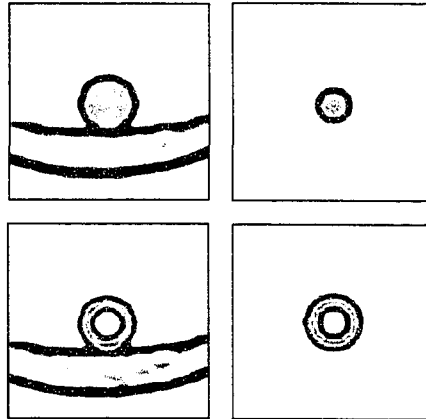
The results presented here are adapted from those published in IEEE Transactions on Nuclear Science [13]. As well, this work has been presented at the 2002 IEEE Medical Imaging Conference [12].

4.1 Methodology

Measurements were performed using a left ventricular (LV) cardiac phantom (Data Spectrum, Hillsborough N.C.). The phantom consisted of two concentric chambers resulting in a LV cavity and a MYO wall of constant thickness (see Fig. 4.1). The LV cavity was 34 mm in diameter while the MYO wall was 10 mm thick. The chambers were bounded by plastic walls 1.7 mm thick.

Filling of either the LV or MYO chambers with ^{18}F provided the BP or MYO images respectively. 3D emission data were acquired with the default axial sampling ($\Delta r/\text{span}$ of 17/7), Fourier rebinned, and were reconstructed with no added smoothing (all-pass Ramp filter) using filtered backprojection. Transmission data was acquired in 2D mode ($\Delta r/\text{span}$ of 4/9, no septa) and was reconstructed using filtered backprojection from an attenuation file with the default 8 mm Gaussian smoothing. MYO images were

Figure 4.1: (clockwise, from top left) Transaxial slices of the TX, BP, MYO and EV images of the LV cardiac phantom.



normalized as a fraction of the actual activity present to give values in the range of 0 to 1. This allowed for the comparison of several studies ($n=7$).

Normalization values for both the TX and BP scans were obtained by first averaging 15 transaxial slices. The normalization value was obtained as the mean value from a ROI 5 cm in diameter, co-centric with the centre of the BP image. After normalizing both images, the BP was subtracted from the TX image to provide the EV density image, as given by Eq. 2.1 (with $\rho=1.0$ for water). Examples of the MYO, BP, TX and EV image are shown in Fig. 4.1

Prior to calculation of the EV density image, the effects of the plastic walls (1.7 mm thick) of the phantom's MYO chamber were removed. This was necessary since failure to do so resulted in a overestimation of the EV density values, as described in Chapter 3. Removal of the walls was accomplished through the use of the 3D morphological operators, dilation and erosion. These operators shifted the edges of the BP and TX images without altering the slope [95]. Dilation of the BP image removed the effects of the inner wall as shown in Fig. 4.2. The effect of the outer wall was removed by eroding the TX image as shown in Fig. 4.3.

Figure 4.2: Profiles through a transaxial slice of the BP image before (solid) and after (dash) application of the dilation operator. The dilation operator expanded the image without altering the slope of the edge. This placed the edge of the BP next to the MYO region, as it would be if no plastic wall were present.

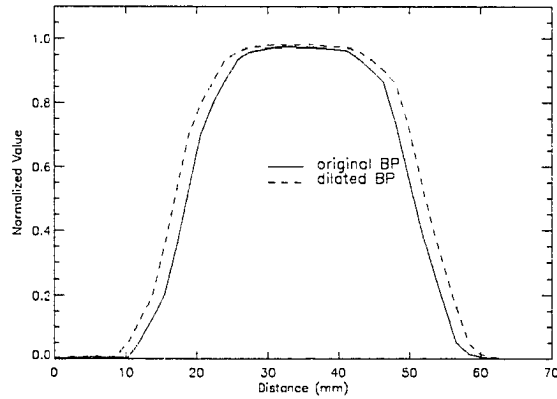
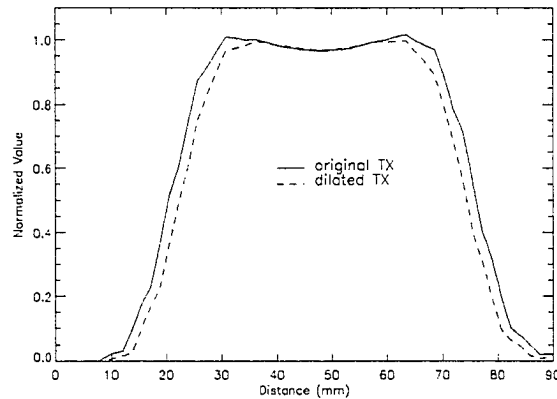


Figure 4.3: Profiles through a transaxial slice of the transmission image before (solid) and after (dashed) application of the erosion operator. This operator places the edge of the TX next to the MYO region as desired.



The global mean value from a ROI encompassing the entire MYO wall was determined for both the MYO and EV images. The corrected MYO value was obtained by dividing the measured MYO value by the EV density correction, as given by Eq. 4.1.

$$MYO_{true} = \frac{MYO_{measured}}{EV} \quad (4.1)$$

The effect of ROI size was then investigated by defining uncorrected MYO and EV polar maps (see Appendix A) using spherical ROIs ($n=540$) evenly distributed around the myocardium. The ROI diameter was varied between 2 and 10 mm. A corrected MYO polar map was created by dividing the uncorrected MYO polar map by the EV density polar map. The mean for each polar map was calculated and averaged over the studies ($n=7$).

4.2 Results

Using the global ROI mean, the uncorrected MYO activity was measured to be 0.68 ± 0.02 , after normalization to the true injected activity ($p < 0.001$ vs 1.0). This 32% underestimation of the MYO activity was due solely to PV effects. The EV density value for the same ROI was found to be 0.79 ± 0.02 g/cm³. Applied, this gave a corrected MYO value of 0.87 ± 0.04 , still significantly less than the true value of 1.0 ($p < 0.001$). After accounting for the phantom's plastic walls through the use of the dilation and erosion operators on the BP and TX images respectively, the EV density value was measured to be 0.67 ± 0.02 g/cm³. This yielded a corrected MYO value of 1.02 ± 0.04 , which was not significantly different than the true value of 1.0.

The effect of ROI size on the EV correction is illustrated in Fig. 4.4. The corrected MYO values were seen to range from 1.01 to 0.96. The EV density image was able to

correct for PV averaging to within 5% for diameters of 2 - 10 mm. However, a small bias was evident. The average uncorrected MYO values decreased at a greater rate than the EV density value, as ROI diameter was increased. This may be due to a slight resolution mismatch of the emission and transmission images.

Fig. 4.5 illustrates the corrected MYO values when emission images were reconstructed with added Gaussian smoothing. For a fwhm of 3 mm, the corrected MYO values systematically increased, but maintained a similar slope. The values subsequently decreased as more smoothing was introduced. At 9 mm, the average corrected MYO value was 0.90, an underestimation of 10%. However, the range of the values for 9 mm smoothing was only 1.6%. This was an improvement over the 5.4% range seen with no smoothing.

Figure 4.4: Effect of ROI size on the EV density correction. The uncorrected MYO (dash) and EV density (dot) values diverge at larger diameters, causing the corrected MYO image (solid) to be underestimated.

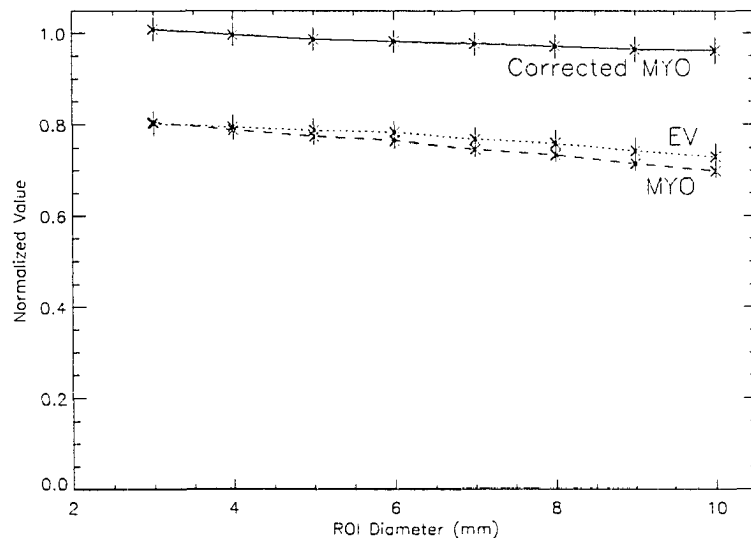
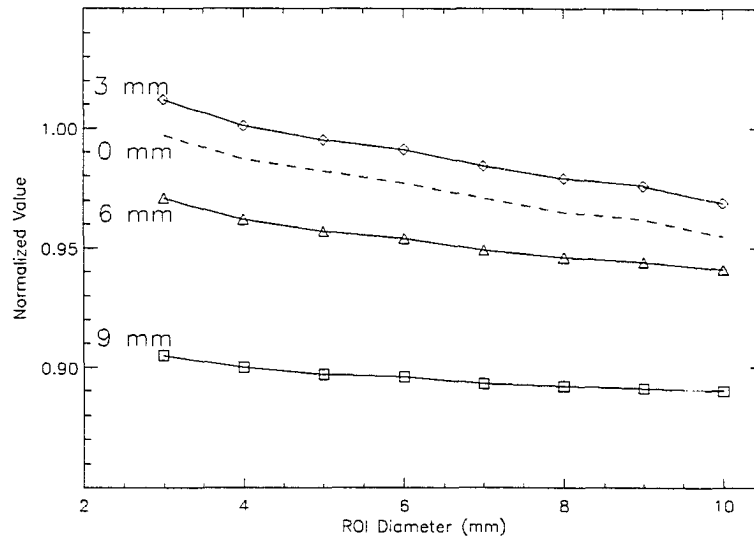


Figure 4.5: Effect of emission image smoothing on the corrected MYO values. Gaussian smoothing of 0 mm (dashed), 3 mm (diamond), 6 mm (triangle) and 9 mm (square) was applied during emission reconstruction to match transmission and emission resolutions. As the fwhm is increased, the values become more independent of the ROI diameter. However, the average value for all diameters is initially increased for 3 mm smoothing and then subsequently decreases as the fwhm is increased. Error bars have been omitted for clarity. Average error for the measurements was $3.6 \pm 0.2 \%$.



4.3 Discussion

The initial failure of the EV density correction was a result of the construction of the phantom. Plastic barriers 1.7 mm thick form the walls of the MYO chamber. This effectively shifted the edge of the BP away from the MYO region. This shift caused lower BP values to be subtracted from the TX image within the MYO region. At the same time, the outer phantom wall caused an outward shift of the TX image away from the MYO chamber. This resulted in increased TX values within the MYO region. The combined effect of the plastic walls was an overestimation of the EV density values. This problem had been previously reported, but no means of correction was discussed [9]. The 3D morphological operators, dilation and erosion, were successfully used to

shift the edges of the BP and TX images adjacent to the myocardial region as desired, without altering their shapes (Fig. 4.2 and Fig. 4.3).

The reason for the bias seen at large ROI diameters may be due to the resolution mismatch between emission and transmission images. As stated earlier, the transmission data was acquired in 2D mode with additional smoothing (8 mm Gaussian) of the attenuation correction file used for TX image reconstruction. The emission images were acquired with different axial sampling and no smoothing of images. Due to these acquisition and reconstruction differences, a slight resolution mismatch, on the order of several millimeters, may be expected. The divergence of the MYO and EV density values for larger ROIs indicated that the peak values of the two images was approximately equal. However, the MYO image exhibited a slightly sharper peak, accounting for its more rapid decrease as ROI diameter increased and more pixels were included in the ROI mean. Gaussian smoothing was applied to the emission images in an attempt to match resolutions. When 9 mm of smoothing was introduced, the bias was nearly removed. However, the increased smoothing caused the MYO values to be reduced. This was not compensated for by the EV density correction indicating that adding smoothing to either the emission or transmission images may not be enough to correct for differences in resolution due to acquisition parameters. However, it should be noted that, even in the worst case of no smoothing, the values in Fig. 4.5 differed by only 5.4%. The EV density image is able to correct for PV effects to within 5% for a ROI diameter of 10 mm. The resolution mismatch in human studies may be more severe than in phantom studies, since more smoothing is typically performed on the emission image. Appropriate smoothing of both the transmission and emission images will be required to match resolutions. The method outlined in this chapter, using Fig. 4.4, may provide a simple means of assessing bias from resolution mismatch.

The static nature of the phantom precludes investigation into the effectiveness of the EV density correction for motion-based PV averaging using this phantom. Cardiac motion would change the shape of the emission profiles through the myocardial wall

and could change the sensitivity to ROI size slightly. However, as discussed in Chapter 3, the EV method does not make any assumptions about the source or shape of the blurring function, i.e. scanner resolution versus cardiac motion. It only requires that the emission and transmission images are blurred by the same function. Typical emission and transmission scan times result in the averaging of many cardiac cycles. If cardiac motion remains constant throughout all image acquisitions, then the amount of motion-induced blurring will be equal in both emission and transmission images.

The EV method is designed to correct for PV averaging within the MYO wall by converting the measured activity per unit volume into activity per mass of nonvascular tissue. This should remove both resolution- and motion-induced PV artifacts. It will also remove the total vascular component of the myocardium (approximately 0.10 ml/g [2]), as discussed in Chapter 2. The effect of this vascular fraction cannot be assessed with the phantom.

Lastly, the LV cardiac phantom represents a normal heart (10 mm thick). The MYO thickness of diseased hearts may vary from 3 mm to 25 mm or more. The effect of this variable MYO thickness cannot be studied with this phantom. In the next chapter, a different phantom is used to assess EV imaging for more clinically representative MYO thicknesses.

Chapter 5

Variable Wall Cardiac Phantom

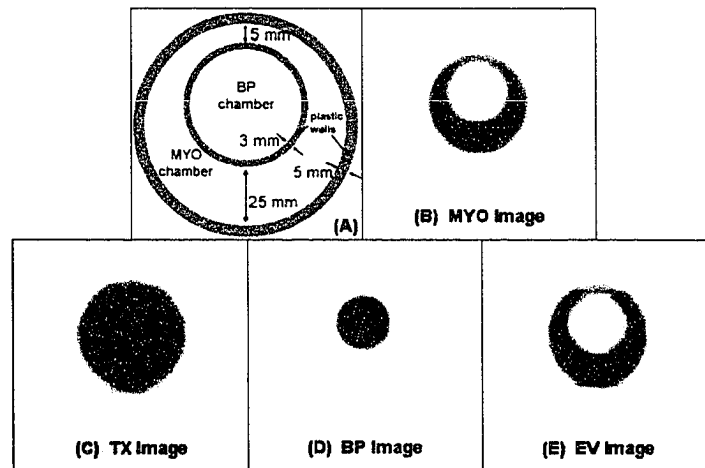
The results of this chapter have been presented at the 2004 IEEE Medical Imaging Conference [14]. As well, they were submitted as a paper to the IEEE Transactions on Nuclear Science. This chapter has been adapted from the manuscript submitted for publication.

5.1 Methodology

Scans were performed using the CEC variable-wall LV Cardiac phantom (PTW, Hicksville, NY). The phantom consisted of an inner cylinder inside of a larger cylinder producing both a BP and MYO chamber as shown in Fig. 5.1. A MYO thickness varying between 5 mm and 25 mm was achieved by offsetting the centres of the two chambers. The outside and inside plastic walls of the MYO chamber were 5 mm and 3 mm respectively [96].

Emission data was acquired using a $\Delta r/\text{span}$ of 17/7, Fourier rebinned, and reconstructed using filtered backprojection with an all-pass Ramp filter. Transmission (TX) data was acquired with a $\Delta r/\text{span}$ of 4/9 and reconstructed using filtered backprojection and an all-pass filter.

Figure 5.1: Transaxial slices of: A) a schematic of the variable-wall phantom, B) MYO, C) TX, D) BP, and E) EV density images. The MYO and BP images were obtained by filling the appropriate chamber with ^{18}F . The TX image was acquired by filling both chambers with water.



Filling of the appropriate chamber with ^{18}F yielded the MYO and BP images. Filling of both chambers with water yielded the TX image (Fig. 5.1). MYO images were normalized as a fraction of the actual activity present to give values in the range of 0 to 1. This allowed for the comparison of several studies.

The EV density image was created according to Eq. 2.1, with $\rho=1.0$ for water.

Initial scans were performed with only the variable wall phantom present in the field of view (FOV) ($n=8$). Subsequent scans ($n=5$) placed the phantom inside a chest cavity partially filled with water to remove TX ring artifacts.

MYO values at various wall thicknesses were determined using 5 mm radius ROIs centered within the MYO wall. Identical regions were defined on the co-registered EV density image to obtain the PV correction factors. Both uncorrected and corrected

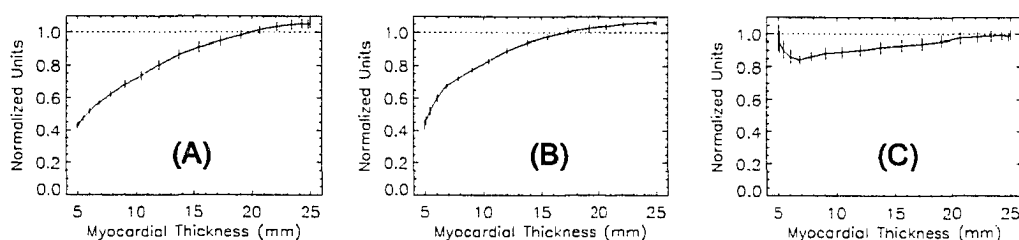
MYO values were plotted as a function of wall thickness.

From Chapter 3 and Chapter 4, the plastic walls separating the BP and MYO chambers are known to produce artifacts in the EV image by mispositioning both the BP and TX edges, relative to the MYO chamber. The morphological operators dilation/erosion were applied to the BP/TX images using a spherically shaped structuring array, to account for the plastic walls in the variable wall phantom. Briefly, dilation was applied to the BP image to expand the image by an amount equal to the thickness of the plastic wall (3 mm) without altering the shape of the edge. The resulting image was equivalent to one where no plastic wall was present and the BP chamber extended to the edge of the MYO chamber. Similarly, erosion was applied to the TX image to account for the 5 mm outside plastic wall.

A second method to account for mispositioning of the BP/TX edges was also developed. Instead of transposing the myocardial ROIs on the EV image directly, the ROIs were instead transposed onto the BP and TX images with offsets corresponding to the plastic wall thickness. For example, the 3 mm thick plastic wall separating the BP from the MYO chamber causes the edge of the BP to be shifted inward by 3 mm. The placement of the MYO ROIs, on the BP image, was then also shifted inward by 3 mm to obtain the BP values as if no plastic wall was present. Similarly, the TX ROIs were appropriately shifted outward by 5 mm. The EV density values were then calculated on a regional basis, as given by Eq. 5.1. This is in contrast to the initial methodology in which an EV density image was created.

$$EV_{ROI} = TX_{ROI} - BP_{ROI} \quad (5.1)$$

Figure 5.2: (A) Measured MYO values for the variable-wall phantom. PV losses cause a 60% underestimation of the activity at 5 mm. (B) Corresponding EV values and (C) PV corrected MYO values. The dilation/erosion operators were applied to the BP/TX images prior to EV image creation. At thicknesses <7 mm, the EV values exhibit a different curvature due to image artifacts. The corrected MYO values at these thicknesses are inaccurate, despite the apparent improvement seen.



5.2 Results

The initial results obtained with only the variable-wall phantom in the FOV, and using dilation/erosion to correct for the phantom's plastic walls, are illustrated in Fig. 5.2. The uncorrected MYO value was measured to be 0.43 at a wall thickness of 5 mm. Full recovery of the true activity was measured for thicknesses of approximately 20 mm and greater. This is consistent with the general rule that PV effects become negligible at twice the fwhm resolution.

The corresponding EV values followed the same pattern, with values of approximately 0.44 and 1.05 at thicknesses of 5 mm and 25 mm respectively. Application of the corresponding EV correction values improved the accuracy of the MYO values for both thin and thick regions of the myocardium.

The EV values at thicknesses less than 7 mm exhibited a different curvature due to an overestimation of the TX values. This resulted in a relative overestimation of corrected MYO values at these thicknesses. Although the corrected activity at 5 mm appeared to be close to the true value of 1.0, it was actually overestimated due to the

TX overestimation arising from image artifacts. These artifacts were thought to be due to both a ring artifact in the TX image and artifacts introduced by the use of the morphological operators.

The TX ring artifacts were reduced by placing the cardiac phantom within the chest phantom, partially filled with water, as shown in Fig. 5.3. Fig. 5.4 shows the results obtained using the chest phantom to reduce the ring artifacts. At 5 mm, the uncorrected myocardial value was 0.43. Application of the corresponding EV values (obtained using the method of morphological operators) improved the accuracy of the MYO values to 0.79 and removed the false minimum seen previously in Fig. 5.2.

Further improvement was demonstrated when the EV values were obtained using the method of adjusted ROIs. As illustrated in 5.4, a recovery of 0.89 was obtained at a MYO thickness of 5 mm.

Figure 5.3: (left) Transaxial slice of the TX image of the variable-wall phantom. Due to scatter differences with the reference scan, ring artifacts (arrows) can appear. (right) By imaging the variable-wall phantom inside of the chest phantom, partially filled with water, the ring artifacts are reduced.

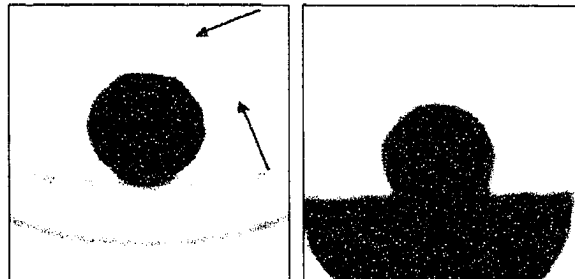
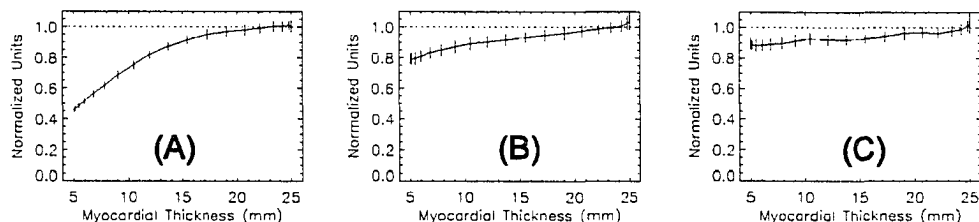


Figure 5.4: (A) Measured MYO values obtained with the variable-wall phantom placed inside the chest phantom. (B) PV corrected MYO values. Dilation/erosion were applied to the BP/TX images prior to EV image creation. Values are still underestimated by $\sim 20\%$ at 5 mm (C) PV corrected MYO values, where the EV values were calculated from adjusted BP/TX ROIs. This method leads to better EV estimates, recovering $\sim 90\%$ of the activity at 5 mm.



5.3 Discussion

PV averaging led to a 60% underestimation of the MYO activity at a wall thickness of 5 mm. Full recovery was obtained for thicknesses greater than 20 mm (twice the fwhm). Application of the EV density correction improved the recovery to 90% at 5 mm.

Phantom studies were performed to model the in-vivo imaging conditions under a more controlled environment. In this chapter, measurements with a simple variable-wall phantom were used to assess the feasibility of the methodology. However, the plastic walls separating the BP and MYO chambers complicated the analysis as in the previous phantom study (Chapter 4). These walls are not present in-vivo.

Data were initially biased due to the presence of TX ring artifacts, a known artifact that can arise from scatter differences between transmission and reference scans [55, 54]. For this reason, the reference scan on the ECAT ART is acquired with a large attenuating slab in the field of view, so that transmission and reference scatter are matched for patient scans. However, the variable-wall phantom is much smaller and therefore has less scatter than the reference scan, which resulted in slight ring artifacts in the

TX image. This artifact was amplified by the rotational nature of the scanner and the circular symmetry of the phantom. Use of the partially filled chest phantom increased the scatter within the FOV, removed the circular symmetry, and reduced the TX ring artifacts.

Another issue believed to be related to scatter was the overestimation of the measured myocardial activity at thicknesses greater than 20 mm (Fig. 5.2). However, the EV values were also overestimated, so that the corrected myocardial values were 1.0, the true expected value. The reason for this overestimation is believed to be due to scatter in various images. As discussed above, transmission ring artifacts can arise, overestimating TX values, and subsequently, EV values. As well, decreased scatter in the transmission image, relative to the reference scan, can result in increased measured linear attenuation coefficients (μ). This increase in μ values is expected to be non-uniform across the phantom, and may result in a non-uniform attenuation correction. Combined, these effects may have resulted in the overestimated MYO values, and the corresponding EV overestimation.

A means of accounting for the presence of the phantom's plastic walls was required to prevent further biasing of the EV values, as described in Chapter 3. In Chapter 4, the dilation and erosion operators were successfully used to remove the effect of the plastic wall. In this chapter, a method involving adjusted ROIs was found to provide a more accurate means of accounting for the phantom's plastic wall, compared with the use of the morphological operators.

Application of dilation and erosion expands or contracts an image by an integer number of pixels. In order to obtain 5 mm or 3 mm morphing, the image must be resampled onto a new grid spacing such that these measurements correspond to an integer number of pixels. This resampling can introduce some smoothing into the image. As well, on a coarse grid, the morphological operators are non-isotropic. That is, they do not contract or expand an image equally in all directions. Careful choice of the

structuring array may reduce this non-isotropic behaviour.

The use of the morphological operators was not seen to be a problem in Chapter 4, since in that instance, the plastic wall corresponded to the size of one pixel, and the image did not need to be resampled. Also, the MYO wall of the LV phantom was 10 mm thick and the values were obtained near the centre of the MYO wall. The non-isotropic behaviour of the operators would primarily affect the edges of the images. These edges are important when the MYO wall is thin, but become less significant as the MYO wall increases in thickness. As well, the results of the previous phantom study were averaged over the angles. By averaging over the angles, the non-isotropic effects of the operators was reduced. With the variable-wall phantom, the MYO thickness varies with angle and so the data cannot be averaged in the same way.

Although the methods of morphological operators and adjusted ROIs were able to account for the spatial extent of the plastic walls, incomplete recovery of activity was still found (Fig. 5.4). Further analysis of the phantom's physical construction revealed that the plastic walls had a linear attenuation coefficient slightly larger ($\sim 5\%$) than that of water. This may have contributed to the overestimation of the TX values which biased the EV values. This could partially explain the incomplete activity recovery at small myocardial thicknesses. At larger thicknesses, the myocardial ROIs are further from the phantom's plastic wall and are thus unaffected.

Another reason for incomplete activity recovery may be resolution differences between transmission and emission images, as well as ROI size. In Chapter 4, it was found that ROI size and resolution mismatch could cause a 5% error in EV estimates.

The potential of EV density imaging as a means of PV correction was demonstrated in this chapter for MYO thicknesses varying between 5 mm and 25 mm. Unfortunately, issues with the phantom's construction complicate further characterization of the methodology. A phantom with thinner plastic walls, as used in a study by Spinks

et. al [9], could reduce some of this artifact. However, Spinks found that the problem of TX spillover from the plastic wall was still present. At 5 mm, Spinks reported that the EV value could recover 90% of the true activity, which is consistent with our value (see Fig. 5.4). In the study by Spinks, no correction for the plastic wall was made. As well, the phantom was surrounded by wood shavings ($\rho=0.12 \text{ g/cm}^3$) to simulate lung density. The lung density and plastic wall resulted in TX spillover, which overestimated EV values. In our study, the overestimation is believed to be partially due to an inability to account for the increased TX values of the plastic, and due to EM and TX resolution differences, a result of the 3D nature of our data. The Spinks study was performed on a 2D scanner, so EM and TX resolution differences were minimal.

The EV density image, as demonstrated through the complications presented by phantom imaging, is sensitive to errors in the TX image. This has implications for clinical implementation of the methodology. In a manner similar to TX spillover from the phantom's plastic walls, spillover from the chest wall could be expected to bias the TX values in human subjects. A possible solution to this issue may be to move the ROIs closer to the left ventricle cavity and away from possible spillover effects, as discussed in Chapter 3.

Another implication to clinical imaging is the lower quality TX images that are often found in larger patients, due to decreased counts resulting from increased attenuation within the patient. These low quality TX images may introduce artifacts into the EV image which could then bias the PV correction (Fig. 5.2 and Fig. 5.3).

Simulations and phantom studies have shown that the EV density image can potentially be used to correct for PV losses. However, various conditions may bias the measured MYO or EV values. In the next chapter, the methodology is adapted to a canine model.

Chapter 6

Dog Model

In-vivo characterization of EV density imaging was performed using a canine model. A canine model was chosen for the following reasons: 1) the ability to use novel tracers such as ^{11}C -carbon monoxide which have not yet been approved for human use in our lab, 2) the ability for repeat imaging since animal studies are not restricted to the dose limits set for normal volunteers, and 3) removal of subject movement during scanning since the dog is anaesthetized. Canine models are typical in cardiac research due to their physiological (i.e. blood flow, metabolism) and anatomical similarity with humans.

6.1 Methodology

6.1.1 Echo

Cardiac wall motion and thickness was assessed using echocardiography to determine the expected PV losses within the various regions of the heart. Echocardiography was performed using a SONOS 5550 (Philips) with a S3 transducer in T-mode (variable frequency output between 1.3 MHz and 3.2 MHz). Short axis and four chamber (equivalent to a HLA slice) images were acquired. Wall thickness and motion were evaluated by an expert in areas corresponding to the 9 segment model used in analysis of the

PET data (see Appendix A). Echocardiogram resolution was approximately 1 mm.

6.1.2 PET Imaging

Repeat imaging ($n=7$) was performed using a 25 kg mixed hound breed dog. The dog was placed in the PET scanner under anaesthetic and ventilated with regular air (10% oxygen). Emission (EM) images were acquired in 3D mode with a $\Delta r/\text{span}$ of 17/7 and rebinned into 2D sinograms using SSRB. Transmission (TX) images were acquired in the default 2D mode with a $\Delta r/\text{span}$ of 4/9. A 2 min pre-injection TX scan was acquired prior to both ^{11}C -carbon monoxide (CO) and FDG imaging.

The heart was centered both axially and vertically within the FOV. For the first five studies, the base of the heart was placed at a distance of ~ 8.5 cm from the axial centre, similar to clinical imaging conditions. For studies 6 and 7, the dog was shifted to align the base of the heart at 4.0 cm and 0 cm, respectively, from the axial centre, in an attempt to change the PV losses around the myocardial wall. PV losses should depend on the location of the heart within the FOV, since the resolution of the scanner is slightly non-uniform.

150 MBq of CO was administered as a bolus inhalation into the ventilator tubing. A 30 s breath hold immediately following inhalation allowed for binding of the CO to hemoglobin. Twelve 5 min frames were acquired after CO administration with summation of frames 4 through 12, representing 45 min, to create the CO blood pool (CO-BP) scan file. A description of CO production is given in Appendix D.

A 150 MBq bolus injection of FDG was administered after the CO count rate had diminished to less than 1% of the initial FDG count rate. The FDG bolus was injected over a period of several seconds. A dynamic FDG acquisition (12x10s, 6x20 s, 6x30 s, 12x300 s frames) was started at the time of injection. The last 6 frames (40 min to 70

min) were summed to form the MYO uptake scan file. The first 4 frames (0 to 40 s) were summed to form a FDG-BP scan file.

In the first study, a bolus glucose loading protocol was administered during FDG imaging [97]. This involved measurement of the dog's blood glucose levels approximately 45 min before FDG injection. A bolus injection of glucose was then given based on the measured blood glucose value. In the next 3 studies, a glucose clamp was applied to improve MYO uptake of the FDG [97]. With the glucose clamp, continuous insulin and glucose IV infusions were administered. The glucose infusion was adjusted to obtain a steady blood glucose level, which was measured every 5 min. The last 3 studies used a modified glucose clamp that included a bolus injection of insulin at the time of FDG injection for further improvement of FDG uptake.

EM images were reconstructed using OSEM (6 iterations and 16 subsets) with a 10 mm Hann filter. TX images used for EV density calculation were reconstructed using OSEM (6i/16s) and a 6 mm Hann filter. The TX image was reconstructed from an attenuation file that had default Gaussian smoothing of 8 mm. By applying a 6 mm Hann filter on top of the default 8 mm smoothing, the TX resolution was matched to the EM resolution. EM and TX transaxial image resolutions were approximately 14 mm.

MYO images were normalized for incomplete FDG uptake (see Appendix C) by first subtracting off the CO-BP image, normalized to the LV value, as given by Eq. 6.1,

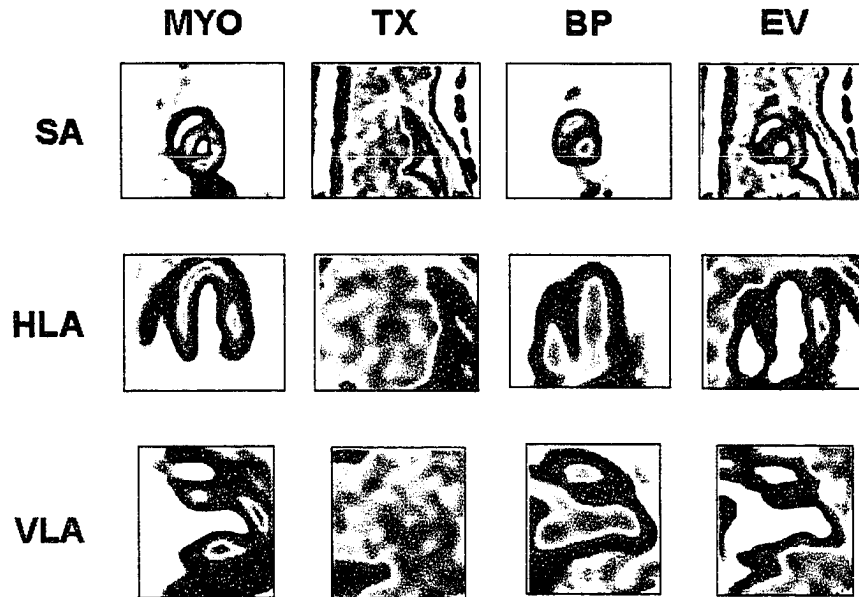
$$MYO_{normalized} = MYO - CO \cdot \frac{MYO_{LV}}{CO_{LV}}, \quad (6.1)$$

where MYO_{LV} and CO_{LV} are the mean values from a region drawn within the LV cavity.

All images were resliced into horizontal long axis (HLA), vertical long axis (VLA), and short axis (SA) slices, defined using the MYO image (see Appendix A). An exam-

ple of the resliced images for study 2 is given in Fig. 6.1.

Figure 6.1: SA, HLA, and VLA slices for study 2.



To evaluate image quality, and to obtain the required normalization factors, three LV and two liver ROIs were defined on a HLA and VLA slice, respectively, of the MYO image. As well, a lung ROI was defined on the TX image. The lung and liver ROIs were used to obtain lung and liver activities from the MYO and BP images, as well as lung density from the TX image. The LV ROIs were transposed onto the TX and CO images to obtain the required normalization factors. The EV density image was obtained according to Eq. 2.1.

To assess EV on a regional basis, the MYO image was sampled into polar map format using 2 mm radius ROIs, centered on the LV myocardium. The MYO polar map values were normalized to set the expected distal-septum values to a RC of 0.55. This value for the RC was based on simulations using the motion model of Chapter 3 with a 9 mm MYO wall, 14 mm smoothing, and a FBV of 0.1. The mean distal-septum value

was chosen as the normalization factor due to its distance from complicating structures such as liver or lung activity (which may effect MYO values in the lateral and inferior walls as described in Chapter 3).

The MYO polar map ROIs were transposed onto the TX, BP and EV images to obtain the corresponding polar maps. A PV-corrected MYO polar map was obtained by division of the MYO and EV polar maps (Eq. 2.3). The polar maps were analyzed using a 9 segment model with the mean and variance determined for each segment. A two-way ANOVA without replication was used to assess the inter-study and inter-segment variation of the segment means. Post-hoc t-testing of mean study and mean segment values versus the global mean was also performed. Adjusted P-values less than 0.05 were considered significant. Both the segment mean and variance were averaged across studies and plotted as a function of segment. The inter-study variance was defined as the variance of the segment means across studies. The intra-segment variance was defined as the mean segment variance averaged across studies.

As has been described earlier, shifting of the ROI towards the LV cavity (endocardial shift) may reduce TX spillover effects. This was studied by producing polar maps with values taken from ROIs shifted 5 mm towards the LV cavity. The data were analyzed as described above.

Finally, a FDG-BP image created from the first 4 frames of a FDG study was investigated as an alternative to CO imaging. FDG-BP, EV, and corresponding corrected MYO polar maps, co-registered with the previous polar maps (ROIs centered on the MYO), were compared with the equivalent CO-based polar maps. The data were analyzed as described above. As well, linear regression analysis was used to determine the correlation between CO- and FDG-BP values, and between FDG- and CO-based EV values.

6.2 Results

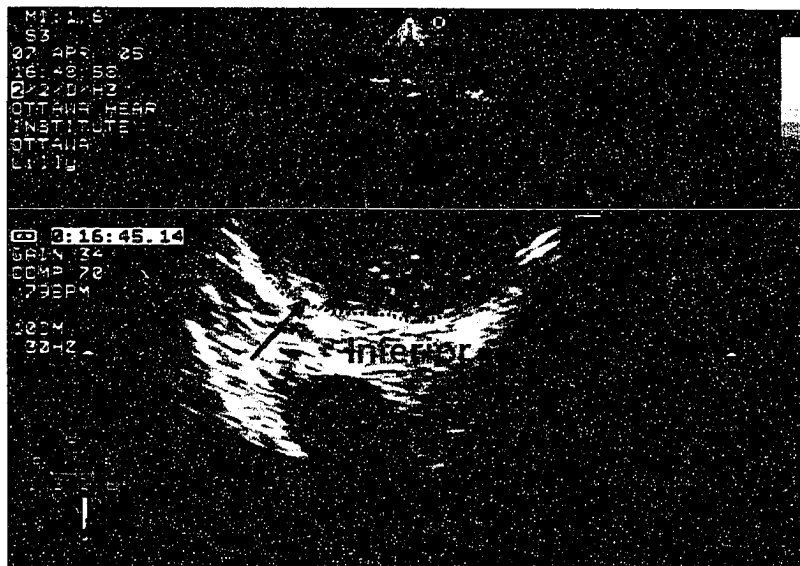
6.2.1 Echo

Fig. 6.2 and Fig. 6.3 show the 4 chamber and short axis views of the dog's heart, obtained from the echocardiogram. The basal-septum and distal-septum regions were determined to have wall thicknesses of 10 mm and 9 mm respectively. The lateral and anterior walls were measured to be 8 mm thick. As expected, the apex was found to be slightly thinner (7 mm) than the other segments. The wall thickness of the basal-inferior region was approximately 9 mm. Lastly, as seen in Fig. 6.3, a region in the distal-inferior region was found to be thinned (6 mm). Visual assessment of wall motion indicated uniform wall thickening during contraction, except in the inferior-distal wall. However, it appeared that the relative wall thickening (relative to wall size) was uniform.

Figure 6.2: Four chamber (HLA) echocardiogram. Wall thickness is greatest in the basal-septum (~10 mm). Apex and lateral wall thicknesses were measured to be 7 mm and 8 mm respectively. Overlaid is a rough outline of the wall edges.



Figure 6.3: Short axis echocardiogram of the distal segments. Wall thickness is fairly consistent (~ 8 mm), except for a region in the inferior segment, which has a thickness of 6 mm (red arrow). Overlaid is a rough outline of the wall edges.



6.2.2 EV Correction

Table 6.1 and Table 6.2 tabulate the lung and liver activities present in the MYO and CO images respectively, expressed as a percent of the target activity. Studies 1 and 4 contained substantial liver, lung, and residual BP activity in the MYO image due to poor FDG uptake. The liver and lung uptake in the CO image was consistent between studies.

Table 6.1: Lung, liver, and residual BP activity in the MYO image (expressed as a percent of the distal-septum MYO activity).

	Study 1	Study 2	Study 3	Study 4	Study 5	Study 6	Study 7
Liver uptake	201	39	53	102	16	30	24
Lung uptake	13	2	6	12	3	3	2.5
residual BP	173	51	58	74	32	27	28

Table 6.2: Lung and liver uptake activity in the CO image (expressed as a percent of the LV activity).

	Study 1	Study 2	Study 3	Study 4	Study 5	Study 6	Study 7
Liver uptake	31	16	20	21	24	25	25
Lung uptake	10	10	9.0	10	8.0	11	9.7

MYO, EV, and corrected MYO polar maps are displayed in Fig. 6.4. The mean MYO value of the 9 segments and 7 studies was measured to be 0.52 ± 0.06 . This corresponded to PV losses of 48%. Two-way ANOVA indicated both variation between segments ($p=0.02$) and variation between studies ($p<0.001$) in the MYO data. Fig. 6.5(A) is a plot of the segmental polar map values for the 7 studies, along with the study mean and standard deviation. No post-hoc differences were found between the study or segment means, versus the global mean. From Fig. 6.5(A), studies 1 and 4 appear to have increased activity in the basal-inferior, distal-inferior, and basal-lateral segments, consistent with increased lung and liver activity (Table 6.1).

Segmental EV polar map values are plotted in Fig. 6.5(B). Two-way ANOVA indicated significant inter-study and inter-segment variation ($p<0.001$). Post-hoc analysis revealed no differences in any of the segments. The BP segment values are plotted in

Figure 6.4: MYO, EV, and corrected MYO polar maps for all 7 studies. EV images were created using the CO image.

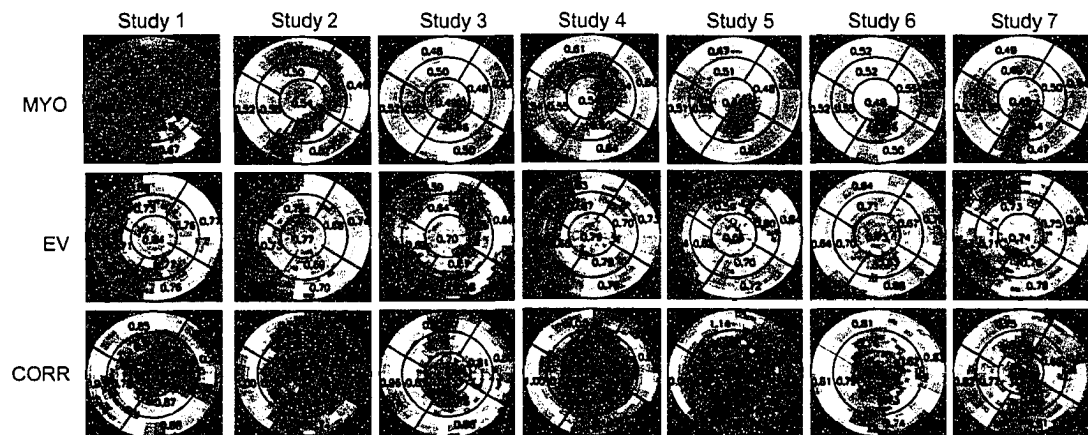
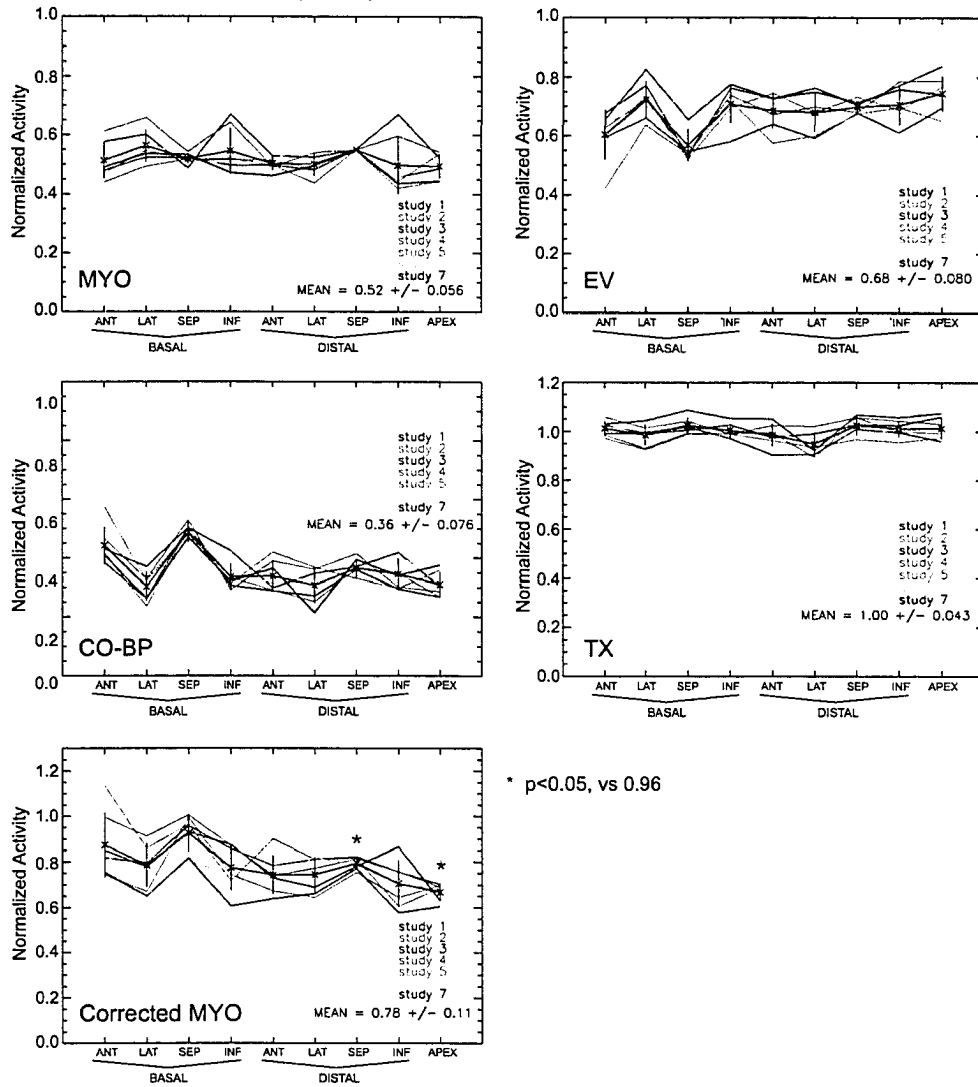


Fig. 6.5(C). ANOVA indicated inter-segment variation ($p < 0.05$), but no inter-study variation ($p = 0.05$). Post-hoc analysis indicated that the basal-septum value tended to be larger than the mean ($p = 0.1$). The pattern of the BP values (Fig. 6.5(C)) is the inverse of what is seen in the EV values (Fig. 6.5(B)). This indicates that it is the BP values that are contributing the PV information. The TX segment values are plotted in Fig. 6.5(D). ANOVA revealed inter-study and inter-segment variation ($p < 0.05$). However, post-hoc analysis indicated no regions or studies different than the mean.

After division of the measured MYO values by the EV values, the mean corrected MYO value was determined to be 0.78 ± 0.11 . Fig. 6.5(E) plots the corrected MYO segment values. As with the uncorrected MYO data, two-way ANOVA indicated significant variation between studies ($p < 0.001$). The variation between regions also increased in significance ($p < 0.001$). Post-hoc analysis revealed that the apex tended to be smaller than the mean ($p = 0.15$). The apex and distal-septum were found to be less than the expected value of 0.96 ($p < 0.05$). Although the distal-septum value was not particularly low compared to other segments, it had a small variance, due to the fact that this region was used to normalize the MYO polar maps for each study.

Two-way ANOVA analysis of the clinically representative studies (excluding studies 1 and 4 due to increased liver and lung activity) removed the inter-study variation ($p = \text{NS}$) but increased the inter-segment variation ($p < 0.001$) in the measured MYO values. The mean MYO value was determined to be 0.50 ± 0.04 . The distal-inferior region tended to be lower than the global mean ($p < 0.08$). MYO, EV, and corrected MYO polar maps, averaged across clinically relevant studies, are given in Fig. 6.6(A). The visual pattern in the MYO polar map followed the pattern expected due to variable PV losses. From the echocardiogram, the distal-inferior wall was seen to be reduced in thickness, so this area was expected to have reduced uptake due to PV averaging. As well, due to the orientation of the dog's heart, the inferior and anterior walls were expected to contain increased axial blurring and, therefore, increased PV losses. Application of the corresponding EV values resulted in a mean corrected MYO value of 0.76

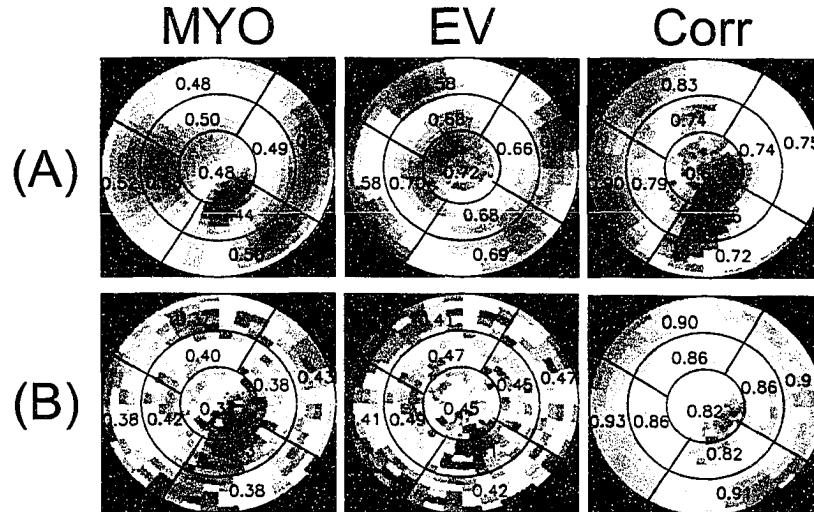
Figure 6.5: Plot of the polar map segment values for the 7 studies. The septal distal region of the MYO data has been normalized to an expected RC of 0.55. Also plotted are the mean study values ($\pm 1\sigma$).



* $p < 0.05$, vs 0.96

± 0.11 . Two-way ANOVA on the corrected MYO values indicated both inter-study and inter-segment variation ($p < 0.001$). However, the inter-segment variation was at a lower significance level than in the uncorrected data. Post-hoc testing indicated no difference in segment or study averages when compared with the global mean. However, values

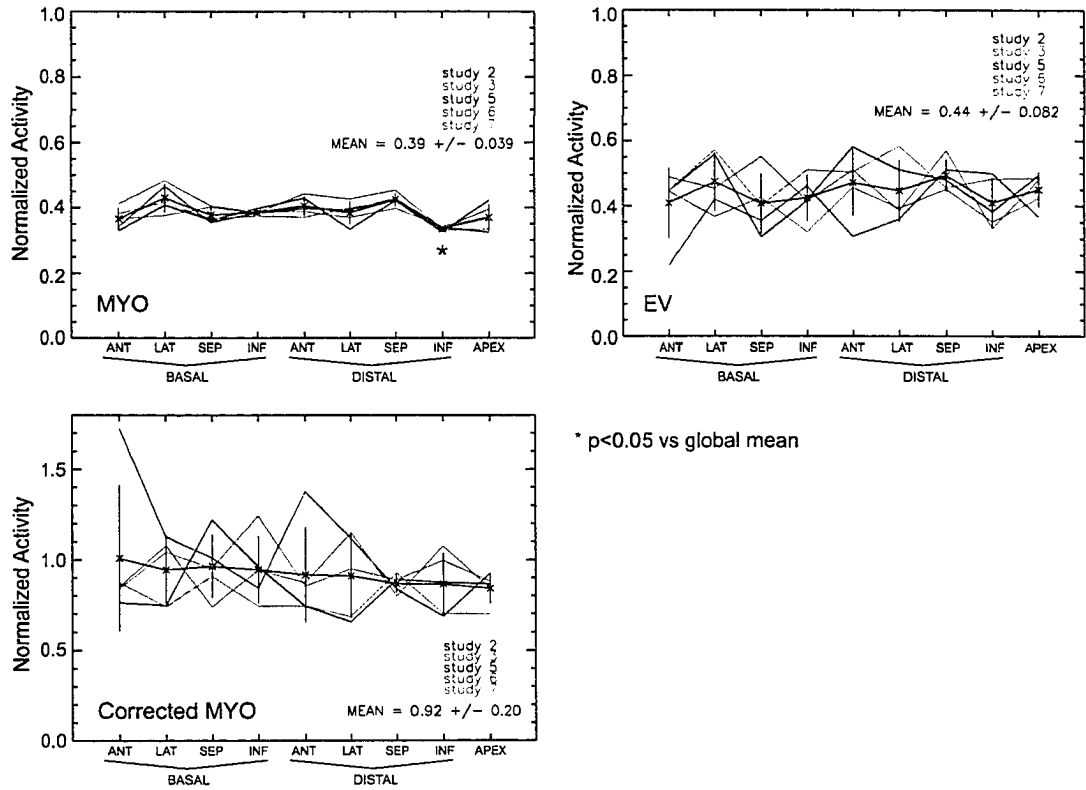
Figure 6.6: MYO, EV, and corrected MYO (CORR) polar maps averaged over the clinically relevant studies using: (A) standard method of ROIs centered on the MYO wall and (B) ROIs shifted 5 mm towards the LV cavity.



lower than the expected value of 0.96 were found in the apex ($p=0.02$), distal-septum ($p=0.03$), and distal-inferior ($p=0.08$) regions. Visual assessment of Fig. 6.6 indicates that the corrected MYO polar map shows increased non-uniformity, when compared with the MYO polar map. This indicates that the EV image was unable to correct for regional PV losses.

Shifting the ROI's 5 mm towards the LV cavity (endocardial shift) on the clinically relevant studies resulted in a mean MYO value of 0.39 ± 0.04 (Fig 6.7(A)). ANOVA indicated both inter-study ($p=0.02$) and inter-segment ($p<0.001$) variation. Post-hoc analysis revealed that the distal-inferior wall was lower than the mean ($p<0.05$). Application of the EV density values (Fig. 6.7(B)) resulted in a mean corrected MYO value of 0.92 ± 0.20 . The corrected MYO data is plotted in Fig. 6.7(C). Two-way ANOVA indicated no inter-segment or inter-study variation. This indicates that, in this case, the EV values were able to account for PV losses. This was confirmed visually in Fig. 6.6. The MYO and EV polar maps followed the same pattern, resulting in a more

Figure 6.7: Plot of the polar map segment values obtained when the polar map ROIs were shifted 5 mm towards the endocardium. Also plotted are the mean study values ($\pm 1\sigma$).



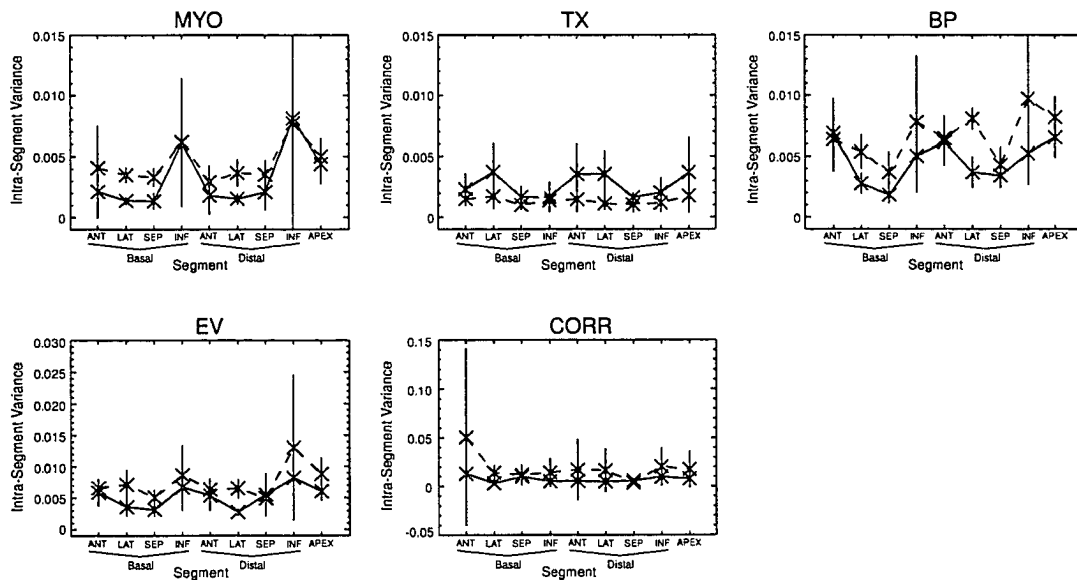
uniform corrected MYO polar map.

The inter-study variance was found to be significantly increased in the BP, EV and corrected MYO polar maps ($p < 0.05$) obtained with a 5 mm endocardial ROI shift when compared with the standard polar map method. No difference was found with the MYO and TX inter-study variances. The inter-study variance of the corrected MYO values was also found to be larger ($p < 0.05$) than that for the measured MYO data.

The intra-segment variances are plotted in Fig. 6.8. A t-test of the means revealed significantly increased intra-segment variance in the MYO, BP, EV and corrected MYO

polar maps obtained with a 5 mm endocardial ROI shift when compared with the standard polar map variances ($p < 0.05$). In the TX polar maps, the intra-segment variance was significantly decreased ($p < 0.05$) with the 5 mm ROI shift.

Figure 6.8: Intra-segment variance (averaged over the clinically relevant studies) for the standard polar maps (solid line) and for those obtained by shifting the ROIs 5 mm towards the LV cavity (dashed line). The variance is increased by shifting the ROIs in all but the TX polar maps.

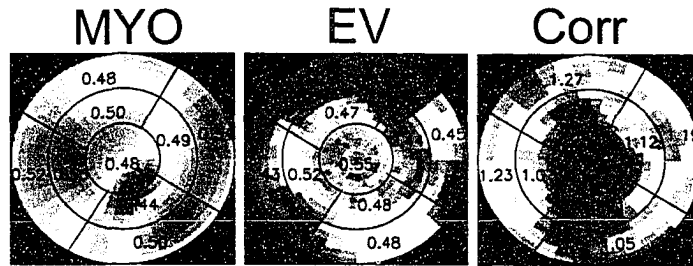


6.2.3 FDG-BP

Mean MYO, EV, and corrected MYO polar maps, obtained using the FDG-BP, are shown in Fig. 6.9. Visual assessment of the average polar maps shows that the EV distribution does not match the MYO distribution, as expected if EV is to correct for PV losses. The result was decreased uniformity of the corrected MYO polar map, compared with the uncorrected polar map.

The corrected MYO values are plotted in Fig. 6.10(A). Application of the FDG-BP

Figure 6.9: MYO, EV, and corrected MYO (CORR) polar maps averaged over the clinically relevant studies. The EV density image was created using the FDG-BP image.



based EV values (obtained using the centered ROI polar maps, plotted in Fig. 6.10(B)) resulted in a mean corrected MYO value of 1.24 ± 0.65 . This corresponded to a 27% overestimation of the true activity, versus the 21% underestimation obtained with the CO-BP image. This was a result of larger BP values. ANOVA indicated significant inter-study variation ($p < 0.001$), but no inter-segment variation ($p = 0.11$) in the corrected MYO data. From post-hoc analysis, the apex was found to have the lowest value ($p = 0.12$ vs the mean).

The polar map segment values from the FDG-BP images are plotted in Fig. 6.10(C). ANOVA indicated significant inter-segment and inter-study variation ($p < 0.001$). The CO-BP polar maps exhibited only inter-segment variation.

Figure 6.10: Plot of the polar map segment values obtained using a FDG-BP image. Also plotted are the mean study values ($\pm 1\sigma$).

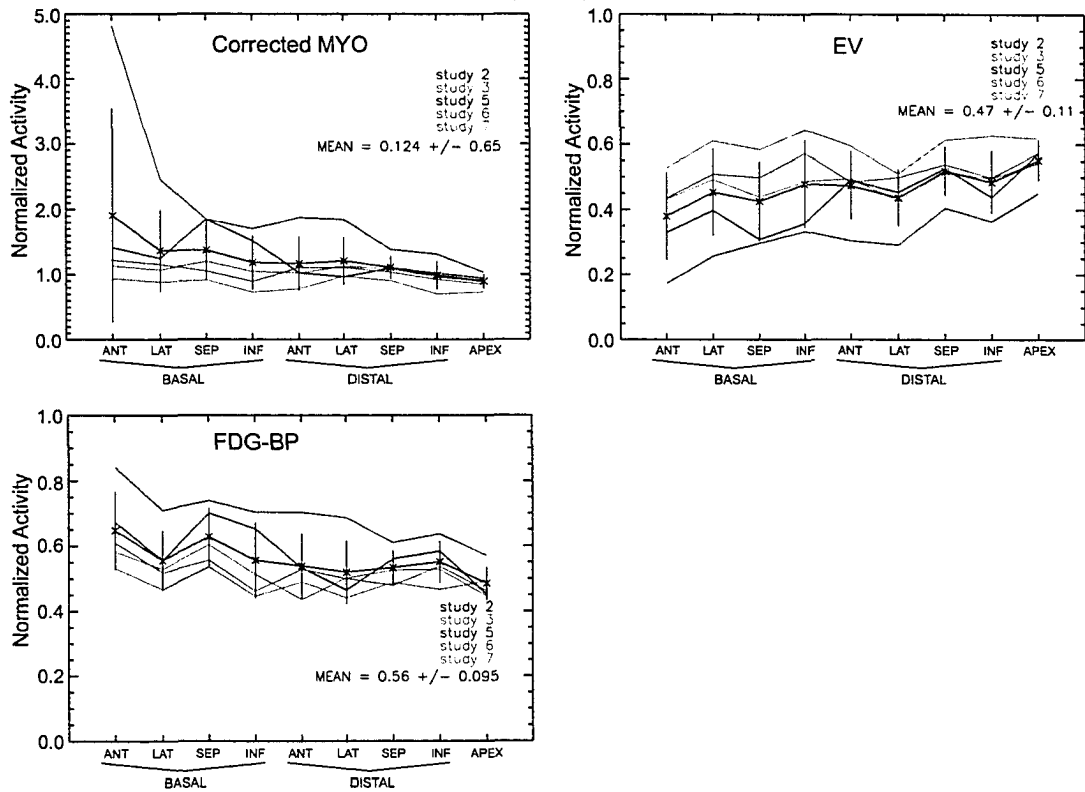
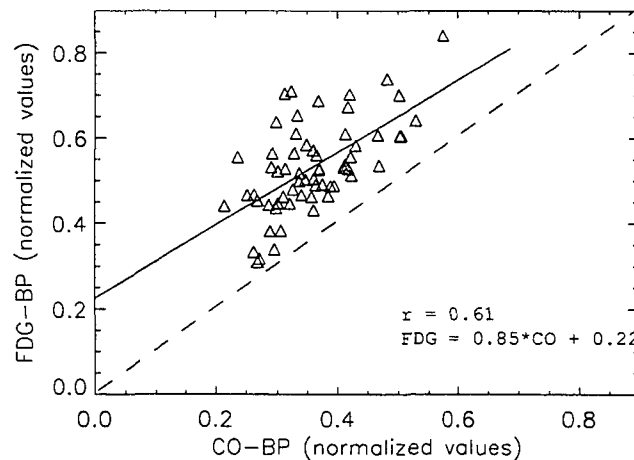


Figure 6.11: Scatter plot of the FDG-BP values for all segments and studies, versus the CO-BP values.



The FDG-BP values were found to be on average 47% higher than the CO-BP values. A paired student t-test on the segment means indicated significant differences between the CO- and FDG-BP values ($p < 0.001$).

Fig. 6.11 is a scatter plot of the FDG-BP versus CO values. Linear regression analysis of the scatter plot indicated the FDG-BP values were correlated with the CO values ($r = 0.61$). The FDG-BP based EV values were found to be correlated ($r = 0.74$) with the CO-BP based EV values, as shown in Fig. 6.12.

The inter-study variance of the FDG-BP values was significantly higher than the CO inter-study variance ($p < 0.001$), indicating that the method has less reproducibility. However, the intra-segment variance was not statistically different between the two methods. The intra-segment variance is plotted in Fig. 6.13. The variance in corrected MYO values within the basal-anterior wall is skewed due to noise. In this region, the EV polar map of study 5 contained pixels that were near or less than zero (see Fig. 6.14), due to high BP values. This resulted in severely biased corrected MYO values and large variance estimates. The inter-study variance of the corrected MYO values tended to be larger than the measured MYO values ($p = 0.08$).

Figure 6.12: Scatter plot of the FDG-BP based EV values for all segments and studies, versus the CO based EV values.

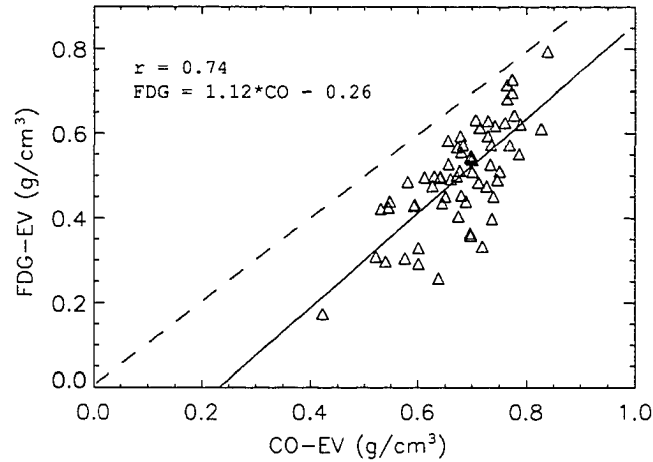


Figure 6.13: Intra-segment variance (averaged over the clinically relevant studies) for the FDG-BP based polar maps. The variance in the basal-anterior wall is skewed due to noise in study 5 resulting in several pixels where $EV \approx 0$ or $EV < 0$.

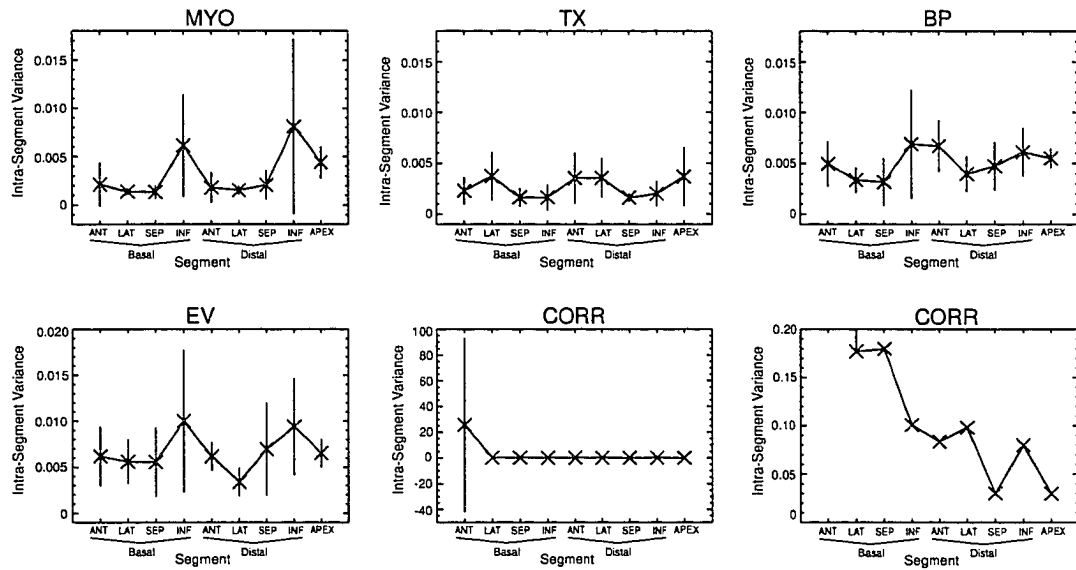
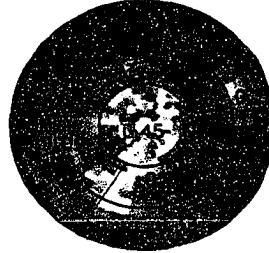


Figure 6.14: FDG-based EV polar map for study 5. Some pixels in the basal-anterior region are ~ 0 or < 0 (red arrows). This is due to ill-conditioned BP values that are either equal to or exceed the corresponding TX values.



6.3 Discussion

6.3.1 EV Correction

High FDG uptake in the lung and liver biased the measured MYO values in the lateral and inferior segments as seen in studies 1 and 4. These biased MYO values tended to obscure the inter-segment variation expected due to PV effects, and to introduce inter-study variation. Clinically, these two studies are of poor quality, and may have been repeated. Studies 1 and 4 were removed from further analysis so that EV density imaging could be best characterized.

Analysis of the clinically representative images (studies 2, 3, 5, 6, and 7) showed that application of the EV density correction was able to provide more quantitatively accurate MYO measurements. In polar maps with ROIs centered on the MYO wall, MYO values were initially underestimated by 50%. After PV correction, the MYO estimates were underestimated by 22%.

However, noise in the EV image resulted in increased noise in the corrected MYO values, as seen in the increased inter-study variance in corrected MYO values. Much of this noise was introduced by the BP image. From Fig. 6.5(C), it is seen that the BP values are relatively consistent in the basal-septum. The reason for this is that the septum ROIs on the BP image were placed in a local minimum. This local minimum

was a result of spillover from both the LV and RV cavities. As a result, the values here were relatively insensitive to small changes in ROI position. The ROIs for the other segments were placed along the edge of the BP image and were more sensitive to small changes in their position, resulting in noisy BP polar maps. The TX values did not show the same amount of noise as the BP values due to increased TX spillover from pericardial structures.

The corrected MYO activity was found to be underestimated in the apex and distal-inferior segments due to increased TX values within this region. This overestimation of TX values was a result of TX spillover from either the chest wall or liver, as predicted by the simulations in Chapter 3. The simulations predicted that, due to PV losses across the epicardium, the normalized TX values within most segments should be ~ 0.9 . However, from Fig. 6.5(D), the TX values are unity for the distal-inferior and apex regions. This TX spillover may be the reason that the corrected MYO values remained underestimated by 22%. From Fig. 6.5(E), only the corrected MYO value in the basal-septum was within 10% of the expected value of 0.96. In this region, TX spillover is compensated for by RV spillover.

The corrected MYO value in the basal-anterior segment of study 5 appeared to be overestimated. This was a result of increased BP values within this region (Fig. 6.5(C)), believed to be due to increased LA activity. The reason for this increased LA activity is unknown, but could be related to attenuation correction since it was also seen in the FDG-BP image.

Shifting the ROIs 5 mm towards the LV cavity placed the ROIs near the inside edge of the MYO wall. In this region, the MYO values were underestimated by 61% on average. Application of the corresponding EV values recovered the expected activity to within 5% (Fig. 6.7). As well, the EV values removed the inter-segment and inter-study variation, including the basal-septum and apex. This resulted in a more uniform distribution, as desired (Fig. 6.6). The reason for the improvement in EV estimates

was due to the fact that TX spillover effects are minimized near the endocardium, as predicted in Fig 3.11 of Chapter 3.

However, the disadvantage to an endocardial shifting of the ROIs was an increase in inter-study variance. This was due to the increased PV losses incurred. As a result, a larger correction ($1/EV$) was needed, leading to small EV values. Since the EV values are applied as a divisive factor, the corrected MYO values are more sensitive to changes in EV when EV is small. A similar problem was reported by Hutchins et. al [74] using a kinetic model-based PV correction.

To allow for the comparison of the 7 studies, the MYO data were normalized to set the distal-septum value to an expected RC value of 0.55. This value of RC was based on simulations of a 9 mm MYO wall, 14.4 mm smoothing, and a FBV=0.1. The true RC value obtained from this simulation was 0.530. Using this value of 0.530 would have resulted in a 4% increase in the reported corrected MYO values. The data obtained using the 5 mm endocardial shifted ROIs would then have recovered the true activity to within 1%. However, changing the wall thickness to 10 mm in the simulation would result in a RC of 0.573, or a 4% decrease in the corrected MYO data. As well, changes to the FBV would also effect the RC value. For a 9 mm MYO wall and with a FBV of 0, a RC of 0.589 is obtained. Use of this value would result in a 7% increase in the corrected values. In humans, FBV has been reported to be 0.1 [2]. It was assumed that 0.1 would be a reasonable approximation for the dog as well, since the dog's heart is similar to that of a human. However, this value is only an approximation and cannot be easily determined. Given the errors involved in calculating an appropriate RC value, 0.55 was determined to be a reasonable approximation.

The EV values obtained are in good agreement with the published human values. Yamamoto [3], Iida [2], and Gerber [4] found the EV value to be approximately 0.63 g/cm^3 . This is consistent with the dog EV values, obtained with polar map ROIs centered on the MYO wall. However, none of the previous studies reported the value

within the apex, which was found to be larger in this study. The previous studies typically used manually positioned ROIs on a transaxial slice, whereas in this research, ROI placement was automated and sampled the entire LV myocardial wall (i.e. polar maps). This is an important step if the EV values are to be used regionally. As well, it allows for PV correction of the polar maps used by experts in interpreting areas of disease.

Although the EV values are comparable to the published human studies, they are larger than the published dog results of Iida [5]. One of the reasons for this may be the size of the dog. In the Iida paper, the dog weight varied between 10 kg to 20 kg. The dog used in our investigation was larger (25 kg), with a heart more similar in size to that of a human (confirmed with the echocardiograms).

It appears that if the polar maps are carefully sampled to avoid contaminating TX signal, then the EV values, obtained using the CO-BP, can provide more uniform polar maps (see Fig. 6.6) and more accurate activity measurements. This may improve the clinical interpretation of the MYO polar maps. The MYO and EV polar maps of Fig. 6.6 were averaged over 5 studies. The corrected MYO polar maps were then obtained by dividing the averaged polar maps, reducing the effects of noisy EV pixels. However, the individual polar maps would be expected to contain more noise (i.e. Fig. 6.5), which can potentially be reduced via polar map smoothing.

6.3.2 FDG-BP

The FDG-BP values were found to be correlated with the CO-BP values, but systematically larger. This was a result of myocardial FDG uptake within the first 40 s, which biased the BP image in a manner similar to the effect of lung or liver activity on the MYO image. The intercept of Fig. 6.11 was also found to be non-zero. This implies that in regions where the CO-BP goes to zero, the FDG-BP does not. This is an expected result if myocardial FDG uptake is biasing the FDG-BP image. Application of the biased FDG-based EV values resulted in a 26% overestimation of the true

activity, which is still an improvement over the initial 50% underestimation of activity. However, the polar map uniformity was not improved (see Fig. 6.9). Summing fewer frames may provide a more accurate assessment of the vascular space using FDG-BP, but at the expense of increased noise.

A larger correlation was found between the FDG- and CO-based EV values. This is due to the fact that the EV values also include TX information, which is independent of the method used to obtain the BP image. This correlation would be expected to decrease if the polar map ROIs were endocardially shifted by 5 mm.

The EV values obtained using the FDG-BP image are smaller than the value of 0.60 g/cm^3 published by Gerber et. al. [4]. Gerber reported no difference between FDG-based and CO-based EV values in healthy subjects. As well, the FDG-based EV values from a set of coronary patients were not found to be different than the values from the healthy subjects. However, in the discussion, Gerber reported that a FDG-BP has a larger volume of distribution than a CO-BP (and hence larger values in the myocardial wall). This is given as the reason that their EV values in coronary patients are smaller than what was reported by Yamamoto [3] and de Silva [8]. Unfortunately, no comparison was made between CO-BP and FDG-BP values. As discussed above, the FDG- and CO-based EV values are better correlated than FDG- and CO-BP values, due to the inclusion of TX information in the EV values. It may be that the larger regions used by Gerber included more TX information, minimizing the effects of myocardial FDG uptake in the BP image. Gerber's was also the only study to find lower EV values in the septum, compared with the anterior and lateral walls. This is consistent with TX spillover overestimating the anterior and lateral wall EV values, suggesting that the regions used by Gerber did indeed contain significant TX effects.

In some instances, the methodology was found to produce non-physical results due to increased BP values and noise. With these two conditions, it may be possible for $BP \approx TX$, or even $BP > TX$. This would result in ill-conditioned EV values, where $EV \approx 0$

or $EV < 0$, as seen in the basal-anterior segment of the FDG-based EV polar for study 5 (Fig. 6.14). Use of these ill-conditioned EV values provides non-physical activity estimates. Smoothing of the EV or corrected MYO polar maps, to remove excessive noise, may provide better estimates in situations where the method becomes ill-conditioned.

Due to contaminating MYO signal in the BP image and increased noise, the use of summed FDG - BP images in EV imaging may not prove useful in improving the clinical interpretation of polar maps. However, the FDG -based EV values can improve the quantitative accuracy of activity estimates. Larger regions may help in reducing noise artifacts.

Chapter 7

Human Studies

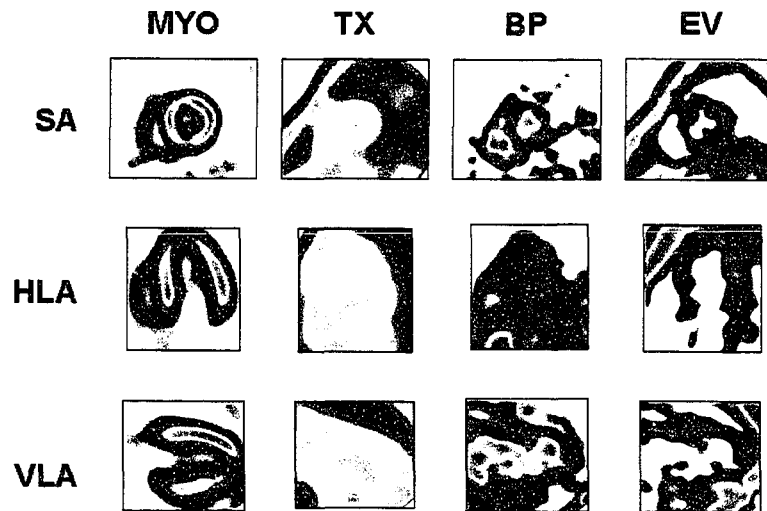
The method outlined in Chapter 6 was adapted to a set of normal human subjects to determine the feasibility of clinical EV density imaging for PV correction. No CO image was acquired, and so the BP image was created only from the first 40 s of the dynamic FDG dataset.

7.1 Methods

FDG imaging was performed on 5 normal subjects (3 males, 2 females) having a mean age of 28.2 ± 6.7 years. Each subject was injected (30s to 60 s manual infusion) with approximately 75 MBq of FDG . A dynamic FDG dataset (12x10 s, 6x20 s, 6x60 s, 12x300 s) was acquired using the default 2D mode ($\Delta r/\text{span}$ of 17/35). Prior to FDG injection, a 6.5 min transmission scan ($\Delta r/\text{span}$ of 4/9) was acquired. A glucose clamp [97] was administered to all of the patients during FDG imaging.

The BP scan file was created through summation of the first 4 useful frames of the dynamic dataset (40 s). A useful frame was defined as one which contained both RV and LV activity (typically, the first frame contained RV activity only). The MYO scan file was created by summing the last 6 frames (30 min).

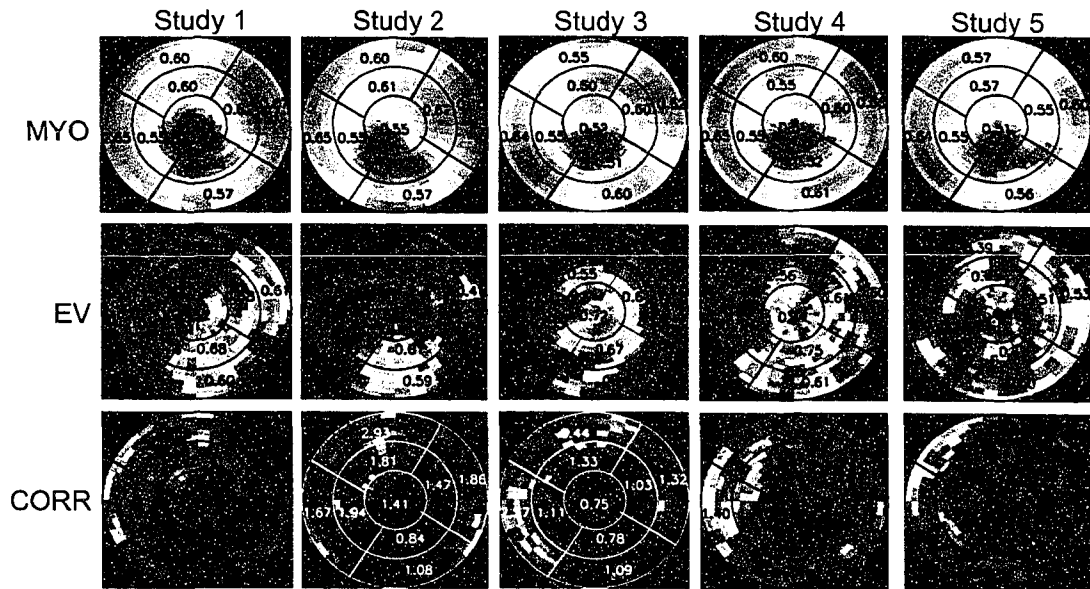
Figure 7.1: SA, HLA, and VLA slices for study 1.



EM images were reconstructed using OSEM (6 iterations and 16 subsets) with a 12 mm Hann filter. TX images used for EV density calculation were reconstructed using OSEM (6i/16s) and a 8.9 mm Hann filter. The TX image was reconstructed from an attenuation file that had default Gaussian smoothing of 8 mm. By applying a 8.9 mm Hann filter on top of the default 8 mm smoothing, the TX resolution was matched to the EM resolution. EM and TX transaxial image resolutions were approximately 15.5 mm.

The images were analyzed in the same manner as was used for the canine model (see section 6.1.2). Briefly, the images were resampled into SA, HLA, and VLA slices. An example of the resliced images from study 1 is given in Fig. 7.1. Three LV ROIs were defined on the MYO image. One lung ROI was defined on the TX image. The EV image was created according to Eq. 2.1. All images were sampled into polar map format (using 2 mm ROIs, centered in MYO wall) and analyzed using the 9-segment model. The MYO values were normalized by setting the distal-septum region to a RC

Figure 7.2: MYO, EV, and corrected MYO (CORR) polar maps for all 5 subjects. EV images were created using the first 4 frames of the dynamic FDG dataset.



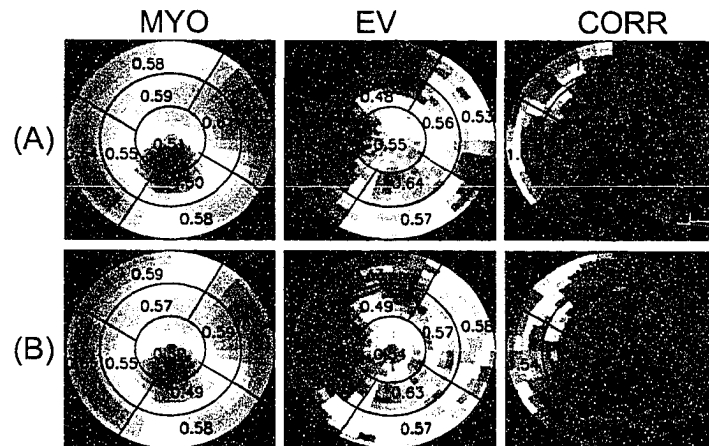
of 0.55. This value for the RC was based on simulations using the motion model of Chapter 3 with a 10 mm MYO wall, 15.5 mm smoothing, and a FBV of 0.1.

7.2 Results

Liver and lung activity in the MYO image was found to be $<5\%$ of the MYO activity for all subjects, which is better than in the dog studies. The mean residual LV activity in the MYO image was measured to be $21 \pm 8.6\%$. The mean lung activity in the FDG-BP images was found to be $20.5 \pm 4.8\%$, which is slightly higher than the dog studies. Clinically, these values represent good image quality.

The MYO, EV, and corrected MYO polar maps are shown in Fig. 7.2. The polar maps, averaged across studies, are shown in Fig. 7.3. The pattern seen in the MYO polar map is consistent with expected PV losses. As was the case with the dog studies (Fig. 6.6), the inferior and anterior regions were aligned along the axial dimension of

Figure 7.3: Mean MYO, EV, and corrected MYO (CORR) polar maps averaged: (A) across all 5 studies and (B) only over studies 1, 4, and 5, since studies 2 and 3 were believed to have contained patient movement that biased the EV values, as discussed later in the chapter.



the scanner, where PV losses are increased due to axial blurring. This is consistent with the MYO polar maps of Fig. 7.3, which have lower values in the inferior and anterior regions, compared with the septum and lateral wall. The distal-inferior/apex region is also seen to have decreased uptake. This region of the myocardial wall is typically thinner, and so it experiences increased PV losses. The EV polar map should have the same distribution as the MYO polar map. However, from Fig. 7.3, it is seen that the EV polar map does not follow the expected distribution. In particular, the apex and inferior segments have increased EV values, whereas these regions corresponded to low MYO values. The result was that application of the EV values did not result in a more uniform MYO polar map.

The mean MYO value was measured to be 0.58 ± 0.06 (a 42% underestimation of the true activity). The MYO segment values are plotted in Fig. 7.4(A). ANOVA on the measured MYO data indicated inter-study ($p=0.02$) and inter-segment ($p<0.001$) variation. Post-hoc analysis indicated the the distal-inferior segment was lower than the mean ($p<0.05$), while the basal-septum was larger than the mean ($p<0.01$).

The mean EV value was determined to be 0.50 ± 0.12 . ANOVA indicated significant inter-study and inter-segment variation ($p < 0.001$), but no differences were found with post-hoc analysis. The EV values are plotted in Fig. 7.4(B). The BP, and TX values are plotted in Fig. 7.4(C) and Fig. 7.4(D) respectively. ANOVA on the TX data revealed both inter-study ($p = 0.02$) and inter-segment ($p < 0.01$) variation. Values tended to be less than 1.0 in the distal-lateral ($p = 0.08$) and basal-lateral ($p = 0.09$) regions, next to the lung. ANOVA on the BP data indicated inter-segment variation ($p < 0.001$), but no inter-study variation ($p = 0.09$). The basal-septum tended to be larger than the mean ($p = 0.15$). These results are comparable to those found in the dog study.

The corrected MYO data is plotted in Fig. 7.4(E). The mean value was found to be 1.28 ± 0.47 . This represented a 30% overestimation of the expected activity of 0.96. ANOVA indicated reduced inter-segment variation ($p < 0.01$), but increased inter-study variation ($p < 0.01$), when compared with the uncorrected results. Post-hoc analysis revealed no differences between segment values and the mean. However, from Fig. 7.3, a couple of patterns are distinguishable. First, the largest values occur along the basal-septum and basal-anterior wall, due to RV spillover. Secondly, the distal-inferior/apex region is still the lowest region. As was the case with the dog study, TX spillover from the chest wall may have overestimated the EV values here. The distal-inferior/apex region values are close to the expected activity of 0.96, indicating that the increased TX spillover is compensated for by the increased BP values obtained using the FDG-BP. A similar effect was discussed in Chapter 3 in regards to lung density and activity. Since the amount of BP overestimation and TX spillover are not accurately known, it is best to remove these two effects.

Figure 7.4: Plot of the polar map segment values for the 5 studies. The septum of the MYO data has been normalized to an expected RC of 0.55. Also plotted are the mean study values ($\pm 1\sigma$).

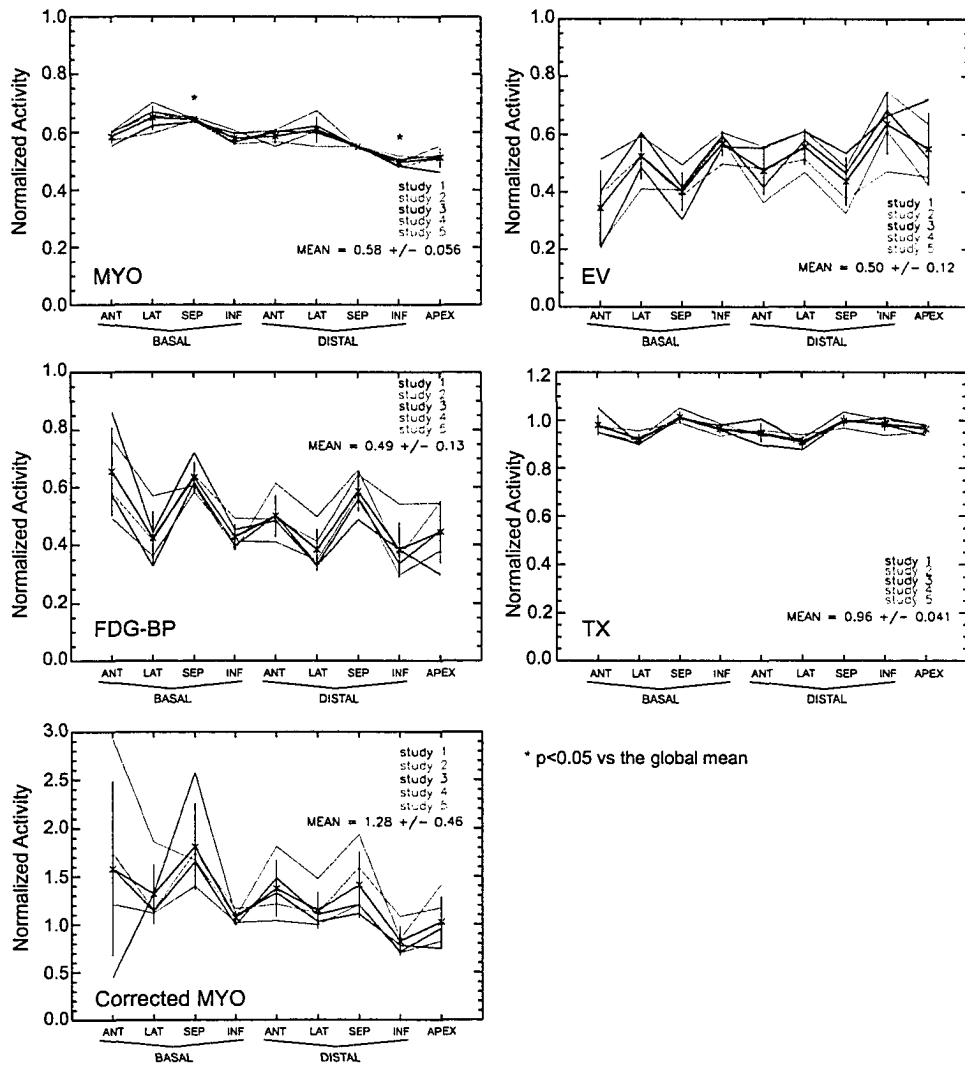
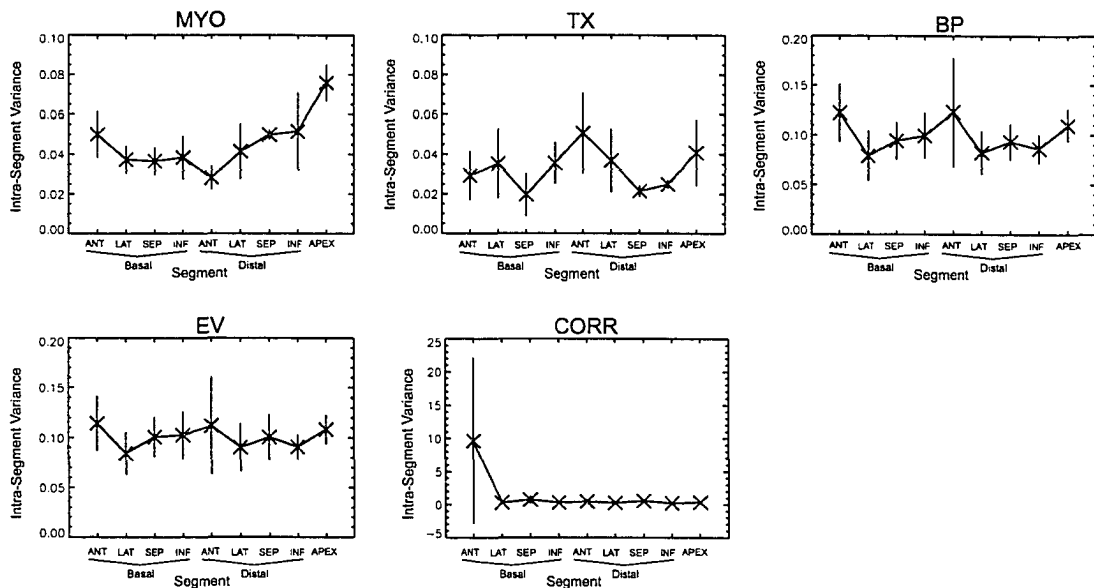


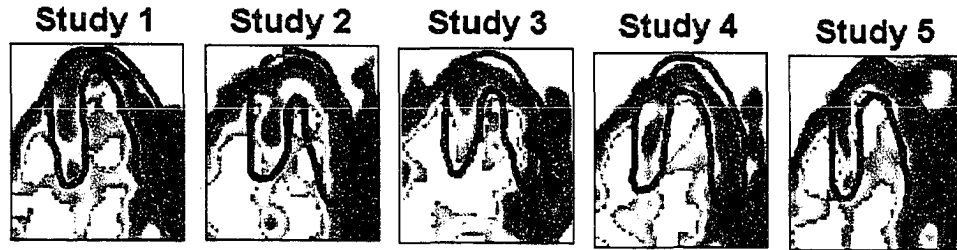
Figure 7.5: Intra-segment variance, averaged over the subjects.



The intra-segment variances are plotted in Fig. 7.5. The corrected MYO intra-segment variance tended to be larger than the measured MYO intra-segment variance ($p=0.11$). This indicated an increase in noise in the polar maps. The intra-segment variance of the basal-anterior wall of the corrected MYO was found to be excessively large, due to ill-conditioned EV values in studies 2 and 3 (see Fig. 7.2, as described in the last chapter (see Section 6.3.2)). The inter-study variance of the corrected MYO data was also found to be significantly larger than compared with the measured MYO values ($p<0.05$), indicating poor reproducibility, as found with the FDG-BP dog studies.

Fig. 7.6 is an image of the BP HLA slices for each subject. Overlaid on each is an outline of the MYO wall, obtained directly from the MYO images. In studies 2 and 3, the BP image does not seem to match the MYO wall. This indicates substantial patient movement occurred between BP and MYO imaging, which may bias the EV values. Using only studies 1, 4, and 5, the mean MYO value was determined to be 0.57 ± 0.06 . ANOVA indicated significant inter-segment variation ($p<0.001$), but no inter-study variation. Post-hoc analysis revealed that the distal-inferior wall tended to

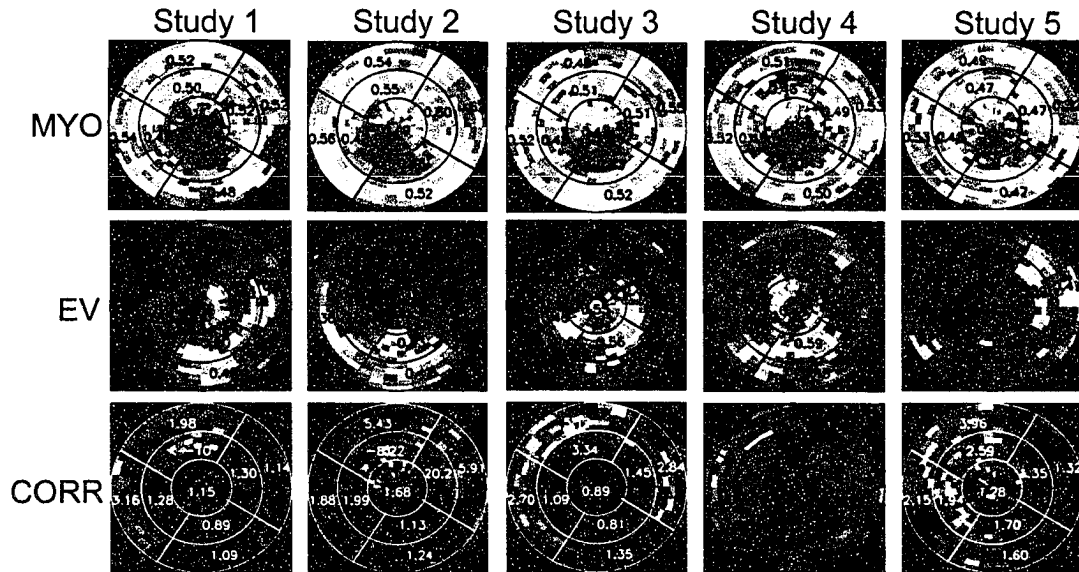
Figure 7.6: HLA slices of the BP image for each subject. Values larger than the LV mean are set to white. Overlaid on each image is an outline of the corresponding MYO wall. The endocardial edge of the lateral wall in studies 2 and 3 appears to be mismatched in the MYO and BP images. This indicates possible patient movement during scanning. Also apparent is the increased LA, RA, and RV values, relative to the LV value.



be lower than the mean ($p=0.08$), while the basal-septum was larger than the mean ($p=0.01$). After application of the EV density values, the mean corrected MYO value was found to be 1.20 ± 0.28 , a 25% overestimation. ANOVA still indicated both inter-segment and inter-study variation ($p<0.001$). Post-hoc analysis revealed no difference between the segment and global means. Visual assessment of Fig. 7.3 showed that the polar map uniformity was increased in the corrected polar map when compared with the map that included all the studies. However, the distribution was still less uniform than the uncorrected polar map.

In the dog studies, a 5 mm endocardial shift of the polar map ROIs resulted in more accurate EV estimates. Fig. 7.7 shows the MYO and EV polar maps for the normal subjects, obtained using a 5 mm endocardial ROI shift. The mean MYO value for studies 1, 4, and 5 was found to be 0.48 ± 0.04 . ANOVA indicated significant inter-segment variation ($p<0.001$), but no inter-study variation. Post-hoc analysis revealed that the apex tended to be lower than the mean ($p=0.06$) while the basal-lateral wall was larger than the mean ($p=0.03$). The mean corrected MYO value was determined to be 0.96 ± 3.2 . Although this value is accurate (true expected value of 0.96), the error is also large ($\sim 300\%$). Visual assessment of Fig. 7.7 showed that the EV images, with the exception of study 4, all contained ill-conditioned values (~ 0 or <0). This is due

Figure 7.7: MYO, EV, and corrected MYO (CORR) polar maps for all 5 subjects obtained using ROIs with a 5 mm endocardial shift. Pixels less than 0 have been set to black. In all except study 4, this resulted in ill-condition EV values (~ 0 or < 0) in the septum and anterior wall.



to increased RV/RA/LA activity, relative to the LV, as seen in Fig. 7.6. Only study 4 appears to have equal activity in all chambers (and no motion). Increased LA activity was seen to produce ill-conditioned EV values in dog study 5.

7.3 Discussion

Use of the FDG-based EV values resulted in a 30% overestimation of the true activity (25% overestimation for subjects with no appreciable motion artifacts). These results are consistent with the 27% overestimation found in the canine mode when FDG-based EV values were used. As before, this overestimation of BP values was believed to have resulted from contaminating MYO signal due to early FDG uptake in the myocardium. As well, substantial inter-study variation in the corrected MYO value of the basal-anterior wall was found. This was a result of ill-conditioned EV values ($EV \approx 0$ or < 0) in studies 2 and 3 (see Fig. 7.2), believed to have been due to motion.

In the dog model, the polar map ROIs were shifted 5 mm towards the LV cavity to obtain more accurate EV estimates. A similar approach was performed with the normal subject data. However, the result was a rise in the number of ill-conditioned EV pixels (see Fig. 7.7). The dog studies, with the exception of study 5, did not exhibit the same problem.

The ill-conditioned EV values were believed to be a result of BP values overestimated due to increased RV/RA/LA activity, relative to the LV activity. This was not found to be as much of a problem in the dog studies. The reason for this is that the normals were injected over a longer period. In the dog studies, the FDG was administered as a quick bolus injection, and so the FDG entered the RV/RA cavities at the same point in time. This frame, which contained a hot RV/RA, was removed from the FDG-BP summation. However, since the patients were injected over a longer period of time, high concentrations of FDG were continually entering the RV/RA cavities over the summed frames. Only later frames, after the FDG infusion finished, would consist of equal LV/RV activities. However, these frames would also have substantial myocardial FDG uptake.

Another reason for the ill-conditioned EV values may be the increased noise in the FDG-BP images of the normal subjects, compared with the dog images. There are several reasons for this increase in noise. First, the injected activity of the normal subjects was $\sim 50\%$ of that used for the dog studies. Current clinical FDG imaging doses are larger (~ 200 MBq) than those used for the dog studies. However, at the time the normal subjects were imaged, FDG was received from off-site, limiting the amount of activity available for injection. Secondly, due to the increased subject size (relative to the dog) attenuation and scatter were increased, resulting in poorer image quality.

Lastly, the ill-conditioned EV values in studies 2 and 3 were thought to be also related to patient motion. Since the dog was under anaesthetic, there was no movement

between BP and MYO imaging. However, the patients are scanned fully-awake, and are prone to small movements over the length of the scan (~ 70 min). Large movements, on the order of 1 cm or more, are often caught since the patients are marked and aligned with the lasers in the PET scanner. In these instances, the scan is repeated. However, smaller movements can go unnoticed. This appears to be the case in studies 2 and 3 (Fig. 7.6).

The FDG-based EV values obtained with the normal subjects are comparable to the FDG-based EV values obtained in the dog study (Chapter 6). Early myocardial FDG uptake appears to overestimate the BP values and underestimate the EV values. This is contrary to the findings of Gerber et. al. [4], who found no difference between FDG-based and CO-based EV values. This difference is believed to be a result of the larger ROIs used by Gerber, as is discussed in Section 6.3.2.

The FDG-based EV values were found to improve the quantitative accuracy of the activity measurements, but at the expense of increased noise. A similar result was reported in the dog study. Larger regions may help in reducing noise artifacts. However, as seen in Fig. 7.2, the use of FDG-based EV images does not improve polar map uniformity. As such, it may not prove useful in improving the clinical interpretation of polar maps for human subjects. A similar finding was reported in the FDG-based EV method of the dog study. However, accurate EV values were obtained using the high quality CO-BP image. It stands to reason then that the method would also work for humans if a better BP image could be obtained. Clinical use of CO imaging is a possibility, but not desirable due to the increased radiation burden to the patient. As well, acquisition of a CO image increases the scan time, which is currently ~ 80 min for a dynamic FDG study.

Another possibility is the use of factor analysis to extract a good quality BP image from the FDG dataset [93, 94, 98]. Briefly, the signal in each pixel, as a function of time, can be represented as a linear summation of the various time activity curves for

each region (such as MYO, LV, RV, liver, etc.), multiplied by the appropriate weighting factors. These time activity curves can be regarded as the basis for the image space. Factor analysis projects the pixels onto each basis to determine the weighting factors which are then used to form the factor image. A BP image formed in this way could be similar to the CO image, free from contaminating MYO signal.

The results obtained from the set of normal human subjects indicates that, with the use of a high quality blood pool image, EV density imaging has the potential to improve FDG viability imaging.

Chapter 8

Discussion

Use of the EV density image to correct for PV losses has several potential advantages over other methods. First, if the FDG-BP image is used, then the EV image can be created from the data currently acquired during clinical imaging. There is no need for subsequent CT or MRI scans. Secondly, the EV values are independent of the parameters in a kinetic model. RC values obtained as a parameter in a kinetic model can be correlated with the other parameters [74], which can result in increased or decreased PV estimates that do not reflect true increased or decreased PV losses. Lastly, the method is computationally simple.

Previous papers had reported that EV values within the apex may be biased due to TX spillover from the surrounding organs (i.e. chest wall or liver), but never quantified this effect [9, 75]. In fact, the apex was typically not included in previous analysis. Characterization of TX spillover effects is needed if the methodology is to be applied to the entire LV myocardium.

In this research, the effect of TX spillover from adjacent organs was investigated. In the simulation and phantom studies of Chapter 3, Chapter 4, and Chapter 5, the overestimation of EV values due to TX spillover was quantified. In-vivo, EV values taken at the centre of the MYO wall were confirmed to be overestimated in all regions except the

septum, due to TX spillover. In the septum, the TX spillover is exactly compensated for by RV blood spillover. Shifting the ROIs 5 mm towards the LV cavity, and away from TX spillover, provided accurate EV values for regional PV correction in the dog studies. By shifting the ROIs, more uniform MYO polar maps were obtained (see Fig. 6.6). This is consistent with the findings of Hutchins et. al. [74], who found biased RC estimates near the epicardium using a kinetic model-based correction. Similar to the Hutchins model, the EV model also assumes that the signal (activity or tissue density) within a pixel is comprised of only BP and MYO signal.

The simulations also predicted decreased EV estimates due to increased RV, RA, or LA activities (relative to the LV activity). Increased LA activity was believed to have underestimated EV values within the basal-anterior wall of dog study 5. An area of research that may hold potential is the use of the initial FDG frame, which typically contains only RV/RA activity, as a means of setting the LV and RV activities equal. This is analogous to the subtraction of residual BP activity in the MYO images performed for the dog studies. The effect of MYO signal in the BP image was also found to be problematic with FDG-BP imaging. The MYO signal arises from early uptake of the tracer and resulted in increased FDG-BP values, when compared with the corresponding CO-BP values.

Simulations, in-vitro, and in-vivo results indicated that the EV density values could reduce PV averaging effects and provide more accurate estimates of the true myocardial activity. However, the trade-off to increased accuracy was an increase in noise. This increased noise limits the use of EV imaging on a pixel-by-pixel basis with polar maps. It may be more appropriate to use larger regions, such as a 9, or possibly even a 5, segment model to reduce noise effects. This would be similar to studies that calculated EV values from 3 or 4 large regions [2, 3, 4].

In Table 8.1, the published EV values are tabulated along with the results from this research work (using polar map ROIs centered on the MYO wall). The canine model

using CO-BP was found to be in good agreement with the published human values, but larger than the published dog results of Iida [5]. This difference was believed to be due to differences in dog weight.

In both the dog and normal subject chapters, the FDG-EV values were found to be underestimated due to increased BP values resulting from early myocardial FDG uptake. This is inconsistent with the results of Gerber et. al. [4], who found no difference between FDG-based and CO-based EV values. However, as discussed previously, this was believed to be due to ROI placement.

Table 8.1: Published EV density values (standard deviation) for normal myocardium

		LAT	ANT	SEP	INF	APEX
Human	Gerber* 1998	0.62 (0.02)	0.63 (0.02)	0.56 (0.02)	N/A	N/A
	Gerber 1998	0.64 (0.02)	0.63 (0.02)	0.56 (0.02)	N/A	N/A
	Yamamoto 1992	0.66 (0.03)	0.68 (0.04)	0.63 (0.04)	0.67 (0.05)	N/A
	Iida 1991	0.62 (0.05)	0.64 (0.04)	0.62 (0.05)	N/A	N/A
Dog	Iida 2000	0.48 (0.09)	0.48 (0.05)	0.42 (0.05)	N/A	N/A
Dog	present work	0.68 (0.07)	0.63 (0.09)	0.64 (0.08)	0.68 (0.06)	0.72 (0.07)
	present work*	0.44 (0.11)	0.42 (0.12)	0.48 (0.11)	0.48 (0.11)	0.55 (0.06)
Normals	present work*	0.54 (0.07)	0.41 (0.13)	0.42 (0.08)	0.61 (0.08)	0.55 (0.13)

* FDG-BP

Chapter 9

Future Directions

EV values obtained using the CO-BP image were found to provide more accurate estimates of FDG uptake. However, this work did not compare the EV values with other estimates of RC, particularly with those obtained from kinetic modeling, which are also used in our lab. Analysis of the dynamic FDG data should be performed to obtain RC_H , which can then be compared to EV. By characterizing the differences and similarities between EV and RC_H , a better understanding of the strengths and limitations of the methodologies would be gained. This understanding would allow for a better use of one or the other methods in improving FDG measurements.

One of the disadvantages of the current methodology is the increased noise in the corrected FDG polar maps, due to noise in the EV image. Several areas can be pursued to reduce this noise, and allow for the clinical use of the methodology. First, the ROIs used to sample the polar map could be increased in size. Increased ROI size should improve polar map noise, but at the expense of increased smoothing and increased bias from TX spillover. Secondly, the polar maps could be analyzed using only a 9 segment model. That is, MYO and EV polar maps would be created to obtain values for the nine segments, and the corrected MYO values would be calculated for these nine segments only. The advantage to this is that the effects of noisy pixels (i.e. $EV \sim 0$) would be minimized. The disadvantage is that the method is no longer polar map based, and

regional FDG uptake effects may be averaged out. A 9 segment method would be a compromise between the published methods using 3 or 4 manually placed regions, and a true polar map method. Current ASNC standards call for a 17 segment polar map [99], which would help maintain regional FDG uptake values. This would be an advantage over the 9 segment model. However, the effect of noise on the 17 segment model needs to be investigated. Lastly, the EV polar maps could be smoothed prior to PV correction. The type of smoothing that could best remove the noise (e.g. Median filter to remove noisy peaks and valleys) needs to be investigated. The advantage to polar map smoothing is the ability to apply EV values on a polar map basis, as opposed to the segmental regions described above.

The gold standard for BP imaging is a CO acquisition. EV results using the CO-BP image showed promise for the PV correction of FDG uptake values. However, a CO-BP acquisition would increase patient dose and study acquisition time, both of which are disadvantages in clinical imaging. The use of a FDG-BP image was investigated as an alternative to CO-BP. However, early FDG uptake in the myocardial wall, and noisier data (compared with the CO-BP) lead to an increase in the number of ill-conditioned pixels ($EV \leq 0$) in the EV image, skewing the corrected MYO values. The methods described above (increased ROI size and polar map smoothing) need to be investigated as a means of reducing this noise. However, it may not be possible to remove the effects of early FDG uptake in the myocardial wall, unless only one or two FDG frames were used to form the FDG-BP image. The trade-off to this approach is even poorer counting statistics. An alternative method of obtaining a BP image from the dynamic FDG data is factor analysis. As described in Section 7.3, factor analysis attempts to extract a physiological image (i.e. BP, MYO, etc.) from the dynamic data set. Theoretically, factor analysis should be able to extract an FDG-BP image comparable to CO-BP (i.e. no activity in the MYO wall). However, the ability of factor analysis to work with noisy data needs to be investigated to determine whether this method can be used clinically.

Once issues relating to noise and BP creation have been investigated, the method

can be adopted to patient data. This research has developed and characterized the use of EV density imaging for PV correction in ideal circumstances, i.e. phantom work and normal myocardium. The effect of an EV-based PV correction in areas of disease has yet to be investigated. Thinning of the myocardium, often associated with areas of scar, would increase PV losses. Application of the EV-based correction would remove this effect, and the area would appear more viable. However, it may be that the amount of scar is of importance clinically. Conversely, previous ^{15}O -water studies have indicated that EV density values are not reduced due to scar tissue [3, 5], since the EV image makes no distinction between viable and scar tissue. As such, application of the EV values to areas which contain a mix of viable and scar tissue, (but no wall thinning) would not change the relative activity distribution. The effect of an EV-based PV correction on interpretation of FDG values must be investigated. As an initial pilot study, patient data, with and without PV correction, should be separately interpreted by an expert to determine the benefits of the EV correction to patient management. As well, the effect of the correction on the management of patients with various other pathologies that affect wall motion and thickness (i.e. hypertension or left bundle branch block) should be assessed to determine the population of patients who would best benefit from an EV-based PV correction.

Conclusion

The EV image has been shown to increase the accuracy of FDG uptake values by reducing PV losses. This has the potential to improve the accuracy of PET imaging in patients with altered myocardial wall thickness or motion. However, application of the EV values also resulted in increased noise in the FDG uptake values. As well, a number of conditions were shown to bias the EV values, such as transmission or activity spillover from structures adjacent to the heart. Further studies into reducing both EV noise and the effects of spillover may make this method a viable alternative to other PV corrections for clinical PET FDG studies.

Appendix A

Polar Maps

The heart is a semi-ellipsoid shaped muscle that rests on the diaphragm near the midline of the thoracic cavity. It is comprised of 4 chambers, the left ventricular (LV) cavity, the right ventricular (RV) cavity, the right atrium (RA) and the left atrium (LA). The apex of the heart is directed to the left and downward. The inferior wall of the heart sits on top of the diaphragm. The lateral wall is adjacent to the left lung. The septal wall separates the RV and LV cavities [100]. Transaxial, sagittal, and coronal slices of a dog FDG PET image, superimposed on the TX image, are shown in Fig. A.1

The LV myocardium (the heart muscle surrounding the LV cavity) is responsible for pumping the blood through the body, and as such, is thicker than the RV myocardium. In PET imaging, it is the LV myocardium that is of primary diagnostic interest.

Measured PET values can be obtained directly from ROIs placed manually on the transaxial PET slices. However, these ROI do not necessarily correspond to the anterior, inferior, lateral, and septal regions of the heart. Typically, the PET images are resliced along the long axis (base to apex) of the heart as shown in Fig. A.2. Slices taken perpendicular to the long-axis are referred to as Short Axis (SA) slices while parallel slices can either be obtained in the Vertical Long Axis (VLA) or Horizontal Long Axis (HLA) orientation. Fig. A.3 illustrates the SA, VLA, and HLA slices for

the image resliced in Fig. A.2.

Volumetric sampling of the LV myocardium is used to reorganize the 3D cardiac PET data into a 2D form referred to as a polar map (or bulls-eye plot). Each sector in the polar map is obtained by sampling for the maximum along a radial projection originating from the long axis of the LV cavity, as illustrated in Fig. A.4. In normal myocardium, the maximum value corresponds to the centre of the myocardial wall. The centre of the polar map represents the apex while the outer ring represents the base of the heart.

Polar map values can also be sampled as the mean from ROIs of arbitrary size, centered around the myocardium. In this instance, the polar map is first sampled to find the location of the maximum along each projection. The locations of the maximums are then used as the centres for the ROIs.

The polar map can be further subdivided into various regions. For example, in this research, a 9 segment model was used. The polar map was subdivided into distal and basal regions representing the septum, lateral, inferior, and anterior walls. The apex represents the ninth segment, as illustrated in Fig. A.4.

Figure A.1: Sagittal, transaxial, and coronal slices from a dog FDG PET study superimposed on top of the TX image.

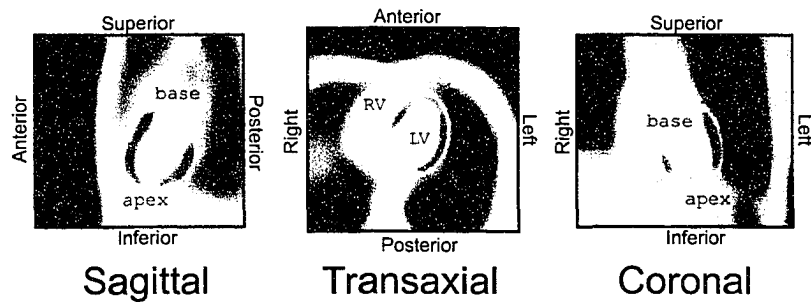


Figure A.2: The transaxial image is resliced into an oblique image. From this oblique image, the Long Axis of the heart is defined. Planes perpendicular to the Long Axis are termed Short Axis (SA) slices.

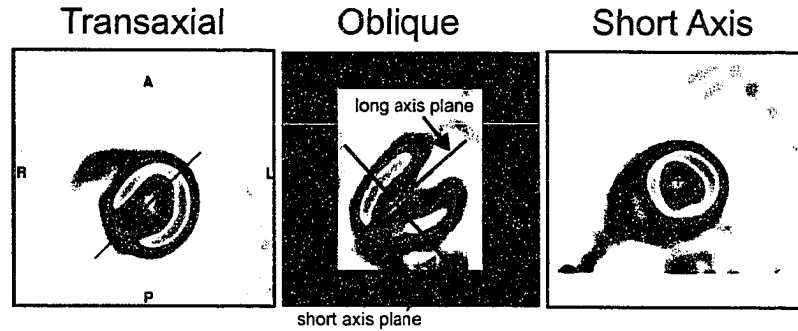


Figure A.3: Once the Long Axis is defined, the image can be resliced into Short Axis (SA) slices perpendicular to the Long Axis, and Vertical or Horizontal Long Axis (VLA and HLA) slices.

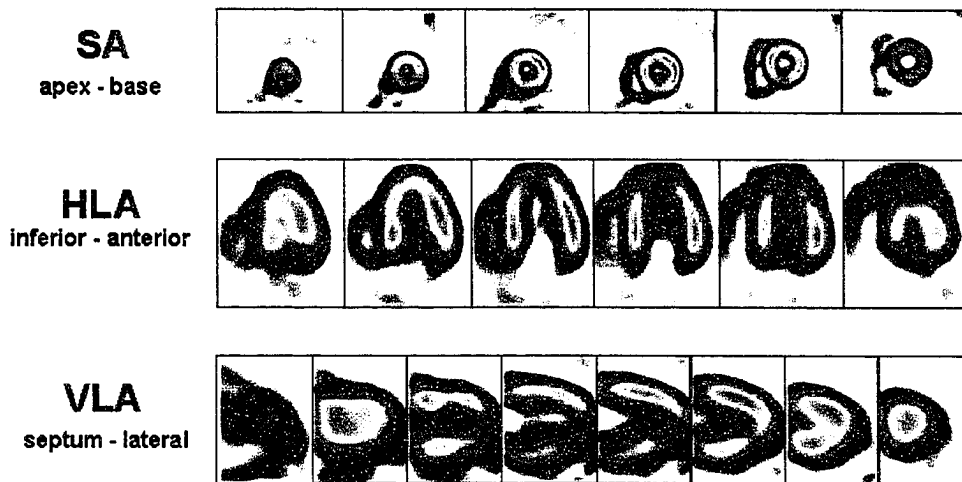
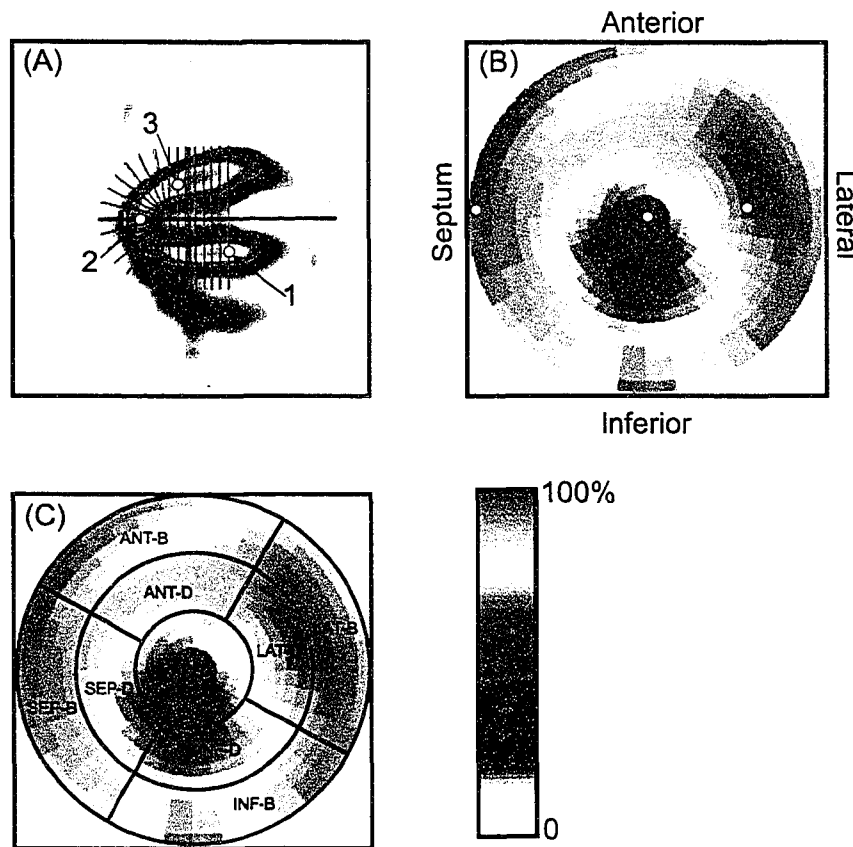


Figure A.4: To produce a polar map, rays originating from the Long Axis are defined around the myocardium, as in (A). The maximum along each ray is used as the polar map sector value, as shown in (B). As an illustration, the maximum along three rays are defined in the PET image. The corresponding location of these three points on the polar map is also shown. The polar map can be divided into segments. In the 9 segment model, shown in (C), Apex, Distal (D) and Basal (B) regions are defined. The distal and basal regions are further subdivided into anterior (ANT), lateral (LAT), septum (SEP) and inferior (INF) segments.



Appendix B

EV Density Values and RC

B.1 MYO Model

Assuming that there is no residual BP activity, or activity in adjacent organs, then the measured myocardial activity in a myocardial voxel is reduced due to PV losses and vascular space, as defined in Eq. B.1.

$$MYO_{meas} = (1 - FBV) \cdot RC \cdot MYO_{true} \quad . \quad (B.1)$$

Here:

- MYO_{meas} and MYO_{true} are the measured and true myocardial activities (Bq/cm^3),
- FBV is the fractional blood volume of the voxel (the vascular space, i.e. blood vessels, capillaries, etc., $\sim 10\%$ [2]), and
- RC is the recovery coefficient due to geometrical- and motion- based PV losses.

The goal is to recover MYO_{true} given MYO_{meas} . This can be done exactly if both RC and FBV are known. Often, an estimate of RC is developed which includes FBV effects as well.

B.2 EV Density Values

From Iida [2], the EV density image is calculated as:

$$EV = \left[\frac{TX}{TX_{LV}} - \frac{BP}{BP_{LV}} \right] * 1.06 \text{ g/cm}^3 \quad . \quad (\text{B.1})$$

As discussed in Chapter 2, the EV density values can be used as an estimate of RC. This estimate includes the effects of the FBV. As well, this method factors in density differences by multiplying the result by the density of whole blood (1.06 g/cm^3). This density factor is necessary since the TX term (i.e. the density of the MYO voxel) is normalized to the density of whole blood. The EV estimate transforms the activity units of the MYO_{meas} values from Bq/cm^3 to Bq/g .

CASE 1: No Vascular Component

If there is no vascular component (i.e. no blood vessels) within the MYO wall, then the second term in Eq. B.1 is due only to LV spillover. In this case, EV values are dependent on resolution- and motion-based PV effects only.

Example: Assume that in a PV volume free region ($RC=1$) of the myocardium, an activity concentration of 1.0 Bq/mL is measured for a given voxel. Dividing this by the density of muscle ($\rho_{muscle}=1.04 \text{ g/mL}$ [73]) yields $0.962 \text{ Bq/g}_{issue}$. Immediately it is seen that converting from volume to tissue mass reduces the expected value, since the measured activity is being transformed onto a different scale (mass instead of volume).

Now, Eq. B.1 yields (using the result from Eq. 2.2):

$$\begin{aligned} EV &= (0.981 - 0.0) * 1.06 \text{ g/cm}^3 \\ &= 1.04 \text{ g/cm}^3 \quad . \end{aligned} \quad (\text{B.2})$$

Using Eq. B.1 to correct the MYO values yields:

$$\begin{aligned}
 MYO_{corr} &= \frac{MYO_{meas}}{EV} \\
 &= \frac{1.00 \text{ Bq/mL}}{1.04 \text{ g/mL}} \\
 &= 0.962 \text{ Bq/g} \quad .
 \end{aligned} \tag{B.3}$$

Comparing Eq. B.3 to the expected value, it is seen that the EV density value is able to exactly recover the true MYO activity of 0.962 Bq/g.

CASE 2: A Vascular Component Exists

The fractional blood volume (FBV) of myocardial tissue (i.e. the volume that is composed of blood vessels, capillaries, etc) is typically around 0.1 [2].

Example: Assume that in a PV-free region (RC=1) of the myocardium, the true activity concentration is 1.0 Bq/mL or 0.962 Bq/g_{tissue}. However, due to FBV=0.1, the volume of myocardial tissue in the voxel is reduced so that the measured signal is also reduced. The fraction of volume which is myocardial tissue is 0.9 (1-FBV) so that the measured activity concentration in a given voxel is 0.9 Bq/mL.

Now, Eq. B.1 yields (modifying the TX term to take into account that the density is now 90% myocardium and 10% blood):

$$\begin{aligned}
 EV &= (0.983 - 0.1) * 1.06 \text{ g/cm}^2 \\
 &= 0.936 \text{ g/mL} \quad .
 \end{aligned} \tag{B.4}$$

So that:

$$\begin{aligned}
 MYO_{corr} &= \frac{MYO}{EV} \\
 &= \frac{0.9 \text{ Bq/mL}}{0.936 \text{ g/mL}} \\
 &= 0.962 \text{ Bq/g} \quad .
 \end{aligned} \tag{B.5}$$

As in Case 1, (where $FBV=0$), application of the EV value recovers the true MYO activity. This will be true for any arbitrary value of FBV.

B.3 Hutchins Model

In Hutchins' model, it is assumed that there are only two terms contributing to the measured myocardial activity [74]:

$$MYO_{meas}(t) = TBV \cdot LV(t) + (1 - TBV) \cdot MYO_{true}(t) \quad . \quad (B.6)$$

Where:

- $MYO_{meas}(t)$ is the measured myocardial signal (Bq/cm³),
- $MYO_{true}(t)$ is the true myocardial PET signal,
- LV is the arterial blood signal,
- TBV represents the fractional volume of the voxel occupied by the blood pool activity (0.0 to 1.0). This is comprised of both ventricular spillover and the FBV within the myocardium, and
- $1-TBV$ represents the fractional voxel volume occupied by myocardial tissue.

For a myocardial uptake image (e.g. $t=70$ min), Eq. B.6 can be rearranged into the following:

$$MYO_{true} = \frac{MYO_{meas} - TBV \cdot LV}{1 - TBV} \quad . \quad (B.7)$$

True myocardial activity concentrations can be estimated by subtraction of the vascular component from the measured data (or by assuming that the blood activity

is 0, as done in Eq. B.1), and then dividing by the RC estimate. In this model, 1-TBV is an estimate of the recovery coefficient, including FBV effects (RC_H). TBV is determined as a free parameter in the model. However, by definition, TBV is also the blood pool (BP) image normalized to its LV value:

$$TBV = \frac{BP}{BP_{LV}} \quad , \quad (B.8)$$

so,

$$RC_H = 1 - \frac{BP}{BP_{LV}} \quad . \quad (B.9)$$

The model assumes that the initial fractional volume of MYO tissue is 1.0. However, as previously discussed, this volume is reduced near the epicardium due to MYO PV losses into pericardial structures. In the EV model, this is accounted for using the TX/TX_{LV} term. A benefit of Hutchins' model is that it does not involve a units transformation that may complicate the interpretation of MYO values corrected using EV density values.

B.4 Modified EV Values

A variation based on Hutchins' model and the EV model, proposed by the author, is given in Eq. B.10.

$$RC_{EV} = \left[\frac{TX}{TX_{LV}} \frac{\rho_{blood}}{\rho_{tissue}} - \frac{BP}{BP_{LV}} \right] \quad , \quad (B.10)$$

where ρ_{blood} is the density of whole blood (1.06 g/cm³) and ρ_{tissue} is the density of tissue in the MYO voxel. The density ratio is necessary since the density of the voxel is normalized to a region of whole blood (the LV cavity). However, in order to exactly

calculate ρ_{tissue} , FBV must be known. If FBV=0, then $\rho_{tissue}=1.04$. In the worst case, FBV=1 (or the voxel contains only blood), and $\rho_{tissue}=1.06$. This represents $\sim 2\%$ difference between the two extreme cases.

A comparison of RC_{EV} to RC_H shows that the main difference is the inclusion of the TX/TX_{LV} term to better deal with MYO PV losses across the epicardium. RC_{EV} is similar to EV, but is unitless so it does not result in a units transformation of MYO_{meas} . However, due to the requirement of known FBV values, it will not be an exact correction, as EV was shown to be. As well, by definition, RC_{EV} should be equal to RC, including FBV effects, or:

$$RC_{EV} = (1 - FBV) \cdot RC \quad . \quad (B.11)$$

Appendix C

Variable FDG Uptake and EV Density

Variable Uptake Model

In this model, the measured myocardial activity in a myocardial voxel (MYO) is comprised of three terms: 1) True MYO activity. This activity is reduced due to PV losses and vascular space. 2) Blood activity in the vascular space, which is also reduced due to PV losses. 3) Ventricular spillover. These terms are related by:

$$\begin{aligned} MYO_{meas} &= (1 - FBV) \cdot RC \cdot MYO_{true} + FBV \cdot RC \cdot LV + SP \cdot LV \\ &= (1 - FBV) \cdot RC \cdot MYO_{true} + (FBV \cdot RC + SP) \cdot LV \\ &= [(1 - FBV) \cdot RC + (FBV \cdot RC + SP) \cdot UP] \cdot MYO_{true} \quad . \quad (C.1) \end{aligned}$$

Here:

- FBV is the fraction voxel volume containing blood,
- RC is the recovery coefficient, due to geometrical and motion PV losses,
- LV is the blood activity (from the left ventricle),

- SP is the fraction of LV signal seen in the myocardium due to spillover (0 to 1.0), and
- UP is the uptake, defined as LV/MYO_{true} (0:complete uptake, >0:incomplete uptake).

Now the FBV activity and ventricular spillover can be obtained from a normalized image of the blood pool, as given by:

$$\begin{aligned} BP_N &= \frac{BP}{BP_{LV}} \\ &= FBV \cdot RC + SP \quad , \end{aligned} \quad (C.2)$$

while the recovery coefficient, including vascular space effects, can be estimated using RC_{EV} (Eq. B.10). RC_{EV} will be used instead of EV to maintain the MYO units of Bq/cm³.

Case 1: UP=0.0

In this case, the LV signal is zero, so Eq. C.1 reduces to:

$$MYO = (1 - FBV) \cdot RC \cdot MYO_{true} \quad , \quad (C.3)$$

and using Eq. B.11:

$$MYO_{true} = \frac{MYO}{RC_{EV}} \quad . \quad (C.4)$$

With only uptake in the MYO, the RC_{EV} is able to correct for PV losses.

Case 2: UP=1.0

In this case, the activity concentrations in the LV and MYO regions are equal. Eq. C.1 now reduces to:

$$MYO = (RC_{EV} + BP_N) \cdot MYO_{true} \quad , \quad (C.5)$$

and:

$$\frac{MYO}{RC_{EV}} = \left(1 + \frac{BP_N}{RC_{EV}}\right) \cdot MYO_{true} \quad . \quad (C.6)$$

Since both BP_N and RC_{EV} are always positive (in the absence of noise), and $BP_N < RC_{EV}$, the ratio will always be positive and less than 1.0. The net effect of incomplete uptake is to increase the measured MYO values. This results in an overestimation of the corrected MYO values.

In general, $UP > 0$ biases the initial measured MYO estimates by a factor of:

$$BP_N \cdot UP \quad . \quad (C.7)$$

This will result in an overestimation of the corrected MYO values by a factor of:

$$\frac{BP_N \cdot UP}{RC_{EV}} \quad . \quad (C.8)$$

This overestimation can not be accounted for using either EV, RC_{EV} or RC_H . A similar problem exists if activity is present in adjacent organs such as the lung or liver. Knowledge of the organ activity and spillover effects may be used to unbiased the initial MYO measurements. For example, subtracting a normalized blood pool image from the initial MYO_{meas} data to obtain unbiased MYO_{meas} values.

Appendix D

^{11}C -Carbon Monoxide Production

The binding of carbon monoxide to hemoglobin is approximately 200 times stronger than that of oxygen [100]. As such, carbon monoxide makes an ideal tracer for blood pool imaging, as is required for EV density imaging. Carbon monoxide can be labeled with either ^{11}C or ^{15}O , both of which are positron emitters and have been used for vascular imaging [101, 102]. The advantage of ^{11}C -carbon monoxide is its longer half-life (20 min vs. 2 min for ^{15}O), which allows for longer scan times and improved image quality.

In large doses, carbon monoxide can be lethal since it displaces oxygen from the hemoglobin. The Canadian Environmental Protection Act sets the maximum allowable levels of carbon monoxide at 2.5% COHb, or 2.5% of the hemoglobin may be bound with carbon monoxide [103]. This level corresponds to a limit of approximately 10 mg of carbon monoxide that can be safely injected into a 25 kg dog.

The ^{11}C was produced in a RDS 111 (CTI, Knoxville TN) cyclotron by bombarding 11 MeV protons onto a nitrogen (N_2) gas target containing 1% oxygen, resulting in ^{11}C -carbon dioxide. This ^{11}C -carbon dioxide was then passed through a column of heated, activated charcoal that reduced the ^{11}C -carbon dioxide to ^{11}C -carbon monoxide. The gas was swept away using He, first through a soda lime trap, and then into a plastic

bag from which the injected dose could be drawn.

During production of ^{11}C -carbon monoxide, it is possible to produce ^{12}C -carbon monoxide. As well, there may also be unreacted ^{11}C -carbon dioxide. It is possible to remove the carbon dioxide with a soda lime trap. However, it is not possible to separate the hot (^{11}C) and cold (^{12}C) carbon monoxide. The specific activity of a tracer is defined as the ratio of activity per mol of both hot and cold compound produced. The presence of the cold carbon monoxide results in a reduced specific activity. If the specific activity is too low, the amount of activity needed for imaging can only be obtained by exceeding the carbon monoxide toxicity limit.

Specific activity was measured from a sample of known volume, drawn from the bag. The activity of the sample was measured using a Capintec well counter (CRC-15 Dual PET) and then injected into a gas chromatograph (GC) (SRI 8610C) with a Carbosphere^(TM) column (Alltech). The area of the carbon monoxide peak measured by the GC (measured as arbitrary unit area, UA) is related to the mass of injected carbon monoxide.

The factor for converting GC area to carbon monoxide mass was obtained through measurement of a standard CO sample drawn from a canister containing 1000 ppm of CO in He (Matheson TriGas). The value, 1000 ppm, represents:

$$1000 \text{ ppm}_{\text{CO}} = 1 \times 10^{-3} \frac{\text{mol}_{\text{CO}}}{\text{mol}_{\text{gas}}} . \quad (\text{D.1})$$

The volume occupied by one mol of gas (at 21 °C and 1 atm) is 24.1 L. The molar mass of CO is 28.01 g. Using these constants and the relation of Eq. D.1, the mass of CO within a volume, V, of the standard gas can be determined as follows:

- 1) The number of moles of CO within the volume is given by:

$$n_{CO} = \frac{V}{24.1 \text{ L/mol}_{gas}} \cdot 1 \times 10^{-3} \frac{\text{mol}_{CO}}{\text{mol}_{gas}} \quad . \quad (\text{D.2})$$

2) The mass of CO within the volume is given by:

$$\begin{aligned} m_{CO} &= n_{CO} \cdot 28.0 \text{ g/mol} \\ &= \frac{V}{24.1 \text{ L/mol}_{gas}} \cdot 1 \times 10^{-3} \frac{\text{mol}_{CO}}{\text{mol}_{gas}} \cdot 28.0 \text{ g/mol} \\ &= V \cdot 1.16 \times 10^{-3} \text{ g/L} \quad . \end{aligned} \quad (\text{D.3})$$

Numerous standard injections with various volumes were performed. The volumes were converted into CO mass using Eq. D.3 and plotted in Fig. D.1. Linear regression analysis of the data indicated that the mass scaled linearly with the measured GC area ($r=0.98$) according to :

$$m_{CO} = (0.53 \frac{\mu\text{g}}{\text{UA}}) \cdot \text{Area}_{GC} + 0.18 \mu\text{g} \quad . \quad (\text{D.4})$$

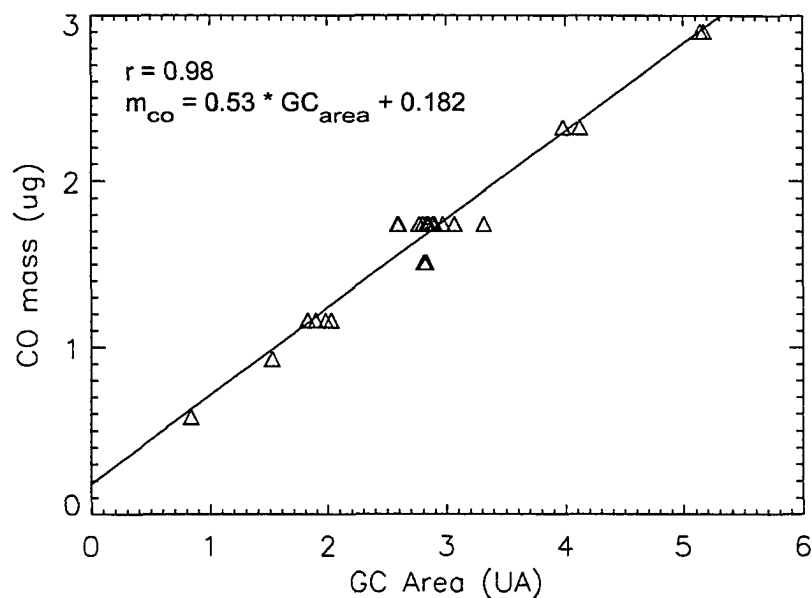
The specific activity for a compound such as carbon monoxide should be quite high, on the order of 10^4 mCi/ μg . However, initial carbon monoxide production runs resulted in specific activities around 1 mCi/ μg . It was believed that the major source of ¹²C-carbon monoxide was the charcoal oven. Ideally, one of the oxygen molecules from the ¹¹C-carbon dioxide should bind to the charcoal bed and not be released. However, due to the high temperature of the oven, the carbon from the charcoal may become unbound and free to form a gaseous ¹²C-carbon monoxide molecule which is swept away along with the ¹¹C-carbon monoxide. The effect of various oven temperatures on ¹¹C-carbon monoxide production is tabulated in Table D.1. Of particular interest is the last column, the mass of CO contained in a 10 mCi sample. The CO mass in a 10 mCi

sample falls below the toxicity limit of 10 mg for all oven temperatures.

Table D.1: Effect of oven temperature on ¹¹C-carbon monoxide production.

Oven temperature (°C)	CO activity (mCi)	CO ₂ activity (mCi)	Specific Activity (mCi/μmol)	M _{CO} in 10 mCi (mg)
700	33.6	718.6	2.6	0.11
725	56.4	656.3	3.1	0.09
750	123	537.0	5.1	0.05
800	253	405.8	7.0	0.04
900	414	123.2	6.7	0.04

Figure D.1: Scatter plot of CO mass (μg) as a function of GC area (measured in arbitrary units of unit area, UA). Linear regression analysis indicated a linear fit ($r=0.98$, solid line) of the data.



References

- [1] C. Rhodes, P. Wollmer, F. Fazio, and T. Jones, "Quantitative Measurement of Regional Extravascular Lung Density Using Positron Emission and Transmission Tomography," *J Comput Assist Tomogr*, vol. 5, pp. 783–91, 1981.
- [2] H. Iida, C. Rhodes, R. de Silva, Y. Yamamoto, L. Araujo, A. Maseri, and T. Jones, "Myocardial Tissue Fraction – Correction for Partial Volume Effects and Measure of Tissue Viability," *J Nuc Med*, vol. 32, pp. 2169–75, 1991.
- [3] Y. Yamamoto, R. de Silva, C. Rhodes, L. Araujo, H. Iida, E. Rechavia, P. Nihoyannopoulos, D. Hackett, A. Galassi, C. Taylor, A. Lammertsma, T. Jones, and A. Maseri, "A New Strategy for the Assessment of Viable Myocardium and Regional Myocardial Blood Flow Using ^{15}O -Water and Dynamic Positron Emission Tomography," *Circ*, vol. 86, no. 1, pp. 167–78, 1992.
- [4] B. Gerber, J. Melin, A. Bol, D. Labar, M. Cogneau, C. Michel, and J. Vanoverschelde, "Nitrogen-13-Ammonia and Oxygen-15-Water Estimates of Absolute Myocardial Perfusion in Left Ventricular Ischemic Dysfunction," *J Nuc Med*, vol. 39, no. 10, pp. 1655–62, 1998.
- [5] H. Iida, Y. Tamura, K. Kitamura, P. Bloomfield, S. Eberl, and Y. Ono, "Histochemical Correlates of ^{15}O -Water Perfusable Tissue Fraction in Experimental Canine Studies of Old Myocardial Infarction," *J Nuc Med*, vol. 41, no. 10, pp. 1737–45, 2000.
- [6] H. Itoh, M. Namura, H. Seki, T. Asai, T. Tsuchiya, H. Uenishi, H. Fujii, S. Fuita,

- Y. Tanabe, J. Ito, M. Shimizu, and H. Mabuchi, "Perfusable Tissue Index Obtained by Positron Emission Tomography as a Marker of Myocardial Viability in Patients with Ischemic Ventricular Dysfunction," *Circ J*, vol. 66, pp. 341–44, 2002.
- [7] K. Schafers, T. Spinks, P. Camici, P. Bloomfield, C. Rhodes, M. Law, C. Baker, and O. Rimoldi, "Absolute Quantification of Myocardial Blood Flow with $H_2^{15}O$ and 3-Dimensional PET: An Experimental Validation," *J Nuc Med*, vol. 43, no. 8, pp. 1031–40, 2002.
- [8] R. de Silva, Y. Yamamoto, C. Rhodes, H. Iida, P. Nihoyannopoulos, G. Davies, A. Lammertsma, T. Jones, and A. Maseri, "Preoperative Prediction of the Outcome of Coronary Revascularization Using Positron Emission Tomography," *Circ*, vol. 86, no. 6, pp. 1738–42, 1992.
- [9] T. Spinks, L. Araujo, C. Rhodes, and B. Hutton, "Physical Aspects of Cardiac Scanning with a Block Detector Positron Tomograph," *J Comput Assist Tomogr*, vol. 15, no. 5, pp. 893–904, 1991.
- [10] R. Wassenaar, R. deKemp, R. Beanlands, and T. Ruddy, "Partial Volume Correction in PET Imaging," *Can J Card*, vol. 17C, p. 123, 2001.
- [11] R. Wassenaar and R. deKemp, "Characterization of Transmission Images for use in Resolution Recovery of Cardiac PET Imaging," *Opto-Canada: SPIE Reegional Meeting*, vol. TD01, pp. 386–89, 2002.
- [12] R. Wassenaar, R. Beanlands, and R. deKemp, "Phantom Studies Investigating Extravascular Density Imaging for Partial Volume Correction of 3-D PET ^{18}FDG Studies," *IEEE Nuclear Science Symposium Conference Record*, vol. 2, pp. 10–16, 2002.
- [13] —, "Phantom Studies Investigating Extravascular Density Imaging for Partial Volume Correction of 3-D PET ^{18}FDG Studies," *IEEE Trans Nuc Sci*, vol. 51, no. 1, pp. 68–71, 2004.

- [14] R. Wassenaar and R. deKemp, "Characterization of PET Partial Volume Corrections for Variable Myocardial Wall Thicknesses," *IEEE Nuclear Science Symposium Conference Record*, 2004.
- [15] R. Wassenaar, S. Mason, A. DiNardo, D. Gauthier, J. DaSilva, R. Beanlands, and R. deKemp, "A Canine Model of 3D PET Extravascular Density Imaging for Myocardial Resolution Recovery," *J Nuc Med*, vol. 46, no. 2, p. 472P, 2005.
- [16] M. Ter-Pogossian, M. Phelps, E. Hoffman, and N. Mullani, "A Positron-Emission Transaxial Tomograph for Nuclear Imaging (PETT)," *Radiology*, vol. 114, no. 1, pp. 89–98, 1975.
- [17] S. L. Bacharach, *Positron Emission Tomography of the Heart*. Futura Publishing Company, Inc., 1992, ch. The Physics of Positron Emission Tomography.
- [18] R. Wassenaar, R. Beanlands, T. Ruddy, and R. deKemp, *Research Advances in Nuclear Medicine 1*. Global Research Network, 2002, ch. Three Dimensional Cardiac Positron Emission Tomography.
- [19] R. Beanlands, G. Nichol, R. deKemp, T. Ruddy, R. Iwanochko, G. Coates, M. Freeman, C. Nahmias, P. Hendry, R. Burns, A. Lamy, L. Mickleborough, W. Kostuk, and E. Fallen, "PET and Recovery Following Revascularization (PARR-1): The Importance of Scar and the Development of a Prediction Rule for the Degree of Recovery of LV Function," *J Am Coll Cardiol*, vol. 40, no. 10, pp. 1735–43, 2002.
- [20] P. Herrero, J. Markham, M. Shelton, C. Weinheimer, and S. Bergmann, "Non-invasive Quantification of Regional Myocardial Perfusion With Rubidium-82 and Positron Emission Tomography," vol. 82, no. 4, pp. 1377–1386, 1990.
- [21] O. Muzik, R. Beanlands, G. Hutchins, T. Mangner, N. Nguyen, and M. Schwaiger, "Validation of Nitrogen-13-Ammonia Tracer Kinetic Model for Quantification of Myocardial Blood Flow Using PET," *J Nuc Med*, vol. 34, no. 1, pp. 83–91, 1993.

- [22] P. Yachimski and P. Challender, *Heart Disease*, 3rd ed. Lippincott Williams and Wilkins, 2003, ch. Diagnostic Imaging and Cardiac Catheterization.
- [23] R. Harrison, M. Kaplan, S. Vannoy, and T. Lewellen, "Positron Range and Coincidence Non-Collinearity in SimSET," *IEEE Nuclear Science Symposium Conference Record*, vol. 3, pp. 1265–8, 1999.
- [24] S. Eidelman and et. al., "Review of Particle Physics," *Physics Letters B*, vol. 592, pp. 1+, 2004.
- [25] S. Cherry, M. Dahlbom, and E. Hoffman, "3D PET using a Conventional Multislice Tomograph without Septa," *J Comput Assist Tomogr*, vol. 15, no. 4, pp. 655–68, 1991.
- [26] H. Grederic and D. Fahey, "Data Acquisition in PET Imaging," *J Nuc Med Technol*, vol. 30, pp. 39–49, 2002.
- [27] S. Cherry, R. Woods, E. Hoffman, and J. Mazziotta, "Improved Detection of Focal Cerebral Blood Flow Changes Using Three-Dimensional Positron Emission Tomography," *J Cer Blood Flow Metab*, vol. 13, pp. 630–38, 1994.
- [28] D. Bailey, K. Lee, G. Stocks, S. Meikle, and T. Dobko, "Clinical 3D PET for Improved Patient Throughput," *J Nuc Med*, vol. 34, p. 184P, 1993.
- [29] P. Marsden, R. Badawi, J. Wong, and M. Maisey, "Validation of 3D Positron Emission Tomography (PET) for Cardiac Scanning in Young Children," *Nucl Med Comm*, vol. 17, p. 283, 1996.
- [30] T. Tshuchida, N. Sadato, Y. Yonekura, K. Sugimoto, A. Nakano, J. Lee, N. Takahashi, A. Waki, Y. Ishii, and H. Itoh, "Myocardial FDG-PET Examination During Fasting and Glucose Loading States by Means of a One-day Protocol," *Ann Nucl Med*, vol. 15, no. 5, pp. 433–38, 1991.
- [31] P. Kinahan and J. Rogers, "Analytic 3D Image Reconstruction Using All Detected Events," *IEEE Trans Nuc Sci*, vol. 36, no. 1, pp. 964–8, 1989.

- [32] S. Matej, G. Herman, T. Narayan, S. Furui, R. Lewitt, and P. Kinahan, "Evaluation of Task-oriented Performance of Several Fully 3D PET Reconstruction Algorithms," *Phys Med Biol*, vol. 39, pp. 355–67, 1994.
- [33] M. Defrise, D. Townsend, and A. Geissbuhler, "Implementation of Three-Dimensional Image Reconstruction for Multi-ring Positron Tomographs," *Phys Med Biol*, vol. 39, pp. 355–67, 1990.
- [34] M. Defrise and P. Kinahan, *The Theory and Practice of 3D PET*, B. Bendriem and D. Townsend, Eds. Kluwer Academic Publishers, 1998.
- [35] M. Daube-Witherspoon and G. Muehllehner, "Treatment of Axial Data in Three-Dimensional PET," *J Nuc Med*, vol. 28, pp. 1717–24, 1987.
- [36] R. Lewitt, G. Muehllehner, and J. Karp, "Three-Dimensional Image Reconstruction for PET by Multi-slice Rebinning and Axial Image Filtering," *Phys Med Biol*, vol. 39, pp. 321–39, 1994.
- [37] S. Matej, J. Karp, R. Lewitt, and A. Becher, "Performance of Fourier Rebinning Algorithm for PET with Large Acceptance Angles," *Phys Med Biol*, vol. 43, pp. 787–95, 1998.
- [38] M. Defrise, D. Townsend, D. Bailey, A. Geissbuhler, C. Michel, and T. Jones, "A Normalization Technique for 3D PET Data," *Phys Med Biol*, vol. 36, no. 7, pp. 939–52, 1991.
- [39] J. Ollinger, "Detector Efficiency and Compton Scatter in Fully 3D PET," *IEEE Trans Nuc Sci*, vol. 42, no. 4, pp. 1168–73, 1995.
- [40] E. Hoffman, T. Guerrero, G. Germano, W. Digby, and M. Dahlbom, "PET System Calibration and Correction for Quantitative and Spatially Accurate Images," *IEEE Trans Nuc Sci*, vol. 36, no. 1, pp. 1108–12, 1989.

- [41] M. Casey, H. Gadagkar, and D. Newport, "A Component Based Method for Normalization in Volume PET," in *Proceedings of the 1995 International Meeting on Fully Three-Dimensional Image Reconstruction in Radiology and Nuclear Medicine*. Kluwer Academic Publishers, 1996, pp. 67–71.
- [42] R. Badawi, N. Ferriera, S. Kohlmyer, M. Dahlbom, P. Marsden, and T. Lewellen, "A Comparison of Normalization Effects on Three Whole-Body Cylindrical 3D PET Systems," *Phys Med Biol*, vol. 45, pp. 3253–66, 2000.
- [43] R. Trebossen and B. Bendriem, "Quantitation in 3D PET: The Effect of Scatter Correction on Recovery Coefficients," *Proceedings of the 1995 International Meeting on Fully Three-Dimensional Image Reconstruction in Radiology and Nuclear Medicine*, pp. 127–31, 1996.
- [44] H. Zaidi, "Comparative Evaluation of Scatter Correction Techniques in 3D Positron Emission Tomography," *Eur J Nuc Med*, vol. 27, no. 12, pp. 1813–26, 2000.
- [45] S. Cherry, S. Meikle, and E. Hoffman, "Correction and Characterization of Scattered Events in Three-Dimensional PET using Scanners with Retractable Septa," *J Nuc Med*, vol. 34, pp. 671–78, 1993.
- [46] J. Ollinger, "Model-Based Scatter Correction for Fully 3D PET," *Phys Med Biol*, vol. 41, pp. 153–76, 1996.
- [47] C. Watson, D. Newport, M. Casey, R. deKemp, R. Beanlands, and M. Schmand, "Evaluation of Simulation-Based Scatter Correction for 3D PET Cardiac Imaging," *IEEE Trans Nuc Sci*, vol. 44, no. 1, 1997.
- [48] T. Spinks, M. Miller, D. Bailey, P. Bloomfield, L. Livieratos, and T. Jones, "The Effect of Activity Outside the Direct Field of View in a 3D-only Whole-Body Positron Tomograph," *Phys Med Biol*, vol. 43, pp. 895–904, 1998.

- [49] B. McKee, R. Clack, P. Harvey, L. Hiltz, M. Hogan, and D. Howse, "Accurate Attenuation Correction for a 3D PET System," *Phys Med Biol*, vol. 36, no. 5, pp. 603–19, 1991.
- [50] R. deKemp and C. Nahmias, "Attenuation Correction in PET Using Single Photon Transmission Measurement," *Med Phys*, vol. 21, no. 6, pp. 771–8, 1994.
- [51] J. Karp, G. Muehllenhner, H. Qu, and X. Yan, "Singles Transmission in Volume-Imaging PET with a 137-Cs Source," *Phys Med Biol*, vol. 40, pp. 929–44, 1995.
- [52] S. Yu and C. Nahmias, "Single-Photon Transmission Measurements in Positron Tomography Using 137-Cs," *Phys Med Biol*, vol. 40, no. 7, pp. 1255–66, 1995.
- [53] D. Bailey, *The Theory and Practice of 3D PET*, B. Bendriem and D. Townsend, Eds. Kluwer Academic Publishers, 1998.
- [54] C. Watson, W. Jones, T. Brun, K. Baker, K. Vaigneur, and J. Young, "Design and Performance of a Single Photon Transmission Measurement for the ECAT ART," *IEEE Nuclear Science Symposium Conference Record*, vol. 2, pp. 1366–70, 1997.
- [55] C. Watson, A. Schaefer, W. Luk, and C. Kirsch, "Clinical Evaluation of Single-Photon Attenuation Correction for 3D Whole-Body PET," *IEEE Trans Nuc Sci*, vol. 46, no. 4, pp. 1024–31, 1999.
- [56] W. Jones, J. Reed, J. Everman, P. Luk, T. Gremillion, B. Castleberry, E. Breeding, M. Musrock, J. Young, M. Overbay, M. Schmand, R. Powers, J. Moyers, K. Baker, and B. Bendriem, "First Time Measurement of Transaxial Resolution for a New High-sensitivity PET Prototype Using 5 LSO Panel Detectors," *IEEE Nuclear Science Symposium Conference Record*, vol. 2, pp. 694–8, 2002.
- [57] R. Bar-Shalom, N. Yefremov, L. Guralnik, D. Gaitini, A. Frenkel, A. Kuten, H. Altman, Z. Keidar, and O. Israel, "Clinical Performance of PET/CT in Eval-

- uation of Cancer: Additional Value for Diagnostic Imaging and Patient Management,” *J Nuc Med*, vol. 44, no. 8, pp. 1200–9, 2003.
- [58] C. Cohade, M. Osman, J. Leal, and R. Wahl, “Direct Comparison of 18-F-FDG PET and PET/CT in Patients with Colorectal Carcinoma,” *J Nuc Med*, vol. 44, no. 11, pp. 1797–803, 2003.
- [59] P. Kinahan, D. Townsend, T. Beyer, and D. Sashin, “Attenuation Correction for a Combined 3D PET/CT Scanner,” *Med Phys*, vol. 25, no. 10, pp. 2046–2053, 1998.
- [60] Y. Nakamoto, M. Osman, C. Cohade, L. Marshall, J. Links, S. Kohlmyer, and R. Wahl, “Comparison of Quantitative Tracer Uptake Between Germanium and CT Transmission Attenuation-Corrected Images,” *J Nuc Med*, vol. 22, pp. 1137–43, 2002.
- [61] R. Wassenaar, R. Wells, and R. deKemp, “Clinical Evaluation of CT versus Ge-68 Attenuation Correction in Cardiac PET Imaging,” *J Nuc Med*, vol. 45, no. 5, p. 118P, 2004.
- [62] R. Wassenaar, R. Beanlands, T. Ruddy, and R. deKemp, “Resolution Recovery with 3D PET Extravascular Density Imaging,” *Opto-Canada: SPIE Reegional Meeting*, vol. TD01, pp. 383–85, 2002.
- [63] J. Colsher, “Fully Three-Dimensional Positron Emission Tomography,” *Phys Med Biol*, vol. 25, no. 1, pp. 103–115, 1980.
- [64] M. Defrise, D. Townsend, and R. Clack, “FAVOR: A Fast Reconstruction Algorithm for Volume Imaging in PET,” *IEEE Medical Imaging Conf*, vol. 35, no. 10, pp. 1919–23, 1991.
- [65] M. Defrise, P. Kinahan, D. Townsend, C. Michel, M. Sibomana, and D. Newport, “Exact and Approximate Rebinning Algorithms for 3D PET Data,” *IEEE Trans Med Imag*, vol. 16, no. 2, pp. 145–58, 1997.

- [66] X. Liu, M. Defrise, C. Michel, M. Sibomana, C. Comtat, P. Kinahan, and D. Townsend, "Exact Rebinning Methods for Three-Dimensional PET," *IEEE Trans Med Imag*, vol. 18, no. 8, pp. 657–64, 1998.
- [67] M. Daube-Witherspoon, S. Matej, J. Karp, and R. Lewitt, "Application of the Row Action Maximum Likelihood Algorithm with Spherical Basis Functions to Clinical PET Imaging," *IEEE Nuclear Science Symposium Conference Record*, vol. 3, pp. 1676–80, 1999.
- [68] T. Obi, S. Matej, R. Lewitt, and G. Herman, "2.5-D Simultaneous Multi-slice Reconstruction by Series Expansion Methods from Fourier-Rebinned PET Data," *IEEE Trans Med Imag*, vol. 29, no. 5, pp. 474–84, 2000.
- [69] D. Bailey, H. Young, P. Bloomfield, S. Meikle, D. Glass, M. Myers, T. Spinks, C. Watson, P. Luk, M. Peters, and T. Jones, "ECAT ART - A Continuously Rotating PET Camera: Performance Characteristics, Initial Clinical Studies, and Installation Considerations in a Nuclear Medicine Department," *Eur J Nuc Med*, vol. 24, no. 1, pp. 6–15, 1997.
- [70] S. Ziegler, B. Pichler, G. Boening, M. Rafecas, W. Pimpl, E. Lorenz, N. Schmitz, and M. Schwaiger, "A Prototype High-Resolution Animal Positron Tomograph with Avalanche Photodiode Arrays and LSO Crystals," *Eur J Nuc Med*, vol. 28, no. 2, pp. 136–43, 2001.
- [71] C. Watson, "New Faster Image-Based Scatter Correction for 3D PET," *IEEE Trans Nuc Sci*, vol. 47, no. 4, pp. 1587–94, 2000.
- [72] J. Mazziotta, M. Phelps, D. Plummer, and D. Kuhl, "Quantitation in Positron Emission Computed Tomography: 5. Physical-Anatomical Effects," *J Comput Assist Tomogr*, vol. 5, no. 5, pp. 734–43, 1981.
- [73] H. Johns and J. Cunningham, *The Physics of Radiology*, 4th ed. Charles C Thomas, 1983.

- [74] G. Hutchins, J. Caraher, and R. Raylman, "A Region of Interest Strategy for Minimizing Resolution Distortions in Quantitative Myocardial PET Studies," *J Nuc Med*, vol. 33, no. 6, pp. 1243–1250, 1992.
- [75] P. Knaapen, R. Boellaard, M. gotte, A. van der Weerdt, C. Visser, A. Lammermsma, and F. Visser, "The Perfusible Tissue Index: A Marker of Myocardial Viability," *J Nucl Cardiol*, vol. 10, no. 6, pp. 684–91, 2003.
- [76] B. Hutton and A. Osiecki, "Correction of Partial Volume Effects in Myocardial SPECT," *J Nucl Cardiol*, vol. 5, no. 4, pp. 402–13, 1998.
- [77] R. deKemp, T. Ruddy, T. Hewitt, M. Dalipaj, and R. Beanlands, "Detection of Serial Changes in Absolute Myocardial Perfusion with ^{82}Rb PET," *J Nuc Med*, vol. 41, no. 8, pp. 1426–1435, 2000.
- [78] A. Da Silva, H. Tang, K. Wong, M. Wu, M. Dae, and B. Hasegawa, "Absolute Quantification of Regional Myocardial Uptake of $^{99\text{m}}\text{Tc}$ -Sestamibi with SPECT: Experimental Validation in a Porcine Model," *J Nuc Med*, vol. 42, no. 5, pp. 772–9, 2001.
- [79] C. Meltzer, J. Leal, H. Mayberg, H. Wagner Jr, and J. Frost, "Correction of PET Data for Partial Volume Effects in Human Cerebral Cortex by MR Imaging," *J Comput Assist Tomogr*, vol. 14, no. 4, pp. 561–70, 1990.
- [80] T. Videen, J. Perlmutter, M. Mintun, and M. Raichle, "Regional Correction of Positron Emission Tomography for the Effects of Cerebral Atrophy," *J Cereb Blood Flow and Metab*, vol. 8, pp. 662–70, 1988.
- [81] H. Muller-Gartner, J. Links, J. Prince, R. Bryan, E. McVeigh, J. Leal, C. Davatzikos, and J. Frost, "Measurement of Radiotracer Concentration in Brain Gray Matter Using Positron Emission Tomography: MRI-Based Correction of Partial Volume Effects," *J Cereb Blood Flow and Metab*, vol. 12, no. 4, pp. 571–83, 1992.

- [82] T. Videen, J. Dunfor-Shore, M. Diringler, and W. Powers, "Correction for Partial Volume Effects in Regional Blood Flow Measurements Adjacent to Hematomas in Humans with Intracerebral Hemorrhage: Implementation and Validation," *J Comput Assist Tomogr*, vol. 23, no. 2, pp. 248–56, 1999.
- [83] B. Lipinski, H. Herzog, E. Kops, W. Oberschelp, and H. Muller-Gartner, "Expectation Maximization Reconstruction of Positron Emission Tomograph Images Using Anatomical Magnetic Resonance Information," *IEEE Trans Med Imaging*, vol. 16, no. 2, pp. 129–36, 1997.
- [84] K. Baete, J. Nuyts, W. V. Paesschen, P. Suetens, and P. Dupont, "Anatomical-Based FDG-PET Reconstruction for the Detection of Hypo-Metabolic Regions in Epilepsy," *IEEE Trans Med Imaging*, vol. 23, no. 4, pp. 510–9, 2004.
- [85] S. Sastry and R. Carson, "Multimodality Bayesian Algorithm for Image Reconstruction in Positron Emission Tomography: A Tissue Composition Model," *IEEE Trans Med Imaging*, vol. 16, no. 6, pp. 750–61, 1997.
- [86] L. Golanowski, R. deKemp, R. Beanlands, and T. Ruddy, "Variance and Covariance of ^{82}Rb Kinetic Parameters: Computer Simulation and Dynamic PET Studies," *Proceedings of the 22nd Annual EMBS International Conference, July 23-28, Chicago, IL.*, pp. 1096–1099, 2000.
- [87] C. Chen, R. Muzic Jr., A. Nelson, and L. Adler, "Simultaneous Recovery of Size and Radioactivity Concentration of Small Spheroids with PET Data," *J Nuc Med*, vol. 40, no. 1, pp. 118–30, 1999.
- [88] —, "A Nonlinear Spatially Variant Object-Dependent System Model for Prediction of Partial Volume Effects and Scatter in PET," *IEEE Trans Med Imaging*, vol. 17, no. 2, pp. 214–227, 1998.
- [89] D. Yu, S. Huang, S. Grafton, W. Melega, J. Barrio, J. Mazziotta, and M. Phelps, "Methods for Improving Quantitation of Putamen Uptake Constant of FDOPA in PET Studies," *J Nuc Med*, vol. 34, no. 4, pp. 679–88, 1993.

- [90] R. Burrow, H. Strauss, R. Singleton, M. Pond, T. Rehn, I. Bailey, L. Griffith, E. Nickoloff, and B. Pitt, "Analysis of Left Ventricular Function from Multiple Gated Acquisition Cardiac Blood Pool Imaging," *Circ*, vol. 56, no. 6, pp. 1024–28, 1977.
- [91] K. Wienhard, L. Eriksson, S. Grootoink, M. Casey, U. Pietrzyk, and W. Heiss, "Performance Evaluation of the Positron Scanner ECAT EXACT," *J Comput Assist Tomogr*, vol. 16, no. 5, pp. 804–13, 1992.
- [92] R. Hart, T. Ruddy, R. Beanland, and R. deKemp, "Sinusoidal Eccentric Thickening Model for ECG-Gated SPECT Perfusion Imaging," *Opto-Canada: SPIE Regional Meeting on Optoelectronics, Photonics, and Imaging*, vol. TD01, pp. 370–72, 2002.
- [93] R. Di Paola, J. Bazin, F. Aubry, A. Aurengo, F. Cavailloles, J. Henery, and E. Kahn, "Handling of Dynamic Sequences in Nuclear Medicine," *IEEE Trans Nuc Sci*, vol. NS29, pp. 1310–21, 1982.
- [94] D. Barber, "The Use of Principle Components in the Quantitative Analysis of Gamma Camera Dynamic Studies," *Phys Med Biol*, vol. 25, pp. 283–92, 1980.
- [95] R. Haralick, S. Sternberg, and X. Zhuang, "Image Analysis Using Mathematical Morphology," *IEEE Tans Pattern Anal Machine Intell*, vol. PAMI-9, pp. 532–50, 1987.
- [96] K. Jordan, B. Knoop, and R. Weise, "The CEC Emission Phantom for PET and SPECT," *Rad Protection Dosimetry*, vol. 49, pp. 321–324, 1993.
- [97] G. Vitale, R. deKemp, T. Ruddy, K. Williams, and R. Beanlands, "Myocardial Glucose Utilization and Optimization of ^{18}F -FDG PET Imaging in Patients with Non-Insulin-Dependent Diabetes Mellitus, Coronary Artery Disease and Left Ventricular Dysfunction," *J Nuc Med*, vol. 42, no. 12, pp. 1730–36, 2001.

- [98] F. Hermansen, P. Bloomfield, J. Ashburner, P. Camici, and A. Lammertsma, "Linear Dimension Reduction of Sequences of Medical Images: II. Direct Sum Decomposition," *Phys Med Biol*, vol. 40, no. 11, pp. 1921–41, 1995.
- [99] M. Cerqueira, N. Weissman, V. Dilsizian, A. Jacobs, S. Kaul, W. Laskey, D. Pennel, J. Rumberger, T. Ryan, and M. Verani, "Standardized Myocardial Segmentation and Nomenclature for Tomographic Imaging of the Heart: A Statement for Healthcare Professionals from the Cardiac Imaging Committee of the Council on Clinical Cardiology of the American Heart Association," *J Nucl Cardiol*, vol. 9, pp. 240–5, 2002.
- [100] G. Tortora and S. Grabowski, *Principles of Anatomy and Physiology*, 9th ed. John Wiley and Sons, INC, 2000.
- [101] H. Glass, A. Brant, J. Clark, A. De Garetta, and L. Day, "Measurement of Blood Volume using Red Cells Labeled with Radioactive Carbon Monoxide," *J Nuc Med*, vol. 9, pp. 571–575, 1968.
- [102] O. Schober, G. Meyer, C. Bossaller, H. Creutzig, P. Lichtlen, and H. Hundeshagen, "Quantitative Determination of Regional Extravascular Lung Water and Regional Blood Volume in Congestive Heart Failure," *Eur J Nuc Med*, vol. 10, no. 1-2, pp. 17–24, 1985.
- [103] F. Hopper, S. MacDonald, M. Shepherd, K. Wilby, and P. Wong, "National Ambient Air Quality Objectives for Carbon Monoxide," *Section 8, Canadian Environmental Protection Act*, 1994.